From Stress to Strain for Damage-Prediction in Atherosclerotic Plaques

A Twelve-Metric Sensitivity Study using Plaque-Specific Fibre Architectures

by **Daniël Rutten**

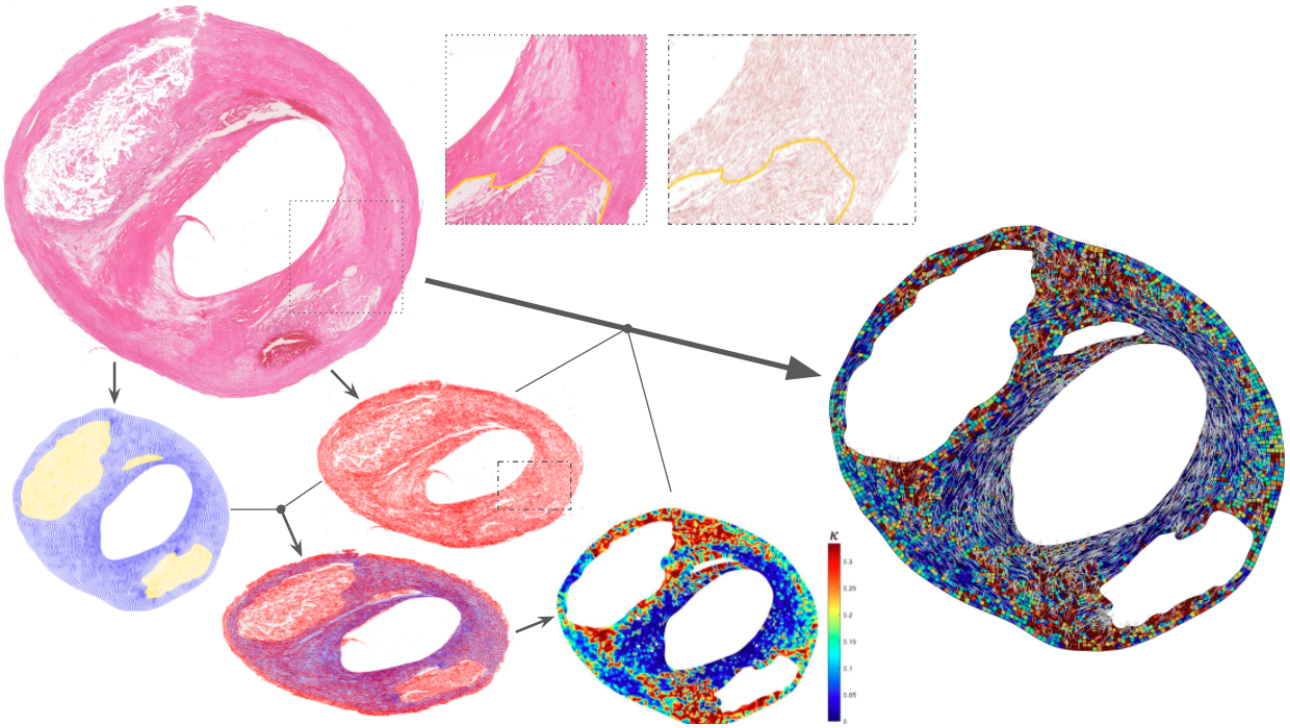

A thesis[1] presented for the degree of
MSc BioMedical Engineering

Technische Universiteit Delft, Netherlands
3mE Faculty of Mechanical, Maritime, & Materials Engineering

[1]supervised by Ali Akyildiz

Chapter 1

Introduction

1.1 The Atherosclerotic Burden

Roughly one in three people die due to atherosclerosis [1]; it is the world's leading cause of death (17.25million or 30% in 2019) and disability (30.93million or 13.95% of DALY's in 2019) [1]. Poignantly, a significant portion ($> 60\%$, [2]) of those deaths are unpredictably sudden: occurring in patients within one hour of symptom onset[1] [3]. Furthermore, in 50% of sudden cardiac deaths [3] and 10-20% of sudden stroke deaths [4], sudden death is the *first* manifestation of atherosclerotic disease[2]. Apparently, sudden death patients are under-identified and under-treated. However, that is not for lack of trying: atherosclerosis, besides being the most lethal disease, is also the most expensive, leading US medical expenditure in 2016 at 363.4billion US$ (13% of total) [5]. Thus, in order to address atherosclerosis' preeminent expense and burden of disease, improved prevention and prediction are necessary.

1.2 Background: Prevention and Prediction of Atherosclerosis

Prevention of atherosclerosis, despite significant advances, is struggling to further mitigate the burden of disease. Preventative interventions typically consist of lifestyle changes (e.g. diet, exercise, and smoking-cessation) and preemptive pharmacology[3] [6, 7], guided by risk-profiling (based on epidemiological findings [8, 9, 10]) and prior symptoms [6]. Yet in spite of ongoing advancements[4] (see [11, 12, 13, 14]), amelioration of the atherosclerotic burden has been incremental since the implementation of risk-profiling and statins (discovered in the '70's) [11, 13]. Meanwhile, increasing prevalence of diabetes, metabolic syndrome, obesity, and the 'Western-lifestyle'[5] - all of which are associated with atherosclerosis - are compounding the atherosclerotic burden [1, 5, 15, 16]. Thus, targeted treatments and improved predictive methods are necessary to make further inroad into (sudden-death) prevention.

Prediction of atherosclerotic events was traditionally guided by symptoms (e.g. angina), blood flow metrics, and calcium scoring. The traditional 'gold-standard' of atherosclerotic diagnosis was (coronary) angiography[6], which provides real-time visualisation of luminal blood flow[7]. Hence, an angiogram allows for assessment of stenosis, which gives a (mediocre) indication of atherosclerotic plaque-progression and is associated with ischemia and atherosclerotic-events in symptomatic patients [18, 19, 20, 21, 6, 5]. X-ray angiography also allows for assessment of arterial calcification (via calcium

[1] ... or < 24 hours if the patient was unobserved; i.e. patient found dead < 24 hours after being asymptomatic.

[2] Not to mention, those sudden events which do not lead to death often cause (severe) disability instead [1, 5]

[3] Athero-preventative drugs include: statins; lipid-lowering agents; anti-coagulants; anti-platelets; anti-hypertensives.

[4] PCSK-9 Inhibitors, Ezetemibe, Anti-Inflammatory (Canakinumab) treatment in particular

[5] A shorthand for sedentary lifestyle, in urban environments, eating a relatively processed and high-cholesterol diet.

[6] Coronary Angiography consists of leading a catheter to the coronary (via a femoral or radial artery) and injecting contrast-fluid into the bloodstream to facilitate real-time X-ray imaging of blood flow through the lumen [17]. Angiography can also be combined with computed tomography (CTA) to enable 3D imaging of the coronary tree [17]

[7] A common metric for blood flow is the *Fractional Flow Reserve* (FFR): The ratio of aortic blood pressure to coronary blood pressure distal to a (suspected) lesion. [17]

scoring[8]), another event-predictor [5, 6, 17, 19, 20, 21, 22, 23].

Unfortunately, the predictive power of traditional markers is limited [24, 25]. Firstly, because the markers are not always applicable: symptom-onset is often *after* a (potentially-lethal) event [3, 5, 6], stenosis only predicts events in symptomatic patients ($> 49\%$ stenosis) [19, 26], and calcium scores are zero in the majority of lesions - especially those likely to rupture [27]. Secondly, the toxicity/radiative cost of angiography makes it inappropriate for preventative screening[9] [30]. Lastly, although traditional markers predict the *likelihood* of events, they do nothing to pinpoint the actual event-site. Hence, they cannot be used to accurately guide targeted interventions[10].

Contemporary prediction therefore shifted its focus to the etiology of atherosclerotic-events. Two pathological mechanisms were found to generate the thrombi responsible for atherosclerotic-events: plaque-rupture (60% of sudden cardiac deaths [27]) and plaque-erosion (40% [27]). Though imaging markers for erosion - a pathophysiological phenomenon[11] - initially proved elusive, markers for rupture - a mechanical phenomenon[12] - were readily determined from histopathology. Specifically, the morphological markers predicting plaque rupture[13] were [27]:

Vulnerable Plaque Markers:

- Large Necrotic Core ($> 30\%$ plaque-area considered high-risk)
- Thin Overlying Fibrous Cap ($> 65\mu m$)
- Macrophage Infiltration (i.e. inflammation)
- Speckled Micro-Calcifications
- Intra-Plaque Hemorrhage
- Neovasculature

Lesions combining these vulnerable morphological features - so-called thin-cap fibrous atheroma (TCFA) [27] - became known as 'the vulnerable plaque' morphology [27, 33].

Computational modelling studies subsequently corroborated the mechanical foundation of plaque-rupture, demonstrating that - even using simplifying assumptions[14] - peak structural stresses predicted plaque rupture-sites with $> 60\%$ sensitivity [34, 35] and a strength threshold of ≈ 300kPa [35]. In addition, the morphological markers were shown to cause elevated plaque-stresses [35, 36, 37, 38]. These promising results suggested that the path to improved prediction was paved by morphological and mechanical markers. However, this promise has yet to translate to clinical practice.

Morphological markers, though clinically-obtainable using newly-developed imaging modalities, have had limited success due to a lack of specificity. Whereas initial demonstrations of morphological- and event-sensitivity (MRI [39, 40], IVUS [41, 42, 43, 44], NIRS [44]) were

[8]Coronary Artery Calcium Score (CACS) is typically calculated via the Agatston-Method [22], which uses 130 Hounsfield units as a threshold for identifying calcifications. Generally, more calcification $\rightarrow$ higher CACS $\rightarrow$ higher risk.

[9]In the peripheral and carotid arteries, clinical practice has therefore already shifted to ankle-brachial index and/or duplex sonography (ultrasound with Doppler analysis) as alternative modalities for assessing blood flow [17, 28, 29]

[10]like balloon angioplasty, stenting, endarterectomy, or revascularisation/bypass

[11]Erosion: Thrombogenesis atop intimal plaque with a dysfunctional or absent endothelial layer. The endothelial layer is stripped/damaged by atherogenic factors like inflammation or low/oscillatory hemodynamic shear stress [27].
Imaging markers for erosion required either immunological imaging or high-resolution imaging of the vessel wall. The imaging modalities that make these possible, PET/SPECT and OCT (perhaps IVUS) respectively, have relatively recently become available for research - let alone clinical - purposes [17].

[12]Rupture: Separation of the fibrous cap overlying a necrotic core, releasing its contents into the lumen where they trigger acute thrombogenesis.

[13]These markers were derived from a study of coronary arteries [27], however the heuristics apply to carotid plaques as well [31, 32].

[14]Notable simplifications include: i) isotropic material models (rather than orthotropic); ii) 2D geometries (plane strain assumption); iii) Homogeneous intima material modelling (only distinguishing intima/media/adventitia and lipid pools/macro-calcifications)

promising, the natural history set-up of some of these studies revealed a new paradox: most of the predicted 'vulnerable plaques' did not rupture [41, 45]. Moreover, some TCFAs were stable for years [43, 46]: apparently, not all thin caps are vulnerable. Thus, morphology alone is not sufficient for event-prediction [45]; alternative markers are necessary. At the time, the foremost candidates were mechanical[15].

Mechanical markers, though effective predictors [34, 35, 49, 50], have struggled to translate to the clinic because of their complicated acquisition process. Indeed, 'structural stress' cannot be read directly from vascular imaging; instead, imaged deformations must first be passed through the *computational lens*:

***Computational Lens*:**

1. A representative (whole) plaque geometry
2. Accurate material models (stress-deformation relationships) for each plaque-component
3. Simplifying assumptions to facilitate computations/accommodate imaging limitations
4. Computation and post-processing (visualisation) of metrics

This acquisition process can take hours and one or more specialists to perform: a prohibitive obstacle for clinical application [17]. Although automation is a feasible solution to mechanical markers' long acquisition times, it would require consensus on an effective method. Unfortunately, this consensus has yet to be reached, as the elements of the computational lens presented new obstacles:

***Computational Lens - Obstacles*:**

1. Clinically-applicable whole-vessel imaging modalities require development
2. Material Models require conceptual development and accurate experimental testing
3. Modelling assumptions require justification and quantification
4. Computed results have to demonstrate high sensitivity/specificity

Forgoing the historical details (see [17, 32]), roughly thirty years of development have arrived at the current state-of-affairs:

***Computational Lens - State-of-Affairs*:**

1. No consensus. Ultrasound (hybrid) modalities have the most potential[16]
2. No consensus. Mechanical-testing demonstrated significant intimal-heterogeneity[17] [52, 53]). Nevertheless, many models/parameter-sets have become available for computational purposes (e.g: [54, 55]). Methodological consensus was reached: inflation or biaxial testing supplanted uniaxial tensile testing [56] and the bespoke HGO material model - which accounts for intimal fibres and orthotropicity - is the most conceptually accurate, though not the most popular due to computational difficulty.

[15] A contemporary alternative worth mentioning is inflammatory-markers, obtained using PET/SPECT scans. Inflammation in plaque-caps has been successfully associated with rupture [47], which can be explained via degradation of cap-fibre - facilitating rupture - by inflammatory MMP-release [48]. However, these promising results have limited clinical application because PET/SPECT tracers are not yet readily available for clinical use [17].

[16] Ultrasound, perhaps hybridised with NIRS, offers the best combination of resolution, acquisition time, penetration depth, accessibility, and affordability [17]. Current research-standards - histology and MRI - are unsuited to clinical application because they require excision and are susceptible to motion artefacting respectively [17].

[17] Histological studies have confirmed that intimal tissue variability is related to the effects of mechanical loading and inflammation on intimal-fibre quality [51, 48].

3. No consensus, as reliable $> 90\%$ sensitivity has yet to be demonstrated in an $n > 20$ study population (and the ends will justify the means). Meanwhile, insights into modelling errors have been achieved[18].

4. Consensus: Rupture-sensitivity of plaque structural stress metrics[19], which include: maximum principal stress, circumferential stress, von Mises stress [34, 35, 49, 50, 60]. Alternatives to structural stress metrics - e.g. shear and normal stress, strain, or energy - have been considered, though only studied in negligibly small populations ($n < 10$). No consensus exists regarding a stress threshold-value[20].

In recap, morphological markers alone are useful but ultimately insufficient for atherosclerotic rupture prediction. Supplementation with mechanical markers (stress-based) has demonstrated added predictive value [49, 50], but clinical application has been obstructed by their complicated acquisition: the 'computational lens'. Moreover, unequivocal sensitivity and specificity results (say, $> 90\%$) have yet to be demonstrated in a reliably large study population ($n > 20$). An important limiting factor for sensitivity/specificity appears to be the observed heterogeneity of intimal material properties [36], which gives rise to the 'vulnerable thin-cap' paradox and the lack of a definitive intimal-strength value (rupture-threshold). The root cause of this heterogeneity appears to be differences in intimal fibre-content caused by variations in pathology and mechanical loading. Thus, accurate acquisition and modelling of fibre may be the next step towards improved prediction.

1.3 Niche 1: Fibre-Cognisant Sensitivity Study

There is a gap in the literature for a fibre-cognisant rupture-sensitivity study: one which models patient-specific culprit-plaque geometries *including* intimal fibre-distributions. The closest precedent, to the author's knowledge, is G.R. Douglas's dissertation [51] and the associated article by Douglas et al. [61]. Though not sensitivity-studies, they present fibre-cognisant modelling of $n = 31$ symptomatic *non-culprit* plaques[21]. The non-culprit plaques were imaged using scanning electron microscopy (SEM) and processed computationally to acquire geometry and fibre-distributions. These were then finite-element modelled using an HGO intimal material models to produce two sets of models: a fibre-cognisant orthotropic set ($\kappa = 0.136$)[22] and an otherwise-equivalent isotropic set ($\kappa = \frac{1}{3}$) for comparison. Douglas et al. conclude that implementing intimal fibre leads to elevated stress-values throughout the plaque, including at locations deeper in the plaque (unprecedented in isotropic modelling), and sometimes leading to alternative peak-stress sites [51, 61]; hence, they recommend the implementation of intimal fibre for improved damage-prediction.

Douglas et al.'s mechanical conclusions echo similar findings presented in previous computational studies comparing orthotropic to isotropic intimal models [32]. Furthermore, Douglas's dissertation [51] includes a thorough study of intraplaque damage and dispersion variations

[18] Significant variability in computed peak-stresses between 2D and 3D modelling results [57] and significant dependence of computational results on the choice of intimal material model [36, 58, 59]. Generally accepted modelling assumptions include: incompressibility, discrete material boundaries, plane strain, neglecting residual stresses [32].

[19] This acceptance was achieved across studies, whereas high sensitivity ($> 80\%$) has yet to be demonstrated in a large study population ($n > 20$) using any single method. This is likely due to the difficulty and workload involved in obtaining and processing a large study population.

[20] Greatly varying estimates have been published [32]. This variability - which further confounds the 'vulnerable thin-cap' paradox - is likely caused by different choices of intimal material model [36], highlighting the importance of accurate material characterisation (i.e. fibre quality). Besides computational estimates, significant variability has also been reported in mechanical testing [52, 55].

[21] Specifically, 16 coronary and 15 carotid plaques

[22] The choice of a fixed dispersion parameter (κ) value is a noteworthy methodological simplification: the true fibre distribution would have region-specific variations in κ. Though Douglas does not explain the reason for this simplification, it seems likely (from experience acquired during the current study) that the choice was made to facilitate non-diverging computations.

throughout the intima, leading to the following histopathological conclusions (which were observed/proposed earlier by the studies in parentheses):

- Fibre tends to align with the predominant/circumferential loading direction ([62, 63])
- Pathology is associated with misalignment/dispersion ([62, 63])
- Intimal damage usually reflects inter-fibre separation rather than fibre-tearing ([64])
- Intimal Damage may propagate along inter-fibre planes ([64])
- Fibre 'triangles' manifest at lipid-pool shoulders where intimal thickening, circumferential, and lipid-encircling fibre groups meet. These 'triangles' have increased dispersion and are vulnerable to damage.

Douglas proposes delamination damage modes, propagation paths, and vulnerable features related to fibre. Thus, the histological findings - like the mechanical ones - suggest an important role for fibre in predicting damage events, clinical or otherwise. A fibre-cognisant damage-sensitivity study is necessary to test this hypothesis.

That said, the results of such a sensitivity-study are clinically inapplicable if they remain beholden to the computational lens. Even if fibre-cognisant modelling brings mechanical damage-sensitivity to new heights, combating computational lens problems 2 through 4, there is still problem 1: clinically-applicable image acquisition. Douglas's method [51, 61] utilises histology, making it non-viable for clinical application. Though other methods for fibre-acquisition have been demonstrated - OCT [65] and DTI-MRI [66, 67] - they too are non-viable: polarisation-sensitive OCT is invasive, non-standard, requires flushing the vessel of blood, and lacks penetration depth; while DTI-MRI is susceptible to motion artefacting and requires a less-accessible large-Tesla MRI.

However, what if the computational lens could be circumvented? The lens (1-4) assumed the calculation of *stress* metrics, for which an accurately segmented whole plaque geometry (1), combined with material models (2), were necessary for modelling (3) and computation (4) using the imaged strain-field as input. However, mechanics is not only stress: the material models are just functions mapping strain to stress values after all. Hence, the plaque mechanics can already be discerned from the imaged strain-field. For instance, if a strain threshold-value were determined it could - unlike stress - be read directly from clinical imaging modalities (e.g: ultrasound or MRI).

1.4 Niche 2: Alternative Mechanical Metrics

Mechanics is not just stress, yet the study of plaque mechanics is traditionally stress-centric. Moreover, it is maximal stress-centric: maximum principal stress, circumferential[23], or von Mises ('average') stress are the most-studied metrics [32]. This reflects the use of engineering methods[24] which traditionally sought to determine stress-values to answer questions like: "how much weight (stress) can this bridge bear before it breaks?" Thus, the seminal studies which gave rise to the study of plaque mechanics and damage-prediction [34, 35, 49] used maximal stress-metrics.

However, there is no *a priori* argument against the use of alternative mechanical metrics; there might be better mechanical predictors than the traditional stresses which have yet to validated. Indeed, there are arguments in favour of alternative metrics: Directional metrics better capture directional damage-modes for instance. Delamination - a damage mode observed by Daemen et al. [64] in carotid plaques and Mohan and Melvin in aorta [68] - is related to

[23]The circumferential direction is theoretically the maximum stress direction in a vessel expanding due to central blood pressure; deviations reflect departures from cylindrical symmetry.

[24]finite-element method, fluid mechanics, and fluid-structure interaction

transverse and shear mechanics causing fibres to, respectively, pull apart from and/or slide along one another. In delamination, it is the cross-linking medium between fibres that breaks, rather than the fibres themselves. Maximal stress-metrics might not capture this behaviour, because the maximal - but sub-critical - stresses usually align with the stiffer fibres [32]. Therefore, shear or transverse stress could be more effective than traditional stress metrics for predicting delamination-based damage. Besides direction, so-called 'fatigue' damage modes are related to cumulative damage. Cumulative damage lends itself to characterisation using (scalar) energy metrics rather than (vector) stress/strain metrics [69]. Lastly, strain-based metrics would not be constrained by the computational lens: whereas stress cannot be read directly from an elastogram - requiring several additional elements (1-4) - strain or strain-energy metrics can. Thus, strain- or energy-based metrics might be more readily applicable in clinical practice.

The literature lacks a thorough study of mechanical metrics other than the traditional stresses. Directional metrics were rarely considered because they have little added value when using the traditional isotropic plaque models [32]. The only thorough computational studies of transverse and shear stresses *in the plaque* - not to be confused with wall/endothelial shear stress[25] - were those by Douglas [51, 61]. Other orthotropic studies [32] adhered to the prevailing traditional stress metrics. On the contrary, histological [63, 64] and material-testing [68, 72] studies more frequently discussed shear- and transverse-mechanics, usually after observing delamination damage-modes. Energy metrics were more frequently studied due to the material fatigue hypothesis of plaque rupture ([73, 74, 75, 76]). However, their findings were redundant: the energy-predicted rupture-sites tended to overlap with maximal stress sites. Also, while material fatigue might explain ruptures observed at sub-critical stress-values, it cannot do so without knowing the exact rupture threshold-values; which are subject to the aforementioned heterogeneity of intimal tissue. Thus, fatigue-based damage studies have fallen out of favour (temporarily), as they have yielded little, despite utilising computational methods (XFEM[26]) significantly more complicated than typical finite-element methods (FEM). Strain-based metrics have been studied sparingly because their added value was initially unclear: strain was often considered equivalent to stress because they are proportional when using linear elastic models. However, it is well-established by now that plaque modelling requires non-linear material models [32], undermining this tacit assumption. That said, the correlation of strain with stress and vulnerable morphological markers [77, 78] *has* since been demonstrated. Recently, the rise of elastography-based material characterisation methods has brought strain-based metrics to the forefront because they preclude the need for additional computation (the aforementioned 'lens') after imaging [79]. All of the above considered, there is a growing need to investigate plaque-mechanical markers other than the traditional stresses.

1.5 Niche 3: Adequate Population Size

As alluded to earlier, plaque-mechanics studies often lack reliably-sized study populations ($n \approx 10$ rather than $n \approx 50+$). It took a body of study (at least [34] and [35]) to support the mechanical understanding of plaque rupture, and powerful single studies like [60] ($n = 32$) [50] ($n = 70$) use large populations. Therefore, any study hoping to reliably investigate the niches above must - given the novelty of the sought-after conclusions - use a sizeable study population.

[25] Wall/Endothelial shear stress is a well-established marker of plaque progression and pathology [70]. Hence, it has also been successfully correlated with rupture, though without specifying the exact rupture-site [71].

[26] eXtended Finite Element Methods

1.6 Study Aims

This study seeks to alleviate the aforementioned three niches in the literature: 1) a fibre-cognisant sensitivity study; 2) mechanical metrics other than the traditional stress-metrics (maximum principal stress, circumferential stress, and von Mises stress); 3) using a sufficiently-large study population. To achieve this, a novel fibre-acquisition and modelling method (1) was applied to a large histological dataset of confirmed plaque ruptures (3) to generate a set each of fibre-cognisant and isotropic patient-specific models. These models were then used to compute a broad selection (see Table 1.1) of directional stress, strain, and energy metrics (2) for sensitivity study (1) and mechanical analysis (2). Details of the method are explained in the following section.

12 Mechanical Metrics Studied		
Stress	S_{vMises}	von Mises
	S_{MaxIPP}	Max. In-Plane Principal
	S_{11}	Circumferential/Fibre-Direction
	S_{22}	Transverse/Fibre-Normal
	S_{12}	Shear
Strain	LE_{MaxIPP}	Max. In-Plane Principal
	LE_{11}	Circumferential/Fibre-Direction
	LE_{22}	Transverse/Fibre-Normal
	LE_{12}	Shear
Energy	ELSE	Elastic Strain Energy
	ESEDEN	Elastic Strain Energy Density
	SENER	ESEDEN *w.r.t. current volume*

Table 1.1: Mechanical Metrics investigated in this study

Chapter 2

Methods

The study method is presented chronologically: First, the histological raw data; Second, the computational modelling and image processing techniques; Last, the statistical analyses performed on the model outputs.

2.1 Histological Raw Data & Selection Criteria

The histological raw data was selected from a previously reported data set [64]. The original data set consisted of 244 serially-sectioned, hematoxylin and eosin (H&E)-stained carotid plaque samples, extracted from 27 carotid vascular-event patients. Careful extraction and processing [64] allowed for preservation of in-vivo plaque geometries.

The current study selected a subset from the original data set using three exclusion criteria: The first criterion eliminated cases with suspected handling artefacts to avoid inaccuracy of the results. The second criterion eliminated adjacent sections with similar geometries, in order to preclude redundancy. The third criterion eliminated sections near the bifurcation because geometry in this region is highly variable along the longitudinal direction; as a result, 2D representations (such as histology) are especially liable to inaccuracy due to the neglected longitudinal dimension. These criteria led to the exclusion of 167 sections and 4 patients.

Besides the three main exclusion criteria, some practical exclusions were also made: During segmentation, 26 sections (across 2 patients) with poorly-defined inclusion boundaries or non-negligible discontinuities in the plaque tissue were excluded because these would be difficult to model accurately. Lastly, 2 sections were excluded after modelling. In one case, the model failed to converge, the other led to an anomalous error during image processing.

Altogether, 195 sections and 6 patients were excluded from the original 244 section, 27 patient data set, leading to a final study population of 49 sections across 21 patients.

2.1.1 Segmentation

Segmentation of the histology sections identified the intima-media boundary, inclusions of various types, and damage sites in the plaque. The segmentation process was confirmed by a certified pathologist.

The intima-media boundary was located by observing the basement layer and transition to smooth muscle cells.

Inclusions were separated into three types: necrotic cores, calcifications, and intraplaque haemorrhage. Necrotic cores were identified by observing cholesterol crystals in the plaque[1]. Calcifications were delineated by a blue (eosin-stained) boundary-line. Intraplaque hemorrhage regions were identified by interstitial erythrocytes (red blood cells) and sometimes also neovasculature. Cases where inclusion-type was unclear (e.g. partially-calcified necrotic cores,

[1]This necrotic core classification is relatively conservative; intra- and even extra-cellular lipid were not allocated as 'soft inclusion' regions.

necrotic cores with interstitial neovasculature, or micro-calcification) were excluded from the study population.

Damage-sites were identified as discontinuities in the plaque originating at either the lumen or an inclusion. Besides location, damage-sites were also differentiated by whether or not erythrocytes (blood cells) were present. From here on, sites **with blood** will be called ***ruptures***, while those **without blood** will be called ***fissures***.

2.2 Modelling: Finite Element Models (FEM)

2.2.1 Geometry

A 2D geometry was created for each section by uploading the histology image (e.g. fig 2.1a) to ABAQUS[2] and tracing the geometrical features determined during segmentation (lumen, inclusion, and intima-media boundaries) using the spline tool (e.g. fig 2.1b). Gaps in the plaque caused by damage were patched back together by realigning damaged fibre and/or conforming to the curvature of the lumen. The media and adventitia were modelled as two layers of 0.6mm thickness (per Hoffman et al. [80]), generated by projecting the intima-media outline outward from the vessel centroid. Lastly, a circular buffer layer was drawn around the vessel in order to artificially improve convergence properties without influencing the vessel mechanics[3].

2.2.2 Element-Type

The chosen element-type was a hexahedral plane-strain hybrid element with 8 nodes (called CPE8H in ABAQUS). The hexahedral plane-strain element was chosen (over a tetrahedral element) because the additional node aided in achieving convergence, not to mention that it is typical for structural-mechanics applications[4] [81]. The hybrid element-type is necessary to accommodate the incompressibility assumption typically made when modelling plaque mechanics. Perhaps the only atypical choice is the 8-node, non-reduced integration scheme. The reasons for this more computationally expensive scheme are two-fold: first, the corresponding quadratic shape functions improve continuity across heterogeneous elements. Second, the 8-node scheme is less susceptible to hourglassing. Both these details proved crucial in the current application.

2.2.3 Mesh

Meshes for the vessel-geometries were generated using the advancing front algorithm with increasing element size further from the lumen. For mesh generation, the advancing front algorithm was chosen over a medial algorithm because its lack of symmetry improved convergence properties. The choice for progressively larger elements away from the lumen was made in order to reduce computational costs while ensuring accuracy near the lumen. It was implemented using abluminally-increasing seeding factors[5], applied along each material boundary.

A mesh sensitivity study was performed on three randomly-selected cases, which confirmed robustness of modelling outputs to variations in the seeding factors when using the current meshing paradigm.

[2]ABAQUS: a FEM software published by Dassault Systemes

[3]Improved convergence results from distancing the vessel from the encircling boundary condition, which mitigates zero-pivot errors during analysis. The material model of the buffer is chosen to have negligible effects on the vessel mechanics; this was confirmed by comparison with several buffer-less test cases.

[4]Structural mechanics favour the 'hex' over the 'tet' element because the linear/reduced tetrahedral element is a constant-strain element [81]. Additionally, the small volume of the tetrahedral element near the vertices makes them more susceptible to divergence and zero-pivot errors than the hexahedral 'bricks'. Therefore, in practice, hexahedral elements are favoured except when the geometries are too complicated to be meshed effectively without using tetrahedra [81].

[5]Mesh Seeding Factors: Plaque-Lumen/Inclusion Boundary (0.1 to 0.01), Media-Plaque (0.1), Adventitia-Media (0.3), Buffer-Adventitia (0.4), Outer Boundary (0.5). Seeding-intervals at the Lumen/Inclusion boundaries started at 0.1 and were decreased further (to 0.01) when necessary to achieve convergence (2 cases).

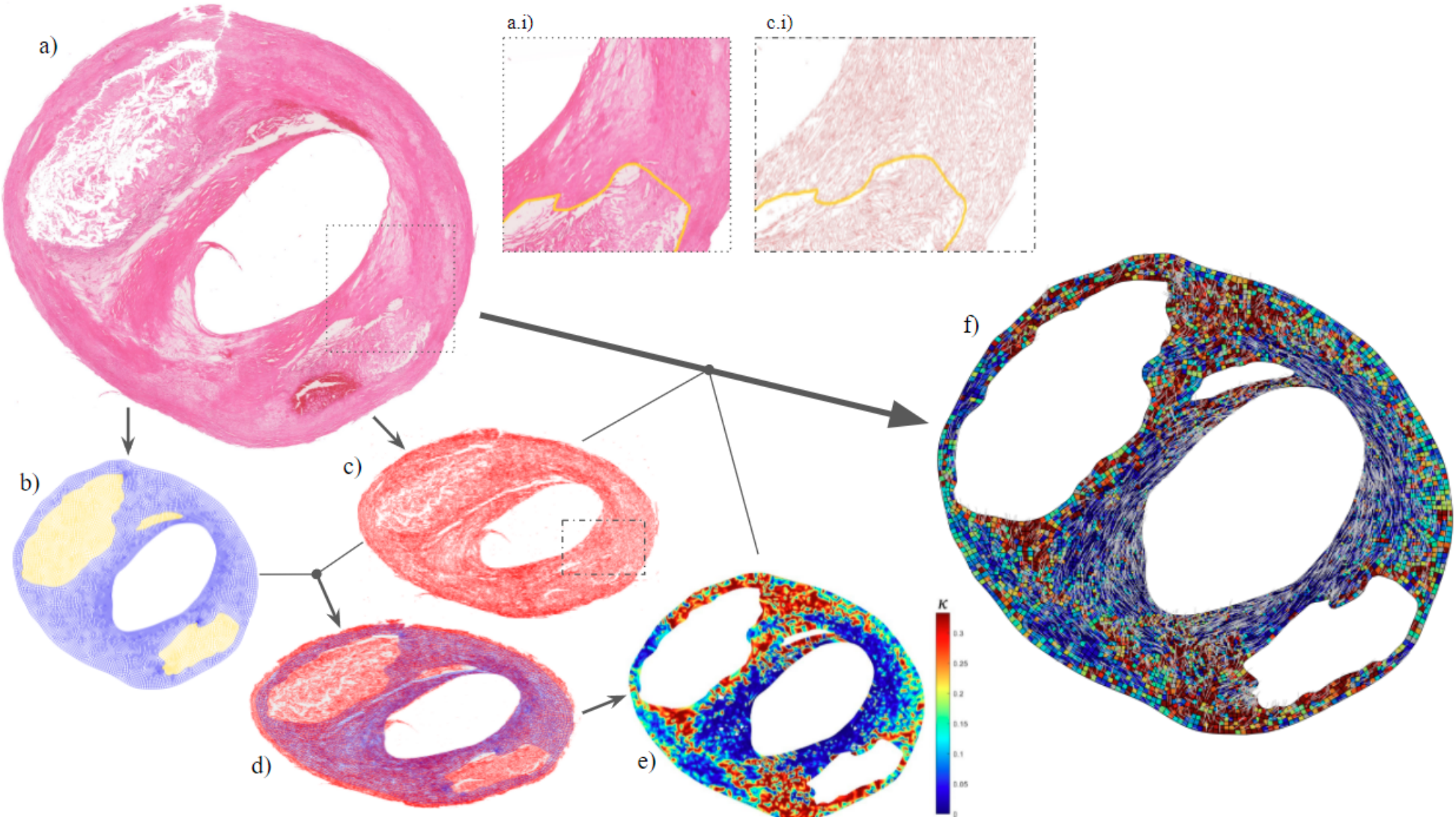

Figure 2.1: Section Analysis and Modelling Pipeline

a) Section 99-105_21000; b) Segmented Mesh Geometry*; c) Detected Fibre Plot;
d) Fibre Plot with FE Mesh Overlay; e) Dispersion Map; f) FEM with Fibre Dispersion and Orientations; .i) inlays

*Inclusions, Media, Adventitia, and Buffer removed for readability

2.2.4 Boundary and Loading Conditions

A single boundary condition was applied to the model: a Dirichlet condition ('encastre') at the outside of the circular buffer layer. This condition reflects constrained vessel inflation due to surrounding tissues and tensile limits of the vessel adventitia. A single loading condition 140mmHg was applied on the luminal surface, representing a typical pathological systolic blood pressure.

2.2.5 Material Models

This study used carotid experiment-derived material models for all vessel components except calcifications, which were modelled using a stiff linear elastic material model. The model parameters and their origins are summarised in table 2.1 below.

Material Models and Parameters					
Material	**Model**	**Type**	**Orientation**	**Parameters**	**Source**
Buffer Layer	Linear Elastic		-	E=10^{-3}kPa, $\nu = 0.05$	Idealised
Adventitia	HGO	Anisotropic Hyperelastic	Circumferential	C_{10}=10kPa, D=0, k_1=400kPa, k_2=140, κ=0.3	Derived from Experiment: Inflation [82]
Media	HGO	Anisotropic Hyperelastic	Circumferential	C_{10}=10kPa, D=0, k_1=10kPa, k_2=60.3, κ=0.2667	Derived from Experiment: Inflation [82]
Plaque	HGO	Isotropic Hyperelastic	-	$\kappa = 0.333$	Experiment: Indentation [55]
		Anistropic Hyperelastic	Plaque-Specific	κ=Plaque-Specific	Above + Fibre-Detection Script
Necrotic Core	Mooney-Rivlin	Hyperelastic	-	C_1=0.046kPa, D_1=4.885kPa, D_2=5.426	Experiment: Uniaxial Extension [52]
Calcification	Linear Elastic		-	E=10^4kPa, ν=0.49	Idealised
Intraplaque Hemorrhage	Mooney-Rivlin	Hyperelastic	-	C_1=0.212kPa, D_1=4.260kPa, D_2=5.312	Experiment: Uniaxial Extension [52]

Table 2.1: Summary of Material Models and Parameters

Note that two plaque models are presented which differ only in the κ-value. This reflects that two FEMs were made per section, one each with the isotropic ($\kappa = 0.333 \approx \frac{1}{3}$) and anisotropic

(image-acquired κ) variants of the plaque-material model. This was done for comparative purposes: the isotropic variant does not account for fibres in the plaque, but has been well-studied in the literature. Conversely, the plaque-specific anisotropic variant *does* account for fibres in the plaque - using locally-specific fibre-parameters obtained through image-processing - but has not been studied before[6]. Therefore, these otherwise-identical FEMs were made to investigate the effect of plaque-specific fibre modelling compared to traditional isotropic modelling.

2.3 Image Processing: Fibre Detection

The locally-specific fibre parameters needed for the plaque-specific anisotropic models were obtained using a custom-written MATLAB script. The script used tools from the image processing toolbox to detect fibres in section images, compute local fibre parameters (dispersion and orientation), and export the corresponding material models to a FEM input-file for ABAQUS. A representation of the processing-pipeline is given in fig. 2.1.

The script's inputs were a 5x magnified, 4K resolution (at least[7]) section image and the corresponding ABAQUS input-file created using the method outlined previously.

The script's first output was a section's fibre plot (see fig. 2.1c), which could be drawn after identifying fibre parameters in the plaque tissue using the Canny Edge Detection Algorithm (MATLAB Image Processing Toolbox)[8]. The fibre plots were validated using idealised test-cases (e.g. pin-stripes and grids) and visual comparison to the original section images. Next, the fibre-data was integrated with the FE mesh to compute a second output: the dispersion map.

The dispersion map (see fig. 2.1e) is a colour-map of the per-element HGO dispersion parameter (κ) values. The κ-values were computed by overlaying a section's fibre plot with its corresponding FEM mesh and applying a numerical implementation of HGO's volume integral[9] [83] to the fibres within each element. The dispersion maps were validated by 'blinded' comparison with visually-estimated dispersion maps drawn over the histological images *before* any computational results had been seen.

It should be noted that the above techniques are unable to extract information from the inevitable gaps at damage sites. Since the selection process had ensured that the gaps were small, the choice was made to fill them in with isotropic HGO plaque material in order to minimally influence the local fibre-mechanics[10].

Ultimately, data from the various outputs was integrated to create the final output: an anisotropic FEM with element-specific κ-values computed from the imaged fibre-distribution (2.1f). This was achieved by translating the computed κ-values and weighted-mean fibre orientations per-element into corresponding anisotropic material models, which was exported to an ABAQUS input-file. The resulting plaque-specific anisotropic FEM, and its isotropic counterpart, were used to compute respective sets of mechanical metric outputs for each section. These results across all sections were aggregated and subjected to statistical analysis.

[6]Recall that Douglas et al. [51, 61] used a fixed κ-value material plaque-model for FE computation, despite having acquired κ-values for the dispersion analysis in [51]

[7]These minimum magnification/resolution specifications were determined after a pilot study comparing results for 1x ($\approx$1K), 2.5x (2K), 5x (4K), 10x (8K), and 15x (12K) images. The minimum effective resolution of 5K was chosen in order to minimise the significant computational cost of the image processing.

[8]The Canny method was selected (over Sobel, Prewitt, Roberts, or 'fuzzy logic') because its output best-resembled observed fibre distribution. This choice aligns with Douglas's in [51].

[9]$\kappa = \frac{1}{4}\int_0^\pi P(\theta)\sin^3(\theta)\theta d\theta$, where $P(\theta) = \frac{2}{\int_0^\pi \hat{P}(\theta)\sin(\theta)d\theta}$, with the fibre-orientation frequency-distribution $\hat{P}(\theta)$

[10]Future iterations of this method might be improved by implementing interpolated fibre-parameters in the gap, especially in case of larger gaps.

2.4 Statistical Analyses

Three statistical analyses were applied to the metrics (table 1.1) computed from the FEMs: correlation analysis, damage sensitivity analysis, and damage threshold (strength) analysis.

Correlation analyses were performed for each of the twelve metrics, both within and across the (an)isotropic FEMs. Ranked correlation coefficients[11] were computed between correspondingly compiled vectors of metric field-outputs. The 'within-model' correlation coefficients were calculated using vectors of metric-values *both* obtained from within the same (an)isotropic section model. These within-model results provided insight into (mechanical) relationships between metrics and allowed redundant metrics to be grouped together for convenience. On the other hand, the 'cross-model' correlation results were computed using one vector compiled from a section's isotropic plaque-model variant, while the other was compiled from the same section's anisotropic plaque-model variant. The cross-model results were used to compare the isotropic and fibre-anisotropic modelling results and provide insight into the effects of implementing fibres.

Whereas the correlation analyses used all of the metric data extracted from a section, the next two analyses focussed on mechanics along specific 'paths', i.e. the lumen or inclusion contours. Therefore, corresponding path data were extracted from the sections. In the case of luminal path data, exclusion regions were sometimes implemented to preclude extraneous analysis on healthy tissue $> 60°$ away from the damage sites. Additionally, Gaussian smoothing was applied to the raw fibre-anisotropic path data - which was very 'spiky' due to varying fibre parameters across neighbouring elements - in order to eliminate false peaks for the subsequent sensitivity analysis.

Sensitivity analysis determines the ability of mechanical metrics to predict plaque damage by searching for peak-values in the path data near damage instances. Traditionally, as in the seminal plaque biomechanics papers [34, 35], sensitivity outcomes are presented as a binary 'hit' or 'miss' given certain maxima-identification and neighbourhood-size parameters. In this study, a 'hit' was defined as a peak (or negative-valued trough) of a given metric that not only occurred within a $\pm 10°$ neighbourhood (± 0.0278 path-distance) of a damage site, but also had a prominence (Δy) of at least 15% compared to the mean metric value in that same neighbourhood[12]. The latter prominence-requirement ensured that insignificant peaks did not generate false positive results. Furthermore, besides the discrete 'hit' or 'miss' analysis, a continuous version of the results was obtained by extracting the path-distance to the nearest damage for each 'hit'.

Last of all, a strength analysis was performed to estimate threshold values for plaque damage initiation. Per-case values were obtained by computing mean local metric values in the vicinity of each damage site, where 'local' denotes the aforementioned $\pm 10°$ (± 0.0278 path-distance) neighbourhood. Population threshold values were then obtained by computing the average of the per-case values.

2.4.1 Population Stratification

For comparative purposes, damage instances within the sections were categorised according to various distinguishing characteristics: First, whether or not erythrocytes (red blood cells) were observed at the damage site: these damage instances are called *ruptures* and *fissures*, respectively. Second, where the damage had occurred: at the lumen or at an inclusion. Inclusions were subdivided further according to their mechanical properties: *soft* (necrotic cores and intraplaque hemorrhages[13]) or *hard* (calcifications). There were also cases where no inclusion

[11] Ranked correlation coefficients were chosen, rather than linear, because the mechanical relationships being investigated were non-linear.

[12] For comparison, Cheng et al. [35] opted for a neighbourhood of $\pm 15°$.

[13] Only 4 instances of damage at an intraplaque hemorrhage region were observed in the study population, so the 'soft' category is dominated by necrotic cores.

was present in the plaque. Third, the location of the inclusion in the plaque - either superficial (abluminal) or deep (adluminal) - was considered. This stratification of damage instances in the study population is visualised in fig. 2.2 below, which also reports the size of each subset. Notably, $n_{\text{damage}} = 167$ damage-instances were studied, of which $n_R = 43$ were confirmed ruptures.

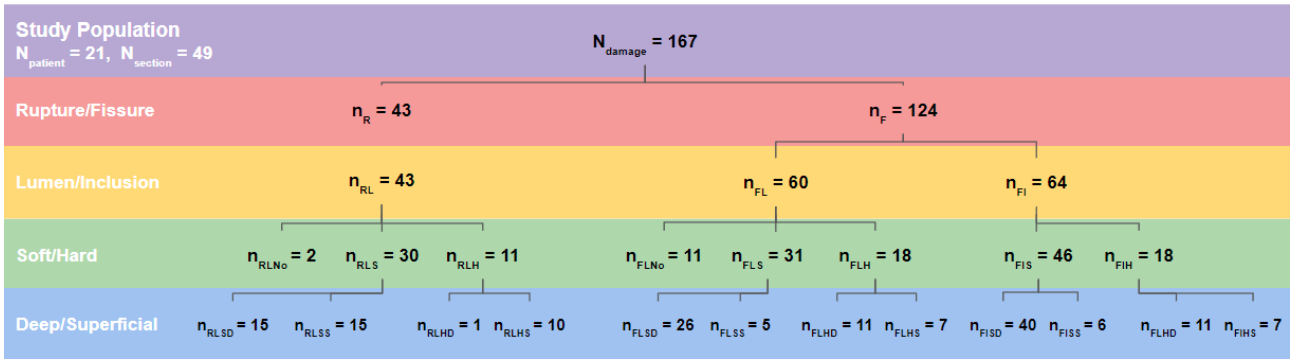

Figure 2.2: Histological Population Stratification

Chapter 3

Results

This section starts with FEM outputs for an illustrative example case before reporting results from the overall population ($n_{sections} = 49$). The latter include a summary of observations drawn from the FEM-outputs, histological observations, and the results of the three statistical analyses into metric correlations, damage-sensitivities, and strength-threshold values.

3.1 FEM Outputs (Example Case)

FEM results for a representative case (previously seen in fig. 2.1) are presented here; specifically: metric output fields and path-data for von Mises stress and shear stress at 140mmHg blood pressure. Just two metrics are presented to avoid redundancy: the correlation analysis revealed that the twelve metrics can be conglomerated into three mechanically-distinct groups[1] (see fig. 3.5 below), of which the important features are captured by the two selected metrics. The remaining metrics' output-fields can be found in appendices B and C.

3.1.1 Metric Output Fields

Figures 3.1 and 3.2 below show output fields for von Mises and shear stress values in the plaque at 140mmHg.

Certain observations held regardless of whether an isotropic or anisotropic plaque model was used: First, von Mises and shear stress values in both cases tended to be greater closer to the lumen. Second, said stresses were greater at high-curvature regions such as lumen 'corners' or inclusion shoulders (particularly NC1). Third, said stresses were greater close to inclusion-boundaries (see adluminal sides of NC2 and NC3). Fourth, the selected stresses had elevated values near the rupture (red arrow) and fissure (cyan arrow) sites.

Conversely, some observations were specific to the chosen plaque model. For instance, the anisotropic plaque model results were less smooth than the isotropic results. Second, von Mises stress values - especially peak values - were significantly higher in the anisotropic case. Third, stress values along inclusion boundaries were relatively higher compared to elsewhere in the plaque when using the anisotropic plaque model. This also led to stress 'hotspots' at shoulders and the abluminal side of inclusions not observed in the isotropic case. Fourth, when using the anisotropic plaque model, stress concentrations were observed in regions corresponding to low dispersion (e.g. shoulders and abluminal side of NC2, abluminal side of NC3) or fibre-channels (ad- and ab-luminal to NC1).

As for other metrics (see app. B), corollaries of the above observations hold in all but one case: that of metric values decreasing with distance from the lumen. Although this holds for all metrics when using an isotropic plaque model, using an anisotropic plaque model it only holds for von Mises, shear ($S12$), maximum in-plane principal stress (S_{MaxIPP}), and fibre-parallel

[1] See fig. 3.5 below for confirmation. The three groupings are: $vMises/S_{MaxIPP}/LE_{MaxIPP}/S11/ELSE/ESEDEN/SENER$; $LE11/LE22/S22$; and $S12/LE12$. The first two groups overlap in the isotropic case.

stress ($S11$). Otherwise, for transverse stress ($S22$), all strains, and all energies, metric values further from the lumen are not necessarily lower.

3.1.2 Path Data

Figures 3.3 and 3.4 below show von Mises and shear stress values (at 140mmHg) along the Lumen and NC1. These data reiterate the observations made from the output fields: abluminally-decreasing metric-values (i.e. Lumen > NC1), peak-values at high-curvature and damage-sites, and greater anisotropic than isotropic von Mises stress values. However, the path data also revealed new insights.

For instance, the path data showed that multiple peaks occur on any given path - especially at sites with high curvature - and that while those near damage-sites tended to be the greatest within a large neighbourhood ($\pm 45°$), they were not necessarily global maxima.

In addition to visualising peak-values, the incorporation of maxima analysis into the path data gave insight into the metrics' predictive performance ('sensitivity'[2]). Hence, in the example case, both shear stress metrics achieved 'hits' for the rupture-site at the Lumen, while the von Mises both 'missed', their peaks falling just outside the required 10° neighbourhood (see fig. 3.3). Similar 'misses' occurred in both metrics for NC1 (fig. 3.4). Thus, sensitivity of the von Mises and shear stress metrics was not dependent on which plaque-model was used (in this example case). However, this indifference did not carry over to other metrics: anisotropic strains and $S11/S22$ achieved 'hits' while their isotropic counterparts did not - thus, the anisotropic metrics were more sensitive to damage overall (see app. C).

[2]Sensitivity = $\frac{\text{no. correctly-predicted ruptures}}{\text{no. confirmed ruptures}}$

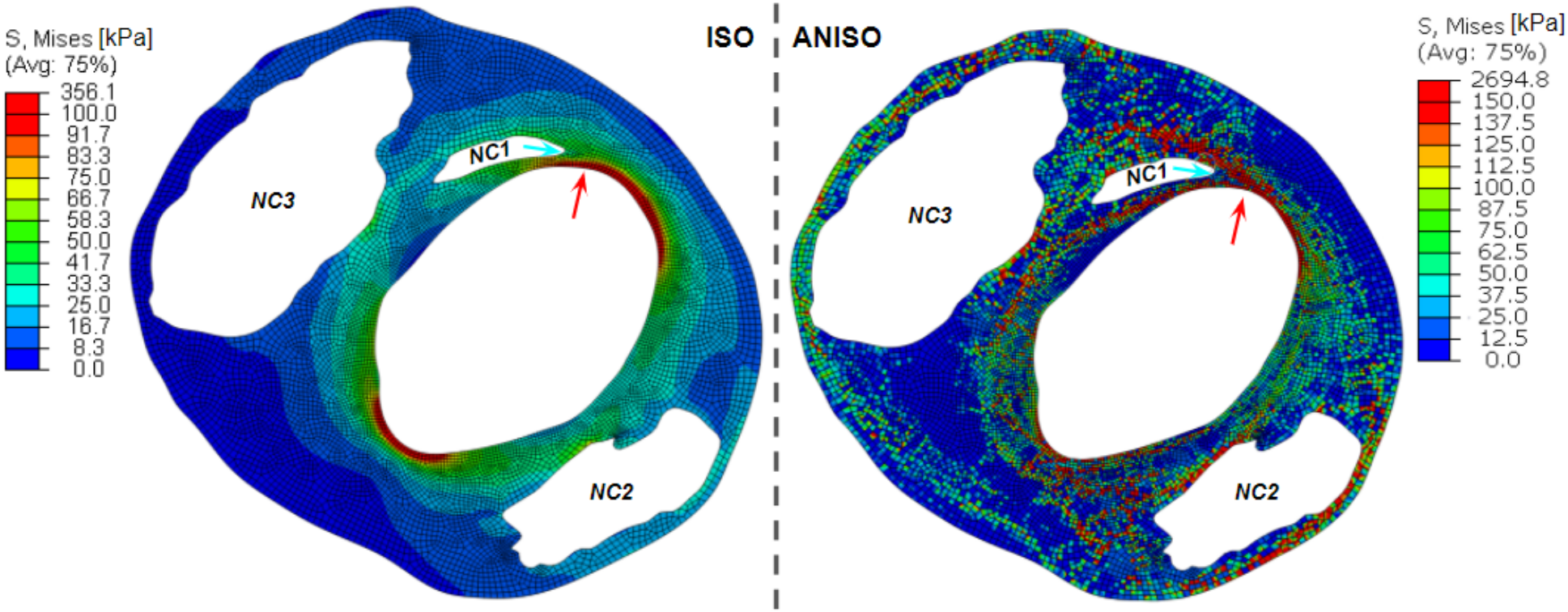

Figure 3.1: von Mises Stress Fields for Isotropic and Anisotropic Models of the Example Case (99-105_12000)
Red Arrow: Rupture
Cyan Arrow: Fissure

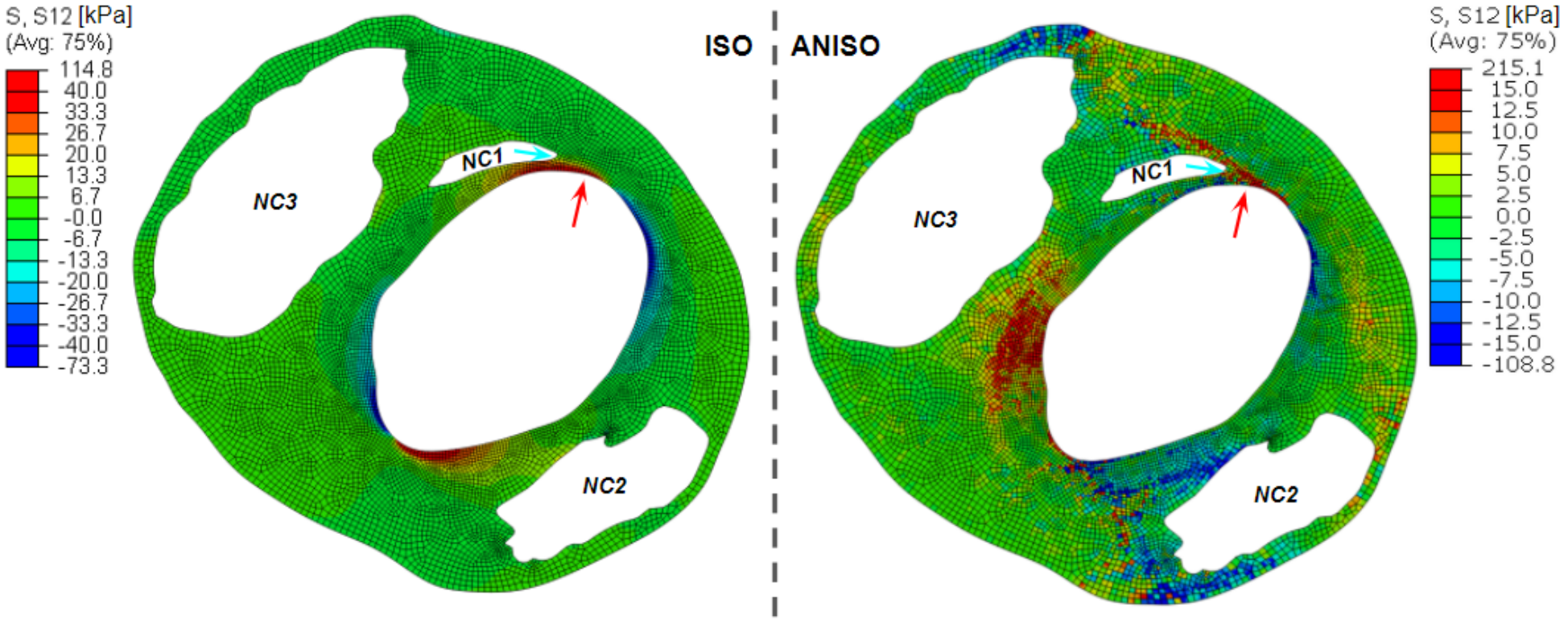

Figure 3.2: Shear Stress Fields for Isotropic and Anisotropic Models of the Example Case (99-105_12000)
Red Arrow: Rupture
Cyan Arrow: Fissure

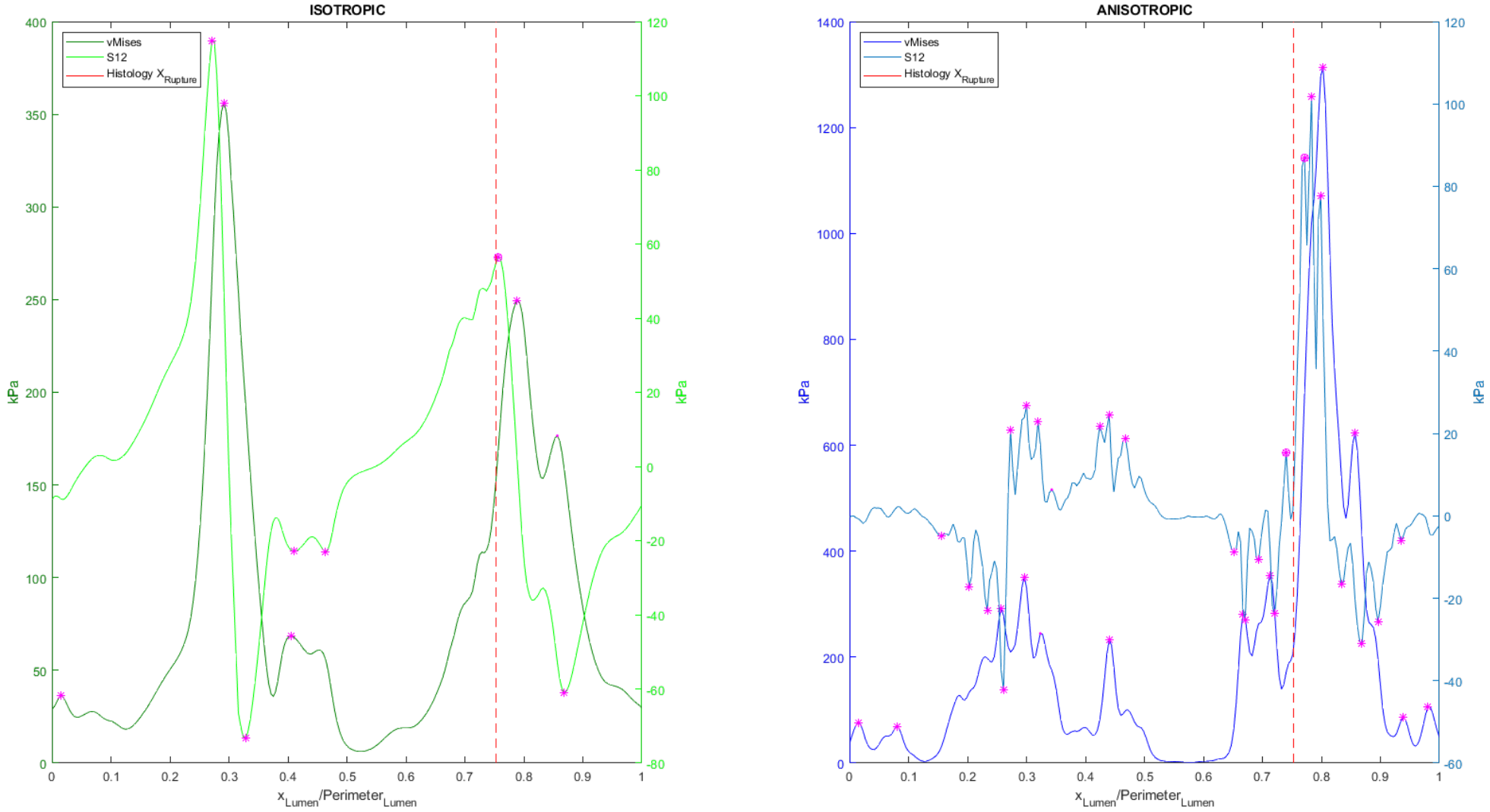

Figure 3.3: Lumen-path values for von Mises (left y-axis) and shear stress (right y-axis) at 140mmHg blood pressure. Distance along each path (x-axis) is presented using a path length-normalised unit. Both isotropic (upper panels) and anisotropic (lower panels) plaque-model results are presented per path. Damage-sites are indicated by a dashed vertical line, red for ruptures, cyan for fissures. Magenta indicates peaks: dots are non-noise peaks, asterisks meet the $> 15\%$ prominence requirement, and circled asterisks represent 'hits' (peaks within 10° of a damage site).

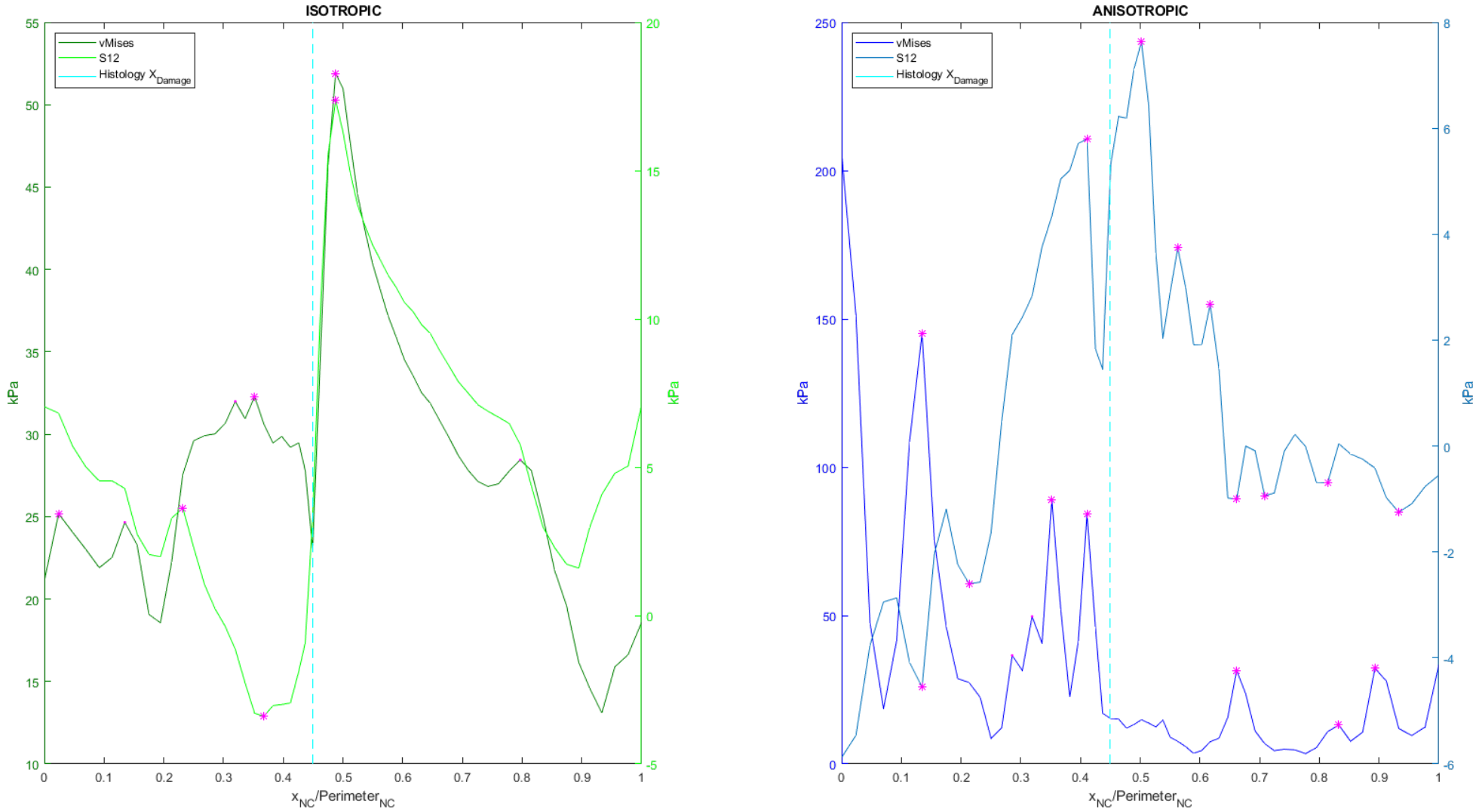

Figure 3.4: NC1-path values for von Mises (left y-axis) and shear stress (right y-axis) at 140mmHg blood pressure. Distance along each path (x-axis) is presented using a path length-normalised unit. Both isotropic (upper panels) and anisotropic (lower panels) plaque-model results are presented per path. Damage-sites are indicated by a dashed vertical line, red for ruptures, cyan for fissures. Magenta indicates peaks: dots are non-noise peaks, asterisks meet the $> 15\%$ prominence requirement, and circled asterisks represent 'hits' (peaks within 10° of a damage site).

3.2 Observations from Histology and FEM Outputs (all cases)

3.2.1 Fibre-Architecture

Visual inspection of the histology cross-sections, their corresponding fibre-plots, and dispersion maps distilled the following observations on fibre-distribution:

First, fibres are primarily circumferentially-oriented; i.e. they tend to encircle the lumen. This tendency decreased abluminally: fibres further from the lumen tended to be less well circumferentially-aligned. By corollary, dispersion-values nearer the lumen tended to be lower than those farther away (see fig. 2.1e or A.3).

Second, besides the lumen, fibre encircling inclusions was also observed (see D.1). As with the lumen, this tendency decreased abluminally: greater alignment/lower dispersion-values were observed on the abluminal side of the inclusion. It is worth noting that these observations were sometimes confounded close to necrotic cores because adjacent pathological necrosis or inflammation - where present - led to higher dispersion values. Overall, lumen-encirclement dominated inclusion-encirclement: inclusion-parallel fibre angles were only observed close to inclusion boundaries, and transverse (i.e. juxtaluminal) fibre orientations were less common.

Third, a novel fibre feature - 'vortices' - arose when the lumen- and inclusion-encircling tendencies conflicted (see D.2). Specifically, vortices arose when non-circumferential fibre-group(s) encircling an inclusion met a lumen-encircling fibre-group, resulting in a mixed fibre-orientation region with higher dispersion: a 'vortex'. This was frequently observed at inclusion shoulders where three fibre-groups met - the lumen-encircling fibre, the adluminal inclusion-encircling fibre, and the abluminal inclusion-encircling fibre - leading to the triangular vortex-regions (see fig. D.2). Cross-referencing of vortex-regions with FEM output fields and histology revealed locally elevated metric-values (e.g. the 9o'clock region of the example case A.1, A.3, and B.2) and, when close to damage-sites, propagating cracks/damage (e.g. D.2).

Fourth, another damage-prone fibre feature was observed: non-circumferential fibre 'channels'. 'Fibre-channels' refer to the fibre-aligned path defined by extended regions of (relatively) low-dispersion fibre. When not aligned circumferentially, fibre-channels precipitated elevated metric-values, predisposing them to damage (see anisotropic fig. 3.1 and 3.2 or app. B.2). Damage propagated along fibre-channels was frequently observed near large or juxtaluminal inclusions whose encircling fibre groups became non-circumferential (e.g. northmost damage path in fig. D.1).

Fifth, damage usually occurred via delamination-modes[3] (see fig. D.2), though tearing-modes[4] were sometimes observed in luminal inclusion caps (fig. D.4). Furthermore, damage propagating through the plaque (along the aforementioned fibre-channels) was exclusively delamination-based. Overall, damage-events were often mixed-mode: luminal tears which propagated to an inclusion via delamination were frequently seen (e.g. figs. A.1).

Lastly, well-aligned fibre was observed in undamaged thin caps (e.g. D.5).

Inflammation and Fibre-Dispersion

It was observed that suspected inflammation regions - identified by the presence of eosinophilic nuclei - invariably presented with higher dispersion-values. This was often observed in pathological tissue adjacent to necrotic cores, as well as in inflamed caps.

[3] 'Delamination' refers to damage-modes where fibres peel away from one another, either due to shear- or fibre-perpendicular (transverse-) forces, leaving a gap between the intact fibres.

[4] 'Tearing' refers to damage-modes where fibres are ripped apart due to tensile force along the fibre-parallel (longitudinal) direction, leaving a gap between the remaining damaged fibre-pieces.

3.2.2 Damage-Modes

Inspection of damage-sites revealed delamination and tearing damage-modes, frequently in tandem (mixed-mode). Mixed-mode damage was seen most frequently, typically in the form of a few torn fibres at the lumen accompanied by intraplaque delamination (fig. D.2). Delamination-only damage was frequently observed at inclusional damage-sites, where fibres peeled away from the inclusion. Damage then propagated through fibre-channels via delamination (fig. D.1. Tearing-only damage was sometimes seen in thin-caps (fig. D.4), though mixed-mode damage was also common in caps (fig. A.1). Tearing-only typically favoured mid-cap rupture rather than shoulders and was often associated with inflammation and low-dispersion values in the cap.

3.3 Statistical Results (all cases)

3.3.1 Metric Correlations

Figures 3.5 and 3.6 below present average within-model and cross-model correlation coefficients for all permutations of the twelve mechanical metrics. Corresponding p-values can be found in app. E

The isotropic within-model correlations reveal two correlated groups: the shear direction ($S12-LE12$) and everything else (allowing for $S22$'s moderate correlations with other stresses). The anisotropic within-model correlations are similar, but see a third group separate itself from the rest: that of the strains $LE11$ and $LE22$. Note also the perfect negative correlation between $LE11$ and $LE22$, which reflects the material incompressibility assumption made during FEM construction.

The cross-model correlations between isotropic and anisotropic metrics show little correlation overall. There are two groups of exceptions: first, $vMises/MaxIPP/S11$ and the energy metrics, which are strongly to moderately correlated cross-model; second, $S11/LE11/LE22$, which share moderate correlations with each other and the previous group.

Within-Model Correlations													
	Anisotropic / Isotropic	Stress					Strain				Energy		
		vMises	SMaxIPP	S11	S22	S12	LEMaxIPP	LE11	LE22	LE12	ELSE	ESEDEN	SENER
Stress	vMises		0.9528	0.7105	-0.0094*	0.0484	0.6661	0.1836	-0.1836	0.0517	0.7744	0.8570	0.8461
	SMaxIPP	0.9708		0.7987	0.0712	0.0520	0.5514	0.2974	-0.2974	0.0546	0.7115	0.7781	0.7532
	S11	0.9306	0.9760		-0.2121	0.0546	0.2229	0.5461	-0.5461	0.0444	0.4422	0.4726	0.4917
	S22	0.3307	0.4023	0.3339		-0.0011*	0.1814	-0.3078	0.3078	0.0134	0.1510	0.1548	0.0192
	S12	-0.0185	-0.0218	-0.0168	-0.0179		0.0503	0.0281	-0.0281	0.8527	0.0514	0.0538	0.0599
Strain	LEMaxIPP	0.9736	0.9492	0.8975	0.3859	-0.0081*		-0.4150	0.4150	0.0637	0.7977	0.9033	0.8944
	LE11	0.6879	0.7314	0.8098	0.0483	-0.0106*	0.6574		-1.0000	0.0058*	-0.1401	-0.1352	-0.1155
	LE22	-0.6879	-0.7313	-0.8098	-0.0482	0.0106*	-0.6574	-1.0000		-0.0058*	0.1401	0.1352	0.1155
	LE12	-0.0223	-0.0260	-0.0229	-0.0117*	0.9793	-0.0089*	-0.0187	0.0187		0.0589	0.0617	0.0646
Energy	ELSE	0.8538	0.8452	0.8089	0.3281	-0.0016*	0.8547	0.6750	-0.6749	-0.0071*		0.8764	0.8488
	ESEDEN	0.9845	0.9653	0.9197	0.3807	-0.0160	0.9913	0.6905	-0.6904	-0.0184	0.8661		0.9587
	SENER	0.9873	0.9644	0.9184	0.3626	-0.0151	0.9910	0.6891	-0.6890	-0.0176	0.8679	0.9981	

Figure 3.5: Within-model ranked correlation coefficients for the twelve metrics (averages across all sections). Isotropic plaque-model results are presented in the lower-left triangle, anisotropic results in the upper-right. Colours indicate the degree of correlation: Green: Strong ($|r| > 0.7$); Yellow: Moderate ($0.7 > |r| > 0.3$); Red: Weak ($0.3 > |r|$). Asterisks (*) indicate a p-value ¿ 0.05. The absent diagonal entries were identically unit-valued auto-correlation coefficients.

Cross-Model Correlations													
Anisotropic ↓		Isotropic →	Stress					Strain				Energy		
			vMises	SMaxIPP	S11	S22	S12	LEMaxIPP	LE11	LE22	LE12	ELSE	ESEDEN	SENER
Stress	vMises		0.7202	0.7275	0.7053	0.2535	-0.0197	0.7094	0.5188	-0.5188	-0.0153	0.6532	0.7144	0.7153
	SMaxIPP		0.7170	0.7601	0.7472	0.3082	-0.0197	0.7060	0.5467	-0.5467	-0.0150	0.6599	0.7133	0.7132
	S11		0.4849	0.5375	0.5443	0.2134	-0.0227	0.4740	0.3968	-0.3968	-0.0142	0.4549	0.4768	0.4801
	S22		0.1299	0.1581	0.1511	0.1485	0.0138	0.1322	0.0998	-0.0998	0.0102*	0.1398	0.1378	0.1325
	S12		0.0613	0.0654	0.0646	0.0147	-0.0074*	0.0595	0.0581	-0.0581	-0.0069*	0.0539	0.0653	0.0641
Strain	LEMaxIPP		0.6048	0.5563	0.5057	0.1716	0.0209	0.5978	0.3483	-0.3484	0.0163	0.5440	0.6019	0.6008
	LE11		0.0493	0.1074	0.1448	0.0381	-0.0413	0.0437	0.1366	-0.1366	-0.0271	0.0112*	0.0423	0.0456
	LE22		-0.0493	-0.1074	-0.1448	-0.0381	0.0413	-0.0437	-0.1366	0.1366	0.0271	-0.0112*	-0.0423	-0.0456
	LE12		0.0696	0.0735	0.0711	0.0166	-0.0174	0.0676	0.0616	-0.0616	-0.0177	0.0603	0.0727	0.0714
Energy	ELSE		0.6577	0.6435	0.6105	0.1980	0.0089*	0.6472	0.5077	-0.5077	0.0065*	0.8083	0.6573	0.6582
	ESEDEN		0.7280	0.6960	0.6517	0.2084	-0.0035*	0.7163	0.4527	-0.4527	-0.0024*	0.6449	0.7209	0.7201
	SENER		0.6901	0.6552	0.6126	0.1841	0.0002*	0.6770	0.4307	-0.4307	0.0010*	0.6163	0.6808	0.6818

Figure 3.6: Cross-correlation coefficients for the twelve metrics (averages across all sections). Isotropic-model metrics are presented across, anisotropic-model metrics top-to-bottom. Colour-coding and asterisks are used as for the within-model correlations in fig. 3.5. Diagonal entries in this table are not unit-valued because they are not auto-correlations (since they are cross-model).

3.3.2 Metrics' Damage Sensitivity

The table below (fig. 3.7) presents overall rupture- and fissure-sensitivity results for all twelve metrics in both isotropic- and anisotropic-plaque FEM variants. Further stratifications for inclusion type, depth, and combinations thereof can be found in appendix F.

Metrics' Damage Sensitivity: 'Hit-Rates' for Ruptures and Fissures

Plaque Model	Metric	vMises	SMaxIPP	S11	S22	S12	LEMaxIPP	LE11	LE22	LE12	ELSE	ESEDEN	SENER
	Ruptures (n_R = 43)												
	ISO	51%	51%	51%	63%	65%	56%	63%	72%	74%	51%	54%	51%
	ANISO	70%	67%	81%	84%	81%	91%	95%	95%	98%	56%	60%	84%
	Fissures (n_F = 124)												
	ISO	50%	51%	56%	65%	60%	52%	67%	71%	70%	52%	41%	48%
	ANISO	65%	65%	73%	85%	75%	69%	87%	84%	85%	55%	54%	65%

Figure 3.7: Metrics' Sensitivity Results for all ruptures (upper) and fissures (lower). The 'hit-rates' (true-positive incidence) are presented as percentages and colour-coded for readability: Red (0-40%), Yellow (40-70%), Light Green (70-85%), Dark Green (>85%)

The best predictor for plaque rupture was shear strain ($LE12$) using an anisotropic plaque model, which had a 98% hit-rate. Furthermore, all anisotropic-model strains had hit-rates over 90%. Behind the strain metrics, in spite of reliable hit-rates over 80%, were fibre-parallel ($S11$), fibre-perpendicular ($S22$), and shear ($S12$) stress; not to mention strain energy density with respect to current volume (SENER). On the other hand, the performance of isotropic plaque model metrics was significantly worse: the best isotropic predictor of plaque rupture was also shear strain, but now with a 74% hit-rate. The only other isotropic-model metric with over 70% sensitivity was transverse strain ($LE22$). The remaining isotropic metrics' performance, though never poor, were consistently mediocre (50-70% sensitivity).

As for plaque fissure, the best predictor was fibre-parallel strain ($LE11$) using the anisotropic plaque model variant, which was 87% sensitive. Close runners-up were anisotropic-model shear strain ($LE12$) and fibre-perpendicular stress ($S22$) and strain ($LE22$), which were 85% sensitive ($LE22$: 84%). As was the case with ruptures, isotropic-model metric sensitivity was significantly worse, with the best metrics - $LE22$ and $LE12$ - achieving 71% and 70% sensitivity respectively. The remaining isotropic metrics, like before, were consistently mediocre (40-70% sensitivity).

Thus, anisotropic-model metrics predicted damage better than their isotropic counterparts (typically with $\Delta \approx 20 - 30\%$). This discrepancy grew further in the case of luminal damage sites with deep inclusions ($\Delta \approx 20 - 40\%$, see figs. F.1 and F.2), luminal damage sites with superficial hard inclusions ($\Delta \approx 15 - 50\%$, see figs. F.1 and F.2), and fissure sites at superficial soft inclusions ($\Delta \approx 15 - 70\%$, fig. F.3). Conversely, the discrepancy lessened for the TCFA cases: luminal damage sites with a superficial soft inclusion ($\Delta \approx 0 - 20\%$, see figs. F.1 and F.2).

Moving from plaque-model variants to metric-types, strain metrics were best for predicting damage (see figs. 3.7). Stress metrics' overall performance followed closely behind, however this comparison is complicated by a significant case-dependence: stress metrics either matched strains' performance ($\Delta \approx 0 - 10\%$) - in cases with soft inclusions (fig. F.1, F.2, and F.3) - or performed significantly worse ($\Delta \approx 0 - 50\%$) - in cases with hard or no inclusion (see fig. F.1, F.2, and F.3) and cases with deep inclusions (when using an isotropic plaque-model, see

fig. F.1, F.2, and F.3). Not to mention, transverse or fibre-perpendicular stress ($S22$) often overperformed, matching or sometimes exceeding the sensitivity of strain metrics. Energy metrics' performance was straightforwardly poor by comparison to strains ($\Delta \approx 15 - 35\%$) or stresses ($\Delta \approx 10 - 30\%$, see fig. F.1, F.2, and F.3)). The only exception was the small number of no-inclusion rupture cases ($n_{RLNo} = 2$) where energy metrics' sensitivity matched strains' (see fig. F.1, F.2, and F.3)).

Another perspective to consider is directionality, in which regard shear and transverse/fibre-perpendicular (12 and 22) directions tended to perform best, followed by the circumferential/fibre-parallel direction (11), and trailed by von Mises (vMises) and maximum in-plane principal (-MaxIPP) metrics. Similar to before, the comparison of shear and transverse directions to the circumferential direction is often case-dependent: the circumferential/fibre-parallel-direction matches or exceeds shear/transverse metrics in several cases[5].

Besides those mentioned above regarding plaque-model, metric-type, and directionality, the sensitivity results also facilitated the following overarching observations: first, rupture sensitivity was greater than damage sensitivity ($\Delta \approx 0 - 20\%$, fig. 3.7); second, soft inclusion damage sensitivity tended to be greater than hard inclusions' ($\Delta \approx 0 - 40\%$, see fig. F.1, F.2, and F.3); third, sensitivity for fissures with superficial inclusions tended to be better than for deep inclusions ($\Delta \approx 10\%$, see fig. F.2 and F.3).

3.3.3 Metric Strength Thresholds

The following tables (3.1) present average local (i.e. within $\pm 10^\circ$ neighbourhood) metric values (at 140mmHg blood pressure) for rupture and fissure sites at the lumen. These values can be interpreted as strength/damage threshold values *modulo* 140mmHg[6]. Similar tables for damage sites at necrotic cores and calcifications can be found in Appendix G.1.

[5]Anisotropic-model hard-inclusion ruptures (see fig. F.1), soft- and no-inclusion luminal fissures (see fig. F.2), and hard-inclusion fissures (fig. see fig. F.2 and F.3).

[6]Interpreting these values as strengths/damage thresholds comes with an important caveat: they assume that damage occurred *at* 140mmHg of pressure. Although this assumption is unsupported, undermining the values' accuracy, it does not preclude their indicative worth. Damage threshold values - accurate or not - are lacking in the literature, despite being crucial for damage-modelling techniques (e.g. XFEM). Thus, these values based on 140mmHg (a widely accepted value for pathological systolic pressure) may provide an essential starting-point for further studies.

Strength Threshold-Values

Ruptures			
		Isotropic	Anisotropic
Stress [kPa]	vMises	153*	198*
	SMaxIPP	156*	151*
	S11	134*	111*
	S22	14*	19
	S12	40*	13*
Strain [%]	LEMaxIPP	6.6	5.5
	LE11	4.6	1.7
	LE22	4.6	1.7
	LE12	6.9	4.3
Energy	ELSE [mJ]	0.0082*	0.003788*
	ESEDEN $[\frac{mJ}{mm^3}]$	3.9*	1.8*
	SENER $[\frac{mJ}{V_e}]$	4.3*	2.1*

Fissures			
		Isotropic	Anisotropic
Stress [kPa]	vMises	144*	220*
	SMaxIPP	134*	175*
	S11	118*	142*
	S22	20*	26
	S12	27*	13*
Strain [%]	LEMaxIPP	6.2	4.8
	LE11	4.3	1.6*
	LE22	4.3	1.6*
	LE12	5.4	4.5*
Energy	ELSE [mJ]	0.0070*	0.0042*
	ESEDEN $[\frac{mJ}{mm^3}]$	2.9*	1.8*
	SENER $[\frac{mJ}{V_e}]$	3.4*	2.1*

Table 3.1: Rupture and Fissure Strength Thresholds per metric, estimated using Isotropic and Anisotropic models. Asterisks indicate coefficients of variance > 1

Chapter 4

Discussion

This section follows the results' order of presentation: FEM results first, followed by histological observations and FEM-derived statistical outcomes. The latter include metric correlations, damage-sensitivities, and strength-threshold values.

4.1 FEM Outputs

4.1.1 Output Fields

The isotropic and anisotropic FEM-results - having the primary plaque-mechanical determinants in common - were more similar than not. However, differences arose by virtue of the mechanical determinant they did not share: fibre.

However, before mechanics, an apparent difference between the FEM-results should be addressed: the anisotropic FEM-results were markedly less smooth than their isotropic counterparts (also noted by Douglas in [51]). This was caused by the implementation of per-element dispersion and orientation parameters, which could give rise to different material behaviour in adjacent elements. In some cases - those where the element-bounds aligned with fibre-edges - this accurately reflected the fibre-distribution. However, there were also cases where sharp discontinuities arose in smoothly-transitioning fibre regions due to the discrete element-wise variations in fibre-dispersion (κ). Hence, future implementations of this method could be improved by implementing smoothing across adjacent elements[1].

Mechanically, as a result of their shared mechanical determinants, the isotropic and anisotropic FEM-results were more similar than not. Firstly, both models had abluminally-decreasing (stress) metric values (fig. 3.1 or app. B) by virtue of the blood pressure loading at the lumen. Secondly, both models had elevated metric-values corresponding to established morphologically-vulnerable features: thin caps, cap shoulders, large inclusions, high-curvature boundaries, and juxtaluminal inclusions [27, 36, 84, 85]. Third, both models showed elevated metric-values due to compliance mismatches (including shielding by hard inclusions). Thus, the implementation of fibre did not undermine established mechanical determinants - rather, fibre was a secondary determinant.

Fibre, though a secondary determinant, gave rise to important mechanical differences in the anisotropic FEM results. It does so due to its directional stiffness: fibre reduces strains ($LE11$) and increases stresses ($S11$) along the fibre-axis. As a result, the fibre-architecture (fig. A.2

[1]Note that implementing 'smoothing' would not be straightforward: cases where an abrupt transition accurately reflects the fibre-distribution would have to be distinguished from false discretisation-effects. At first glance, using smaller elements seems like an alternative solution. However, in order to be effective, this reduction would have to be taken to the micro-structural level, which is at odds with the current methodology: the HGO material model's dispersion parameter is computed from a population of fibres using statistical methods. Alternatively, it would be possible to forgo the HGO material model in favour of a microstructural model. However, this would require determining corresponding microstructural material models (necessitating per-fibre mechanical testing), not to mention a significant increase in computational costs and change of method.

or 2.1c) significantly modifies the metric-values throughout the plaque. These 'fibre-effects' reveal novel mechanical phenomena in the plaque: fibre-shielding, damage propagation along fibre-channels, vulnerable fibre-vortices, and deep intraplaque hotspots.

'Fibre-shielding' refers to the accumulation of stress in regions of low dispersion fibre, leading to a reduction of stress in neighbouring 'shielded' plaque-regions. Examples of fibre-shielding can be seen in the inclusion caps of fig. 3.1: whereas the isotropic variant showed moderate to high stresses throughout the caps, the anisotropic variant's caps showed localised regions of high and low stress. Specifically, the thin NC1 cap contained an elongated high-stress region - corresponding to a region of low-dispersion fibre (see fig. A.3 or 2.1e) - which led to lower stresses at the (vulnerable) NC1 boundary than in the isotropic variant. Although this particular case ruptured nonetheless, the study population also contained examples of thin-caps with low-dispersion fibre which resisted rupture (fig. D.5). Rupture-resistant thin caps, which defy the 'vulnerable thin-cap' hypothesis and traditional isotropic modelling results, have also been reported in the literature ([45, 46]); perhaps fibre is the missing factor. Thus, dispersion as a marker for plaque-vulnerability is an interesting avenue for further study (also proposed by Douglas [51]). Moving on to the thicker NC2 and NC3 caps, shielding did not reduce stress directly on the inclusion boundary in these cases but did lead to low-stress zones in the cap, relative to greater stresses seen throughout the isotropic-model cap. Again, this suggests that fibre may stabilise vulnerable caps. However, high stresses at the inclusion boundary leave room for damage at the inclusion, which may be a damage-mechanism related to inclusion growth and/or inclusion-initiated damage (see initiation at the inclusion in fig. D.6).

Next, a 'fibre-channel' refers to an elongated region of low-dispersion fibre. Especially when non-circumferentially aligned, they locally elevated metric-values, precipitating damage (see the elevated anisotropic metric-values extending from the rupture site across NC1 and in front of NC3 in anisotropic figs. 3.1, B.4, and B.5). Cross-referencing with the dispersion map confirms that fibre-channels corresponds to regions of low-dispersion fibre (see fig. A.3). Furthermore, intraplaque damage propagation exclusively followed fibre-channels (previously observed by [64], see figs. A.1, D.1, and D.2).

Third, fibre 'vortices' arose when the lumen- and inclusion-encircling tendencies conflicted (see D.2). A common observation was triangular vortices (reported by Douglas in [51]), formed where three fibre-groups met - lumen-encircling fibre, adluminal inclusion-encircling fibre, and abluminal inclusion-encircling fibre (see fig. D.2). As a result of the various fibre-orientations surrounding a vortex, they often gave rise to elevated metric-values (e.g. the 9o'clock region of the example case A.1, A.3, and B.2), predisposing them to damage (as speculated by Douglas [51]). Vortex-formation frequently occurred at plaque shoulders, perhaps contributing to the well-established vulnerability of plaque-shoulder regions [27, 33, 36].

Deep intraplaque hotspots - the last fibre-phenomenon observed - refer to elevated metric-values deep in the plaque. They were not observed in isotropic-model results, but were commonplace in the anisotropic-model results which implemented true fibre-distributions. Examples can be seen at the five and eight o'clock positions in all the anisotropic-model metric-fields, as well as on the abluminal side of inclusions (see Appendix B.2 or the earlier figs. 3.1, 3.2). The emergence of deep metric hotspots after implementing fibre may provide the missing mechanical etiology for reports of damage initiation deep within the plaque [27, 64] and at deep inclusion boundaries (even at the abluminal side) [64].

4.1.2 Path Data

The path data (figs. 3.3 and 3.4 or - for all metrics - app. C) corroborated observations drawn from the output fields regarding the mechanical determinants. Thus, values along inclusion-paths were lower than those along the lumen and local maxima were observed at high-curvature points.

Fibre-shielding effects manifested through relatively higher anisotropic stress values (except

$S12$), since fibre tended to be well-aligned parallel to inclusion- and lumen-boundaries. Correspondingly lower anisotropic strain ($LE11/22$, not shear $LE12$) and energy-metric values were observed.

The sharp transitions (due to element-wise fibre parameters) in anisotropic data were also visible in the path data. To ameliorate this, Gaussian smoothing was applied to the anisotropic path data results[2]. Furthermore, maxima analysis on the path data enforced a local ($\pm 10°$ neighbourhood) prominence requirement (15%) to preclude false-positives due to discretisation-related peaks.

Maxima analysis on the path data also granted insight into the importance of plaque-heterogeneity with regards to damage. Namely, while local maxima tended to exist near damage-sites (see figs. 3.3 and 3.4 app. C), they were not necessarily the global maximum metric-value in the plaque[3]. Thus, besides locating maxima, identifying vulnerable features and/or mapping local plaque-strengths is crucial to predicting plaque-damage (as noted by [36, 50]).

4.2 Histological Observations

4.2.1 Fibre Architecture

The computational objectivity of the fibre plots and dispersion maps facilitated the observation of morphological principles governing plaque fibre distribution: First and foremost, fibres were predominantly circumferentially oriented, in alignment with the primary direction of deformation in the plaque[4]. Furthermore, the observation of lower dispersion values nearer the lumen (and at inclusion boundaries) confirms that well-aligned fibre accumulates where stresses are greatest (before fibre-development, as these regions are also hotspots in isotropic models). Based on these observations, it seems reasonable to speculate that a mechano-sensitive model (similar to Wolff's Law for other collagenous tissues) governs plaque fibre distribution: where there is load, there is fibre [86].

However, the mechanical simplicity of 'where load, there fibre' is complicated by the pathological features in atherosclerotic plaques: Inclusions and inflammation (which degrades fibre) create vulnerabilities in the plaque [86]. Established examples include soft inclusions [36], high-curvature material boundaries [36], juxtaluminal inclusions [36, 85], thin caps [36, 84], and inflamed (low dispersion[5]) plaque regions [27, 48]. These were (re-)confirmed by this study. In addition to these established cases, cross-examination of histology sections with fibre plots and dispersion maps also brought to light new fibre-based predictors for plaque damage: fibre 'vortices' and 'channels'. These were observed when the inclusion-encircling tendency interrupted the dominant circumferential distribution. Both cases led to mechanical metric (stress/strain/energy) hotspots, thereby improving the damage sensitivity of the anisotropic FEM results.

Inflammation and Vulnerability

Besides these global observations, inspection of the sections and dispersion maps on the local scale revealed a strong association between tissue inflammation and fibre-dispersion. Since greater dispersion leads to reduced material strength - all other things equal - this suggests

[2]Path data being at inclusion/lumen boundaries precludes the error of smoothing across a fibre-edge, which was why smoothing of output fields was forgone

[3]Not including quantitative analysis of global and local (95%CI neighbourhood) maxima frequency is an unfortunate oversight of this study that future iterations should seek to rectify.

[4]The primary circumferential fibre-orientation was also confirmed by the moderate correlation coefficient between circumferential stress in isotropic models and fibre-parallel stress in anisotropic models (see fig. 3.6).

[5]the link between inflammation and low-dispersion was established in the current study and previously speculated on by Douglas [51]

that dispersion may be the link between inflammation and plaque-vulnerability; a relationship previously observed [27, 48] but not yet explained from a mechanical perspective. What's more, this link would explain why necrotic cores are typically more vulnerable than intra-plaque haemorrhage or calcification: necrotic cores are most strongly linked to adjacent tissue inflammation [87] and thus fibre degradation-related strength-loss [48]. Indeed, observation of the dispersion maps showed higher dispersion in the vicinity of necrotic cores, but not intra-plaque haemorrhage or calcification. With these connections in mind, investigating the link between dispersion and plaque-vulnerability would be a worthwhile avenue for future study.

4.3 Statistical Analyses

4.3.1 Correlation Analysis

Isotropic within-model correlation coefficients revealed two highly-correlated groups: the shear metrics ($S12/LE12$) and 'the rest'. The high correlation across most isotropic metrics reflects the monotonic mechanical relationships between stress, strain, and energy; unmodified by directional preferences. Thus, stress, strain, and energy metrics can be used more or less interchangeably when considering an isotropic plaque model. Exceptions to this heuristic were transverse stress ($S22$, as warned by Holzapfel et al. [32]) and the shear metrics ($S12/LE12$). Transverse stress was only moderately correlated to 'the rest', perhaps due to modification by the hydrostatic pressure term as it upheld the imposed incompressibility relation between $LE11$ and $LE22$. This would explain why $S22$ and $LE22$ were poorly correlated while $S11$ and $LE11$ were highly correlated, in spite of there being no underlying directional discrepancy in the isotropic plaque-model. As for the shear metrics, these did not correlate with 'the rest' because the shear-direction is significantly dependent on geometry, not just the applied load (as reflected by less abluminal-dependence in figs. 3.2).

Anisotropic within-model correlation coefficients saw a third correlated group separate itself: the group of strains ($LE11/LE22$, LE_{MaxIPP} to a moderately-correlated extent). This reflects the influence of fibre: directional stiffness modifies the mechanical relationship between stress and strain such that they are no longer strongly correlated. Alternatively, increased geometrical dependence may be the culprit. Furthermore, the remaining correlations in the 'the rest'-group are lower in the anisotropic models than the isotropic models. Thus, the interchangeability of stress, strain, and energy no longer applies when fibre is implemented in the plaque model.

Low cross-model correlation coefficients overall showed that implementing fibre significantly alters plaque-mechanics. The few high-valued cross-model coefficients - vMises, MaxIPP, and the energy metrics - reflect that fibre-effects, though significant, do not override primary determinants such as loading direction or geometry.

4.3.2 Sensitivity Analysis

This study improved upon the lineage of studies ([34, 35, 49, 50]) demonstrating the utility of mechanics for predicting plaque damage: it examined a greater number of mechanical metrics, used stricter constraints[6], and used a large (sensitivity) study population; eventually achieving rupture and fissure sensitivities of 98% (anisotropic $LE12$) and 87% (anisotropic $LE11$) respectively. The rupture sensitivity result has great clinical promise because strain values - contrary to stress - can be obtained from established vascular deformation imaging modalities. On the other hand, the fissure result has scientific value because it addresses a niche in the literature: fissures are less well-studied because it is difficult to guarantee that damage occurred in vivo without interstitial erythrocytes. However, the high sensitivity results achieved in this study (which modelled in vivo loading) would be unlikely if the fissures had been created artificially, e.g. while processing the tissue for histology examination. Thus, the results lend credence to

[6]Relatively small neighbourhood-size ($\pm 10°$) and prominence-threshold maxima analysis

the notion that fissures may occur in vivo - at the lumen or either side of an inclusion [64] - corroborating reports of intraplaque fissure [27, 64, 87].

Further insights into plaque mechanics were gleaned by viewing the sensitivity results through different vignettes: isotropic versus anisotropic plaque model, fibre-aligned versus - normal/-shear, and stress versus strain versus energy.

Comparing isotropic to anisotropic sensitivity results highlighted the importance of implementing fibre, as anisotropic sensitivities exceeded isotropic sensitivities by 20% or more across the board. Moreover, this discrepancy grew further for fissure-sites at superficial (thin-cap) soft inclusions and luminal ruptures/fissures with deep inclusions or superficial hard inclusions. The thin-cap cases were explained by fibre-shielding effects relocating metric hotspots in the cap (as seen in fig. 3.1). Second, the deep inclusion cases were explained by fibre-channels giving rise to deep metric hotspots (see deep hotspots around NC2 in anistropic but not isotropic output in fig. 3.1). Third, the superficial hard inclusion cases were explained by fibre-shielding, which was necessary to generate hotspots in these thin caps which were otherwise shielded by the nearby hard inclusion (a compliance-mismatch effect). In the isotropic models, this hard inclusion-shielding effect (unmodified by fibre) led to a reduction of stresses D.7 in the cap, reducing the isotropic metrics' sensitivity. It follows that isotropic modelling of thin caps over hard inclusion might unsoundly imply a cap-stabilising effect of hard inclusions, drawing this result from isotropic modelling studies [88] into question.

Conversely, there were two plaque morphologies where isotropic sensitivities matched (but did not exceed) anisotropic ones: luminal ruptures in plaques without inclusions and luminal fissures in superficial soft inclusion caps. The former no-inclusion cases' fibre-indifference may be explained by the dominance of geometry instead. Furthermore, many fibre-effects were observed accompanying inclusions (channels, vortices, shielded caps), which were absent in these cases. However, more cases than the current two would need to be considered to draw robust conclusions. Next, the luminal fissures (*not* ruptures) at superficial soft inclusions - the vulnerable TCFA morphology. For these cases, their fibre-indifference could be explained by the absence of well-aligned fibre in the TCFA caps. However, the same held true for TCFA-ruptures, which *did* favour anisotropic metrics. Given just five luminal TCFA fissures were observed, the latter finding (based on fifteen cases) should take precedent.

Comparing directional metrics' sensitivities gave further insight into the damage-modes in atherosclerotic plaques: delamination and tearing. The transverse (22) and shear (12) metrics (delamination-related) matched or slightly outperformed the fibre-aligned (11) metrics (tearing-related) across most damage-cases. This result might imply that delamination is slightly more prevalent than tearing, except that both modes often performed well simultaneously, indicating mixed-mode damage. These results align with observations of corresponding histological sections, which revealed that delamination and tearing often co-exist in the vicinity of damage-sites: typically in the form of a luminal-tear and intraplaque delamination. It is not clear whether a luminal tear precipitated delamination (perhaps assisted by penetrating blood) or if intraplaque delamination propagated (along fibre-channels) to the lumen, facilitating tearing of the (few) remaining fibre(s); the order of events cannot be gleaned from the histology-snapshots. Besides mixed-mode damage-cases, the study population also frequently included delamination-only damage at inclusions - reflected by superior deep-inclusion sensitivity of delamination metrics (see 22 and 11 in fig. F.3) - and sometimes included tearing-only damage in thin-caps - *not* reflected by superior sensitivity to superficial ruptures (fig. F.1) or fissures (figs. F.2 and F.3). However, this might be explained by 12 and 22 metric-peaks coinciding with 11 peaks in thin-caps regardless of the damage-mode at play, since geometrical and compliance mismatch are primary determinants in this case [36]. Overall, the transverse- and shear-metrics' slightly greater sensitivity may be explained by their exclusive sensitivity to delamination at inclusions and sensitivity to thin-cap damage regardless of the specific damage-mode (tearing or mixed).

Ultimately, the histological observations and sensitivity-results show that while most plaque

damage - all propagation and some initiation - involves delamination, tearing plays a critical role in cap-damage. These findings support the traditional focus on tearing-modes, but also grant newfound importance to delamination-modes for explaining intraplaque damage events and damage-propagation. Furthermore, the observation of delamination-only damage begs the question of what comes first: tearing at cap/lumen, or deep plaque delamination which propagates towards a terminal tear at the lumen?

Comparing metric types' - stress, strain, and energy - sensitivities revealed that strain metrics are most sensitive to damage. Stress metrics followed closely, sometimes matching strains, while energy trailed far behind.

The stress/strain sensitivity discrepancy shows that stress and strain are not just two sides of the same coin. Though related by stress-strain relationships, those relationships are non-linear in the case of plaque [89], precluding their equivalence. Furthermore, the current models included multiple material models and complex geometry, additional factors which may displace strain- from stress-maxima. In practice, it was observed that - regardless of fibre-implementation - the strain metric peaks fell within the sensitivity-neighbourhood slightly more often stress metrics'.

The low sensitivity of energy metrics makes them unsuitable for short-term damage prediction using clinical imaging. Additionally, it might seem like an argument against fatigue-based damage-modes. However, it should be noted that material fatigue is typically associated with cyclic loading conditions [69] (like systole/diastole *in vivo*), which were not modelled in this study (quasi-static loading). Furthermore, plaque fatigue is also influenced by healing, inflammation, and pathology *in vivo*, which are interactions beyond the scope of the current study. Therefore, this study can only conclude that energy metrics are unsuitable for short-term damage-prediction.

4.3.3 Strength Analysis

Although the strength values (modulo 140mmHg) obtained in this study were indicative rather than precise, their relative magnitudes and variances offered insights nevertheless. For instance, plaque strength values were greatest at the lumen, then at calcified inclusions, then necrotic cores. This supports previous findings that inclusions are vulnerable to damage ([27]), and necrotic cores foremost ([27, 36]). Regarding variances, strain metric failure thresholds tended to have lower variances than stress or energy, while $S22$-strength had the lowest variance of all. This result corroborates earlier discussions of the (stress) confounding effects of fibre-shielding. Lastly, noting that rupture-variances were comparable to fissure-variances suggests that the fissures indeed occurred in vivo rather than as a result of manipulations ex vivo.

4.4 The Best Metric?

All things considered, this study identifies (anisotropic)[7] shear strain as the best metric for plaque damage prediction. The reasons are as follows: first, strain metrics significantly outperformed stresses and energies, except for $S22$ which matched. This tie is broken by strain metrics' exemption from the computational lens problem. Next, the most sensitive metrics were $LE12$, $LE22$, and then $LE12$. Though $LE12$ and $LE22$'s sensitivities were slightly greater than $LE11$'s, the difference was not significant enough to be conclusive. Looking next to the damage-threshold values, though variance did not distinguish the three metrics, magnitude did: the $LE12$-threshold was greatest, making it easiest to identify on imaging. An additional consideration favouring the $LE12$ direction is its association with delamination-based damage, which is additionally better-suited to predicting intra-plaque damage propagation. Should intraplaque damage play a - yet unclear - role in plaque progression or vulnerability, the $LE12$-direction

[7] Identifying 'anisotropic' model variants becomes moot when discussing clinical application of a strain metric, since the computational lens is no longer necessary.

can better predict it than the circumferential/fibre-aligned direction. In addition, $S12$ may be less susceptible to modelling errors than $S11$ or $S22$: The incompressibility assumption, though traditionally accepted, may have influenced $S11$ and $S22$-values to maintain perfect anti-correlation (recall fig. 3.5). As for extension from the modelled two to three dimensions, reports have highlighted the increased role of shear in longitudinal damage-propagation [64], favouring $S12$. Therefore, with sensitivity, clinical application, and accuracy in mind, this study considers $LE12$ the best metric for damage prediction.

Chapter 5

Conclusions

This study compared twelve mechanical metrics' ability to predict damage in atherosclerotic plaques. The study population ($n_{sections} = 49, n_{patients} = 21$) contained $n_{damage} = 167$ damage cases, of which $n_R = 43$ were confirmed ruptures and $n_F = 124$ were fissures[1]. The sections were selected from a previously-reported dataset of carotid artery histology [64]. The selected sections were modelled using section-specific finite element models. The models utilised a state-of-the-art method for acquiring and modelling plaque-specific fibre distributions. Next to the anisotropic models, each section was additionally modelled using a traditional isotropic plaque model - with all other things equal - for comparison. The models were used to compute the twelve mechanical metrics, analysis of which - together with histological observations - led to the following main conclusions.

First, fibre is crucial to plaque mechanics and damage prediction: implementing fibre improved damage sensitivity by 20% or more. Furthermore, fibre-models revealed novel mechanical phenomena in the plaque: fibre-shielding, damage propagation through fibre-channels, metric-elevating fibre-vortices, and deep intra-plaque hotspots. Second, regarding damage-sensitivity of different metric-types: strain metrics were generally more sensitive than stress metrics, both of which were vastly superior to energy metrics. Third, regarding metric-directionality, the shear and transverse/fibre-perpendicular (12 and 22) directions were most sensitive to damage, closely followed (and sometimes matched) by the circumferential/fibre-parallel direction (11). Fourth, this suggested - and histological inspection confirmed - that both delamination and tearing damage-modes exist within plaques, often in tandem (mixed-mode). Tearing-only damage was only observed in caps, while mixed-mode was observed in caps and at inclusions, while delamination-only damage was observed in caps, at inclusions, and as the only damage-mode for intraplaque fissures. Thus, delamination is the primary damage-mode in plaque, but tearing remains critically important to the etiology of ruptures.

Ultimately, this study concludes that the best metric for predicting atherosclerotic plaque damage is shear strain. Not only did it achieve the best rupture sensitivity (98%) and second-best fissure sensitivity (85%, trailing $LE11$ by 2%), but it also circumvents the computational-lens problem hindering clinical application of stress metrics[2], making it a promising candidate for damage prediction in the clinical setting.

[1] *Ruptures* referred to damage-sites with blood (erythrocytes) present, while *fissures* referred to damage-sites without.

[2] The 'computational lens' refers to the necessary (and potentially inaccurate) additional steps of modelling and computation required to evaluate stress metrics.

Chapter 6

Future Work

Avenues for future work are presented here in order of increasing separation from the current method: first, improvements on the current method; second, extensions thereof; third, new studies inspired by the current findings. Lastly, a road-map towards damage prediction in the clinic is presented.

The current method lends itself to three salient improvements: interpolation of the fibre-parameters, smoothing also, and a quantitative (global) maxima analysis. Interpolation of fibre parameters in plaque-gaps (damage) instead of the current isotropic material fill-in would bring the models closer to reality. Furthermore, it might allow relaxation of the 'large tissue-gap' exclusion criterion without loss of accuracy, facilitating the inclusion of more cases. Second, smoothing fibre-parameters across elements could ameliorate the 'peakiness' of the anisotropic results caused by discretisation across elements. However, special care would have to be taken not to smooth across true fibre-boundaries; a simple smoothing filter would not suffice. Third, a quantitative maxima analysis answering two questions: how often were peak metric-values also global maxima; and within what neighbourhood size were they local maxima (with 95% confidence). The answers to these questions would better facilitate clinical applications of the current findings.

Three extensions of the current method could be: adding the third dimension, additional image-processing, and further (quantitative) analysis of the fibre-data. First, adding the third dimension would significantly improve the current study, given reports of axial damage propagation ([64]) and significant mechanical differences in 3D vs. 2D models ([57]). However, the current image-processing method's reliance on histological source material (which is fundamentally 2D) would complicate the transition. A solution could be to 'stack' adjacent sections and use interpolation to fill in the gaps. The current dataset could even be used, since it was serially-sectioned. Alternatively, there are 3D imaging modalities capable of extracting fibre data: OCT [65] or diffusion tensor magnetic resonance imaging (DT-MRI) [66, 67]. The current MATLAB-method could feasibly be adapted to use 3D-source data. Second, additional image-processing modules could be added to the current MATLAB-method. For example, the current study included a colour-analysis pilot (unreported) aimed at discerning fibre-quality by analysing dye-colour saturation. Although the current H&E staining was sufficient for a proof-of-concept, a proper study would call for a collagen-stained dataset[1]. Lastly, the fibre-data obtained in this study deserves further (quantitative) analysis. Although Douglas [51] performed such a study - reporting the vulnerable 'vortices' ('triangles' in [51]) and damage-channels (as observed in [64]) also observed in the current study - their dataset did not include confirmed rupture cases. Therefore, a similar study of the current data set with especial focus on dispersion-related cap-vulnerability would be of significant added value. Furthermore, computational testing of the observed 'fibre-effects' (e.g: dispersion-related vulnerability, damage-propagation through fibre-channels, and fibre-shielding) in idealised models could solidify our

[1] The current dataset included a small number of Mallory's Trichrome stained sections; it could be used as a starting point for a small-sample study.

understanding of these phenomena.

Observations made during the current study encourage further study into the following topics: First, the relationship between inflammation and fibre-dispersion. Histological analysis during this study revealed that intraplaque inflammation (identified here by observation of eosinophils) was invariably accompanied by increased dispersion values. Demonstrating the causal link (proposed in [48]) using more reliable inflammation-markers and/or observing progression would explain how inflammation affects plaque-vulnerability from the *mechanical* perspective. Second, this study observed damage initiation at inclusions (e.g. fig. D.6, as observed in [64]). Moreover, the computational modelling performed in this study achieved high sensitivities for damage-sites initiated at inclusions; supporting damage in vivo rather than during handling. Future studies should strive to either observe (via imaging) or reproduce (via inflation testing) this phenomenon, so that it can be assimilated (if correct) into our understanding of atherosclerotic progression. Third, observations of calcifications in the current dataset reiterated their diversity and our current lack of understanding into their potentially-variable material properties ([85]) and effects on plaque mechanics [85]. Fourth, observations of damage modes and propagation paths in the current study inspire attempts to model these phenomena using fracture mechanical methods (XFEM, see [90, 91, 92, 93, 94, 95]). In anticipation of this, the current study published indicative strength values which may be used as damage initiation criteria for this purpose. Although strength values obtained through mechanical testing would be preferable, reports are scarce (especially for metrics other than tensile stress) at the time of writing [96].

Finally, by demonstrating high damage-sensitivity (and locational accuracy) using strain metrics, this study indicated a way around the 'computational-lens' problem, bringing us closer to plaque-damage prediction in the clinic. Since strain-values can be directly extracted from readily-available imaging modalities (e.g. ultrasound), a low-cost software overlay capable of highlighting vulnerable plaque-regions in real-time is feasible. It could work by highlighting plaque-regions where strain exceeds pre-programmed strain-based damage-threshold values. Hence, additional study (mechanical testing) aimed at ascertaining strain-based damage-criteria is crucial. However, it should be noted that threshold-values could vary with plaque-quality and morphology (e.g. inflammation/fibre-dispersion due to vortices). Thus, a classification of strain-based damage-thresholds for different plaque-scenarios might be necessary. This could be accounted for in the software by providing multiple overlays (with different threshold-values for different scenarios). Selection of the appropriate overlay could be guided by virtual histology (VH-IVUS), hybridisation with NIRS, or a trained clinician. Alternatively, material identification might be automated using the inverse elastography method outlined in ([97]). Altogether, after this study, mechanical testing and/or feasible software development might be all that separate us from accessible and improved plaque-damage prediction in a clinical setting.

Appendix A

Fibre Data for Example Case

A.1 Histological Source Image

Figure A.1: Example Case 99-105_21000 Histology

A.2 Fibre Plot

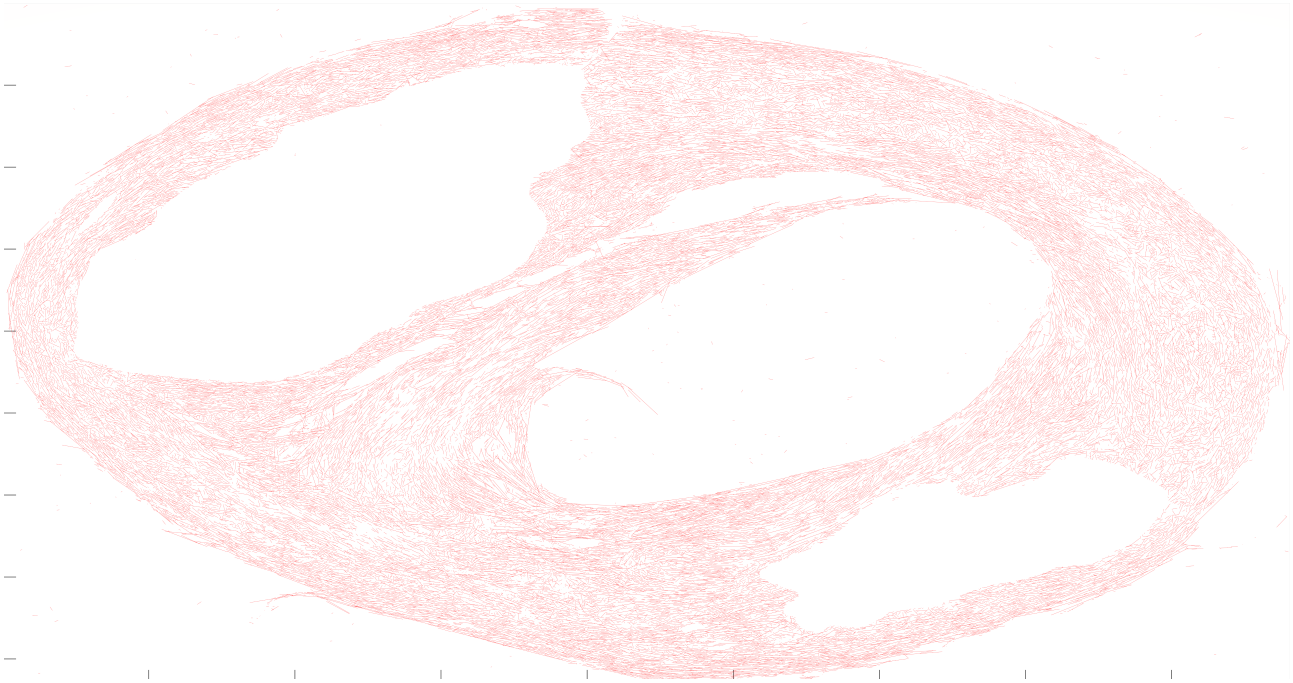

Figure A.2: Fibre Plot for Example Case 99-105_21000

A.3 Dispersion Map

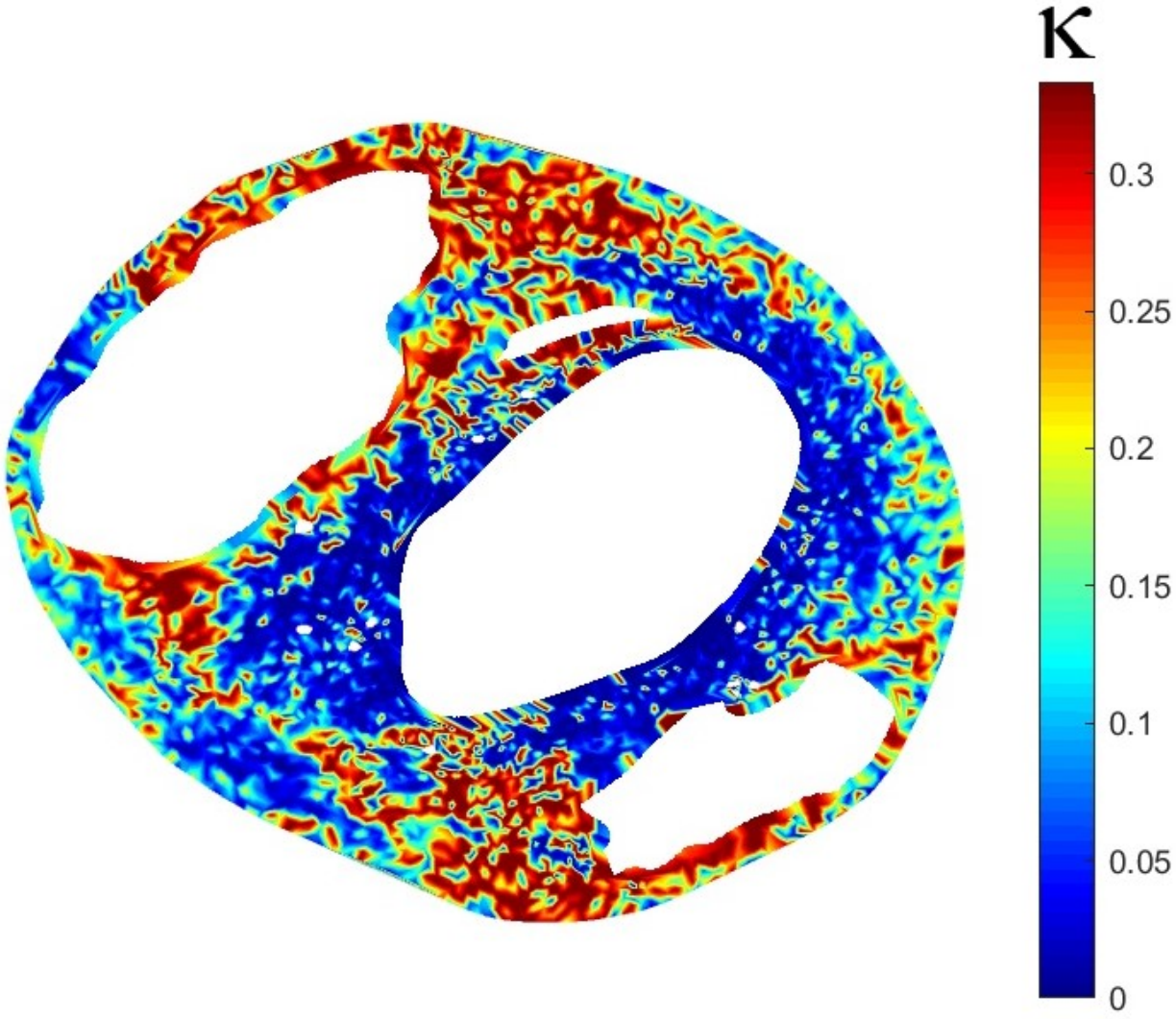

Figure A.3: Dispersion Map for Example Case 99-105_21000

Appendix B

Metric Output Fields for Example Case

B.1 Isotropic Models

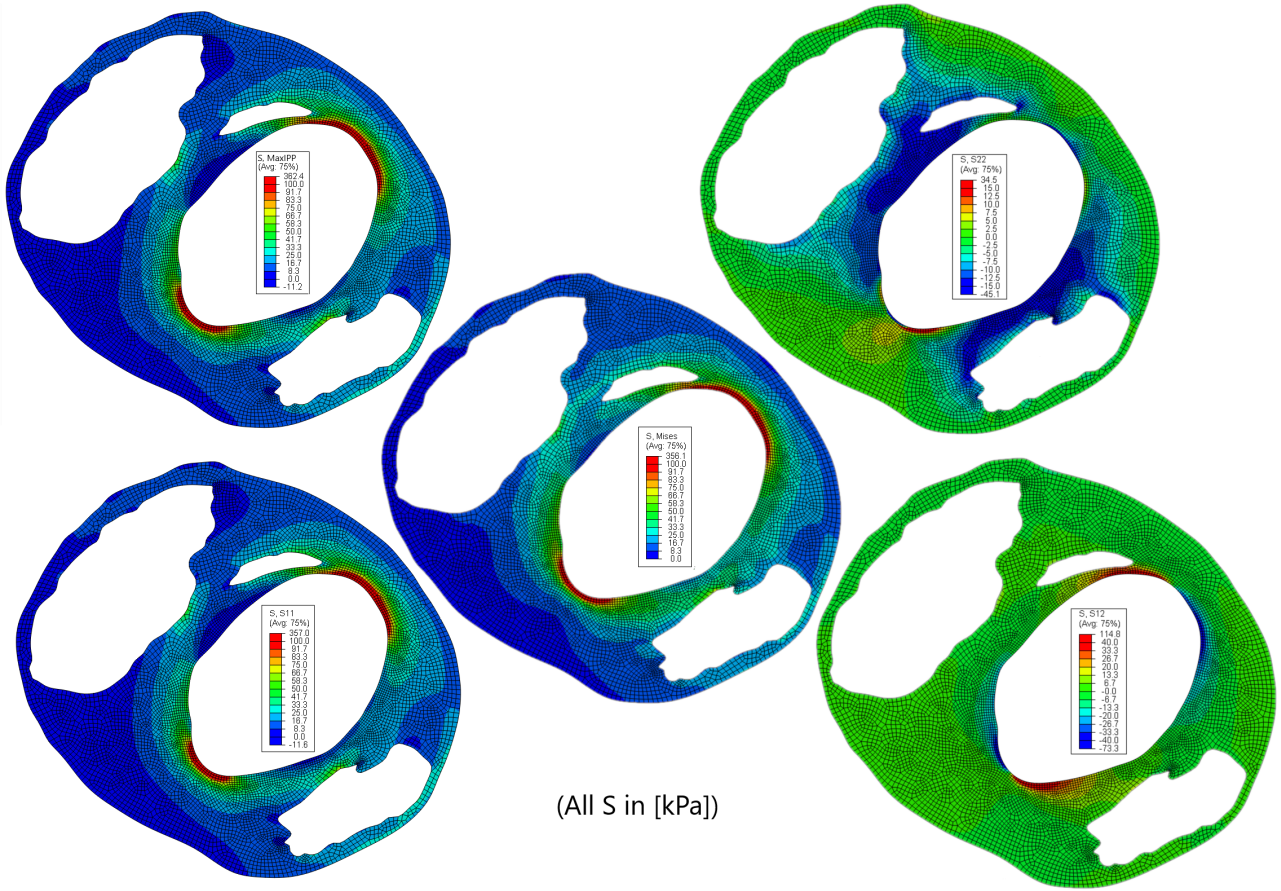

Figure B.1: Stress Metric Output Fields for the Isotropic Example Case (99-105_21000)

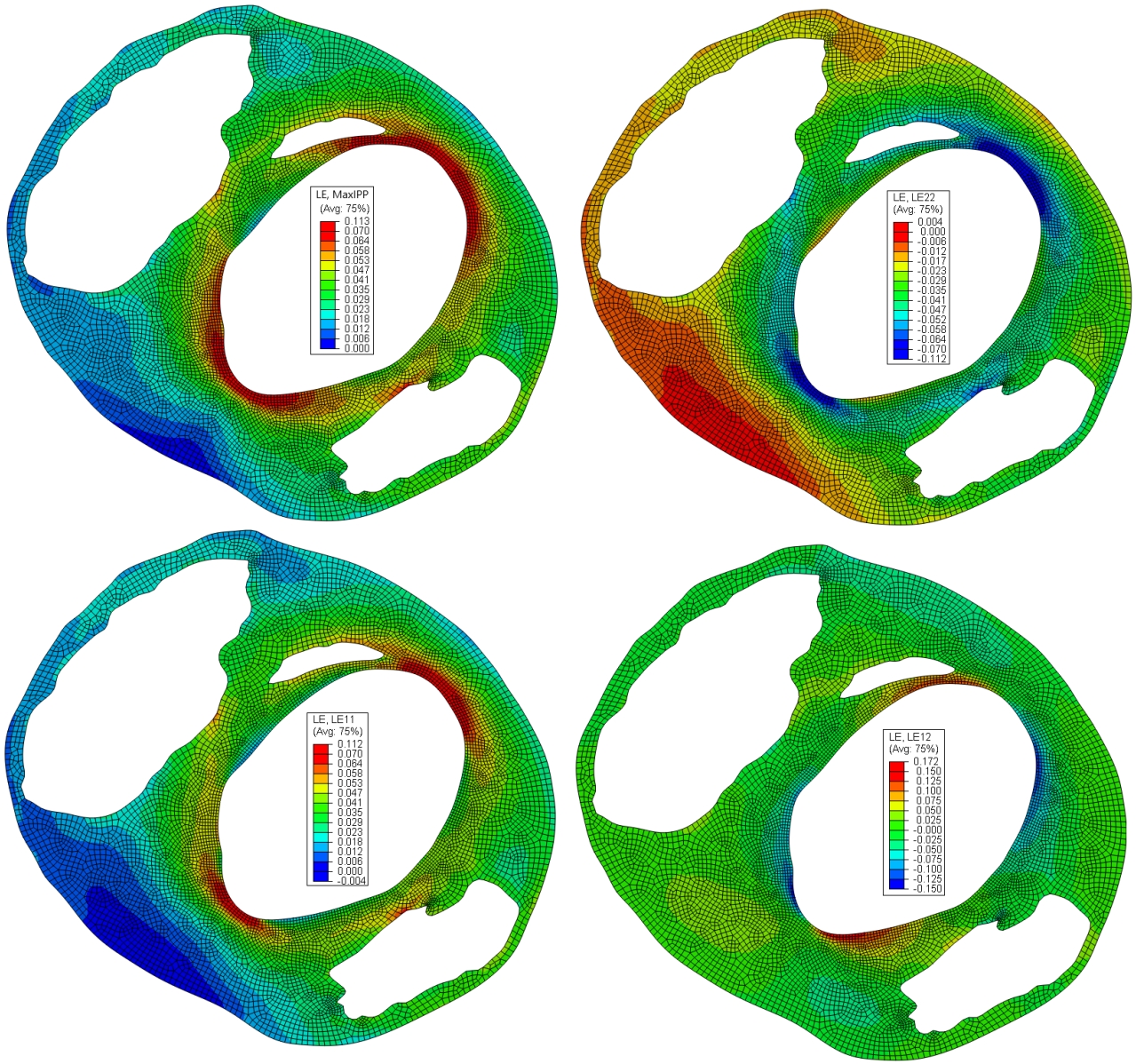

Figure B.2: Strain Metrics for the Isotropic Example Case (99-105_21000)

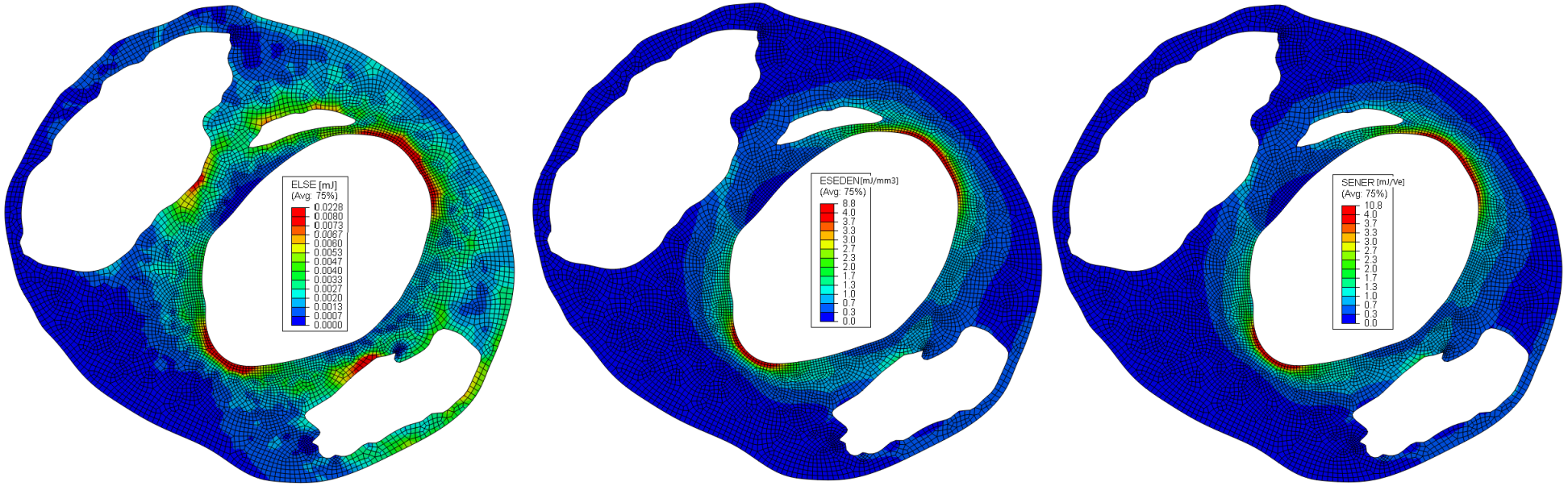

Figure B.3: Energy Metric Output Fields for the Isotropic Example Case (99-105_21000)V_e denotes current element volume

B.2 Anisotropic Models

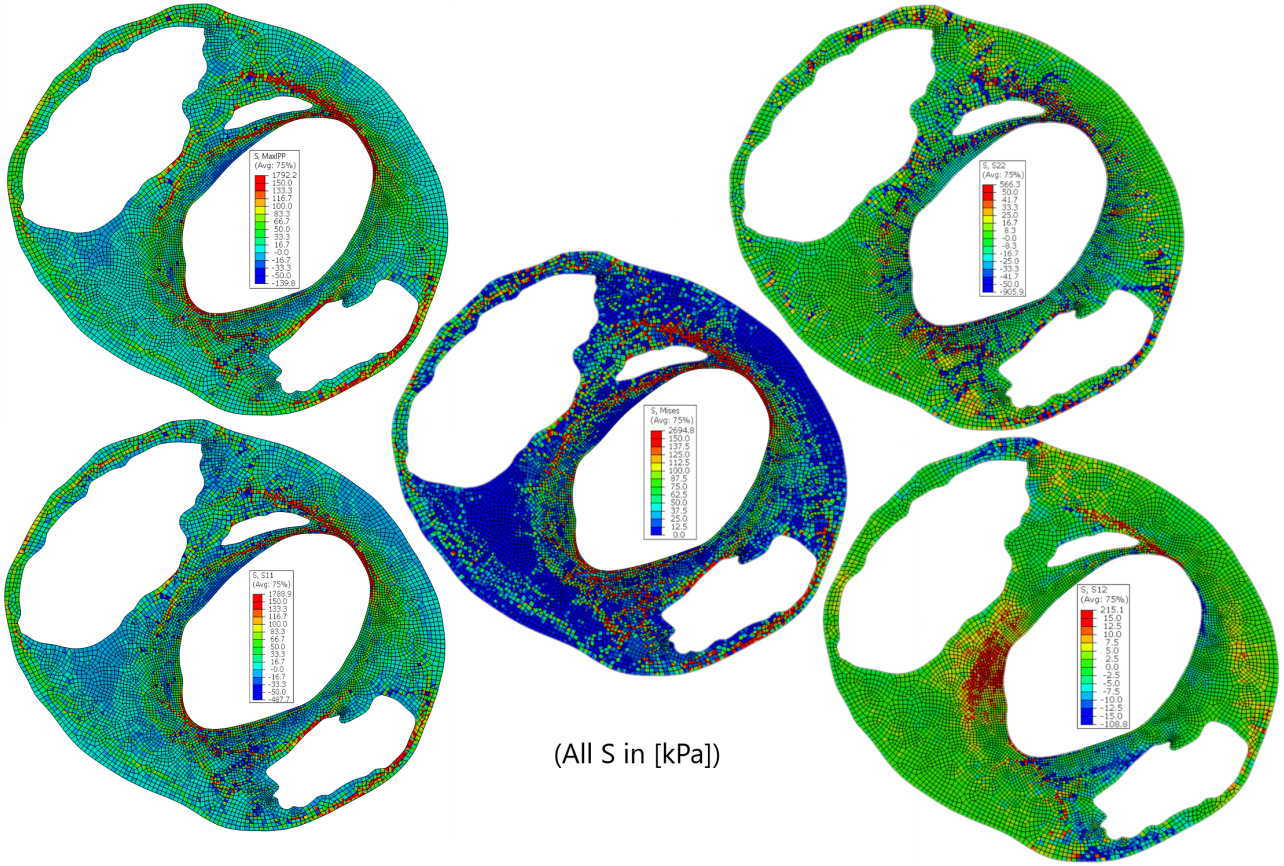

Figure B.4: Stress Metric Output Fields for the Anisotropic Example Case (99-105_21000)

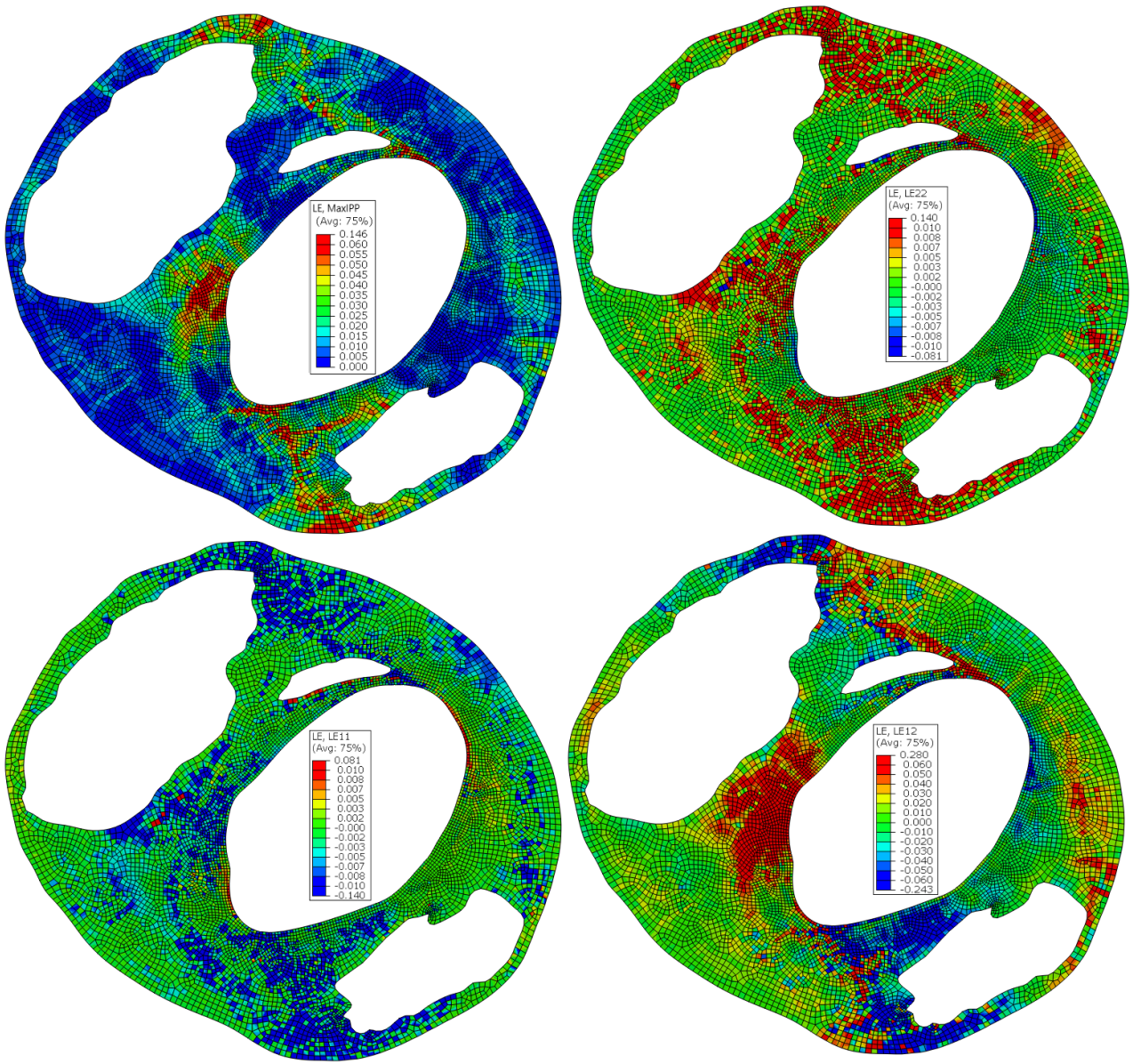

Figure B.5: Strain Metrics for the Anisotropic Example Case (99-105_21000)

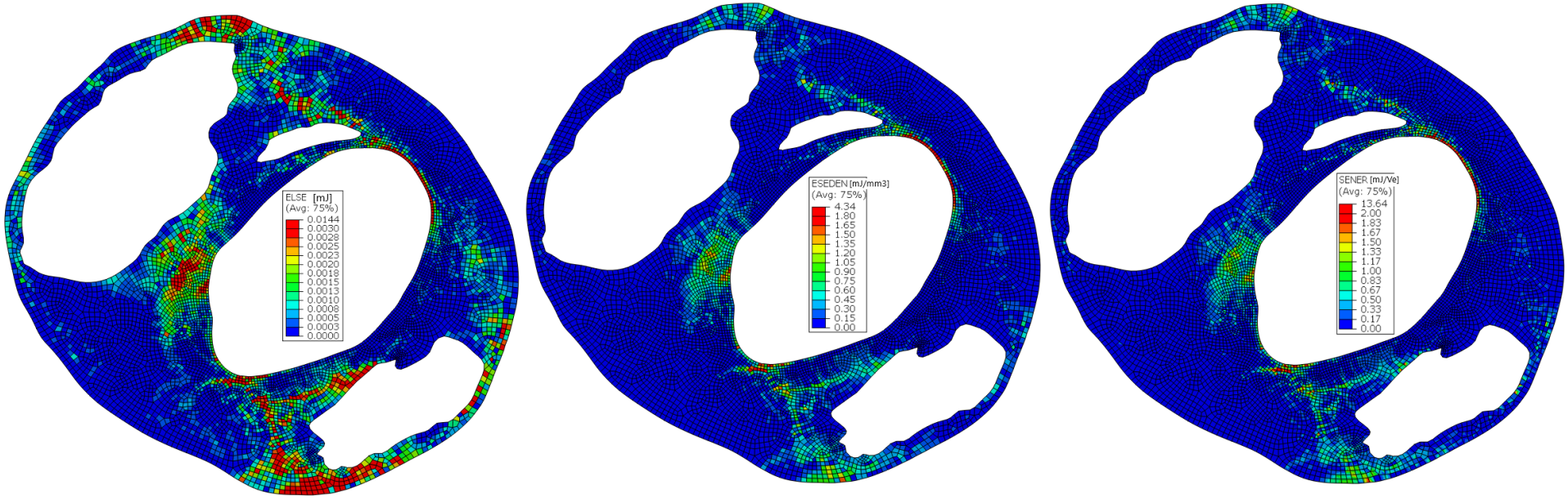

Figure B.6: Energy Metric Output Fields for the Anisotropic Example Case (99-105_21000)V_e denotes current element volume

Appendix C

Path Data for Example Case

C.1 Isotropic Path Data

C.1.1 Lumen

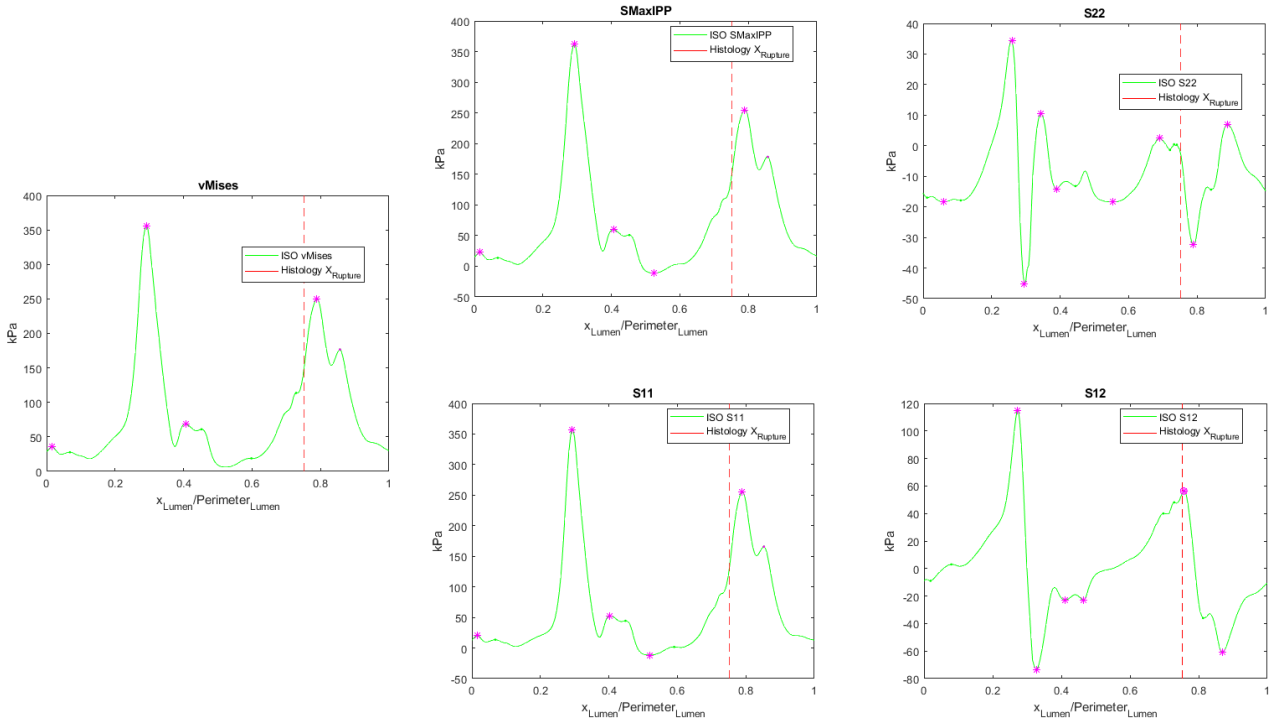

Figure C.1: Lumen-Path Isotropic Stress Metrics

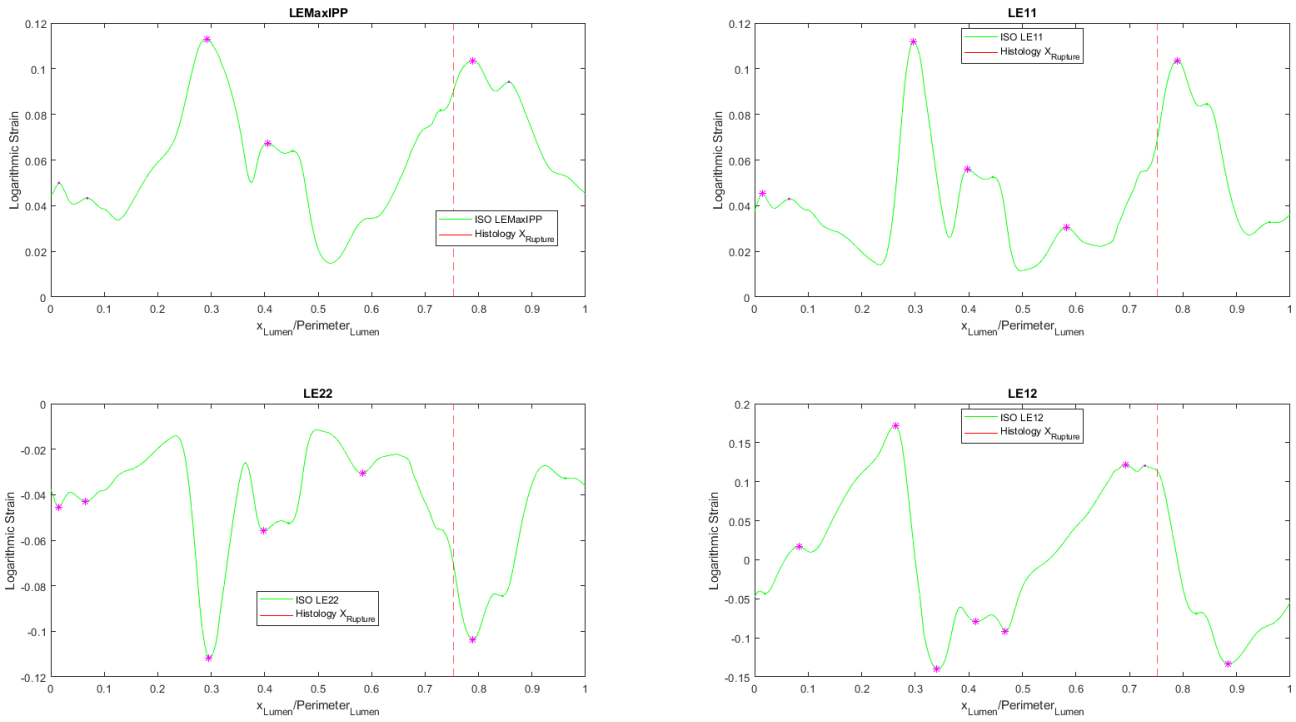

Figure C.2: Lumen-Path Isotropic Strain Metrics

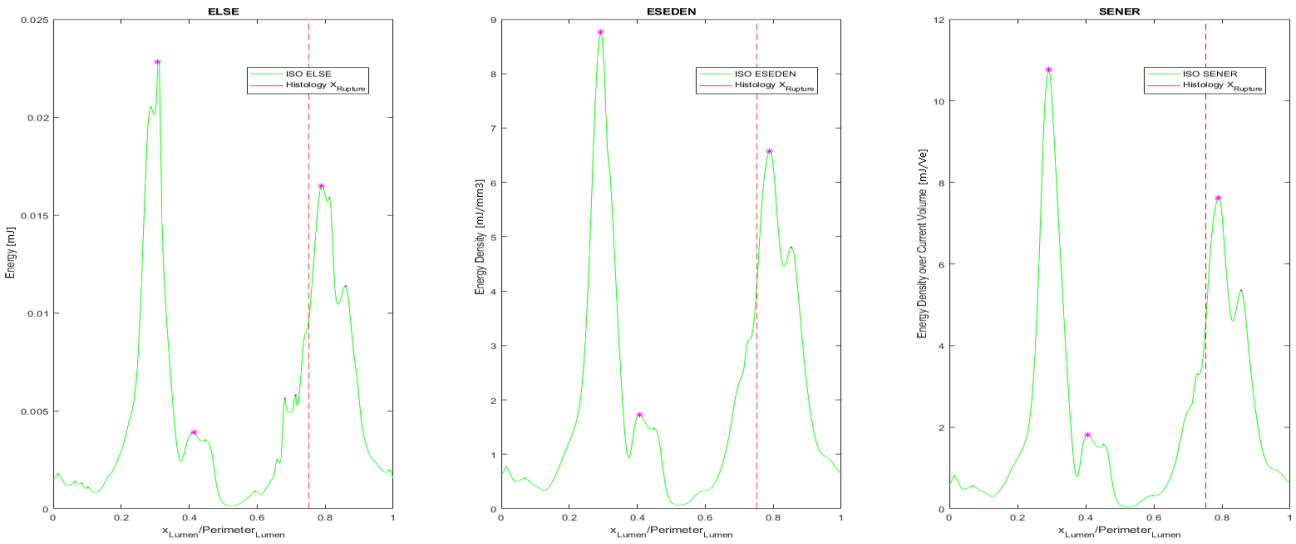

Figure C.3: Lumen-Path Isotropic Strain Metrics

C.1.2 NC1

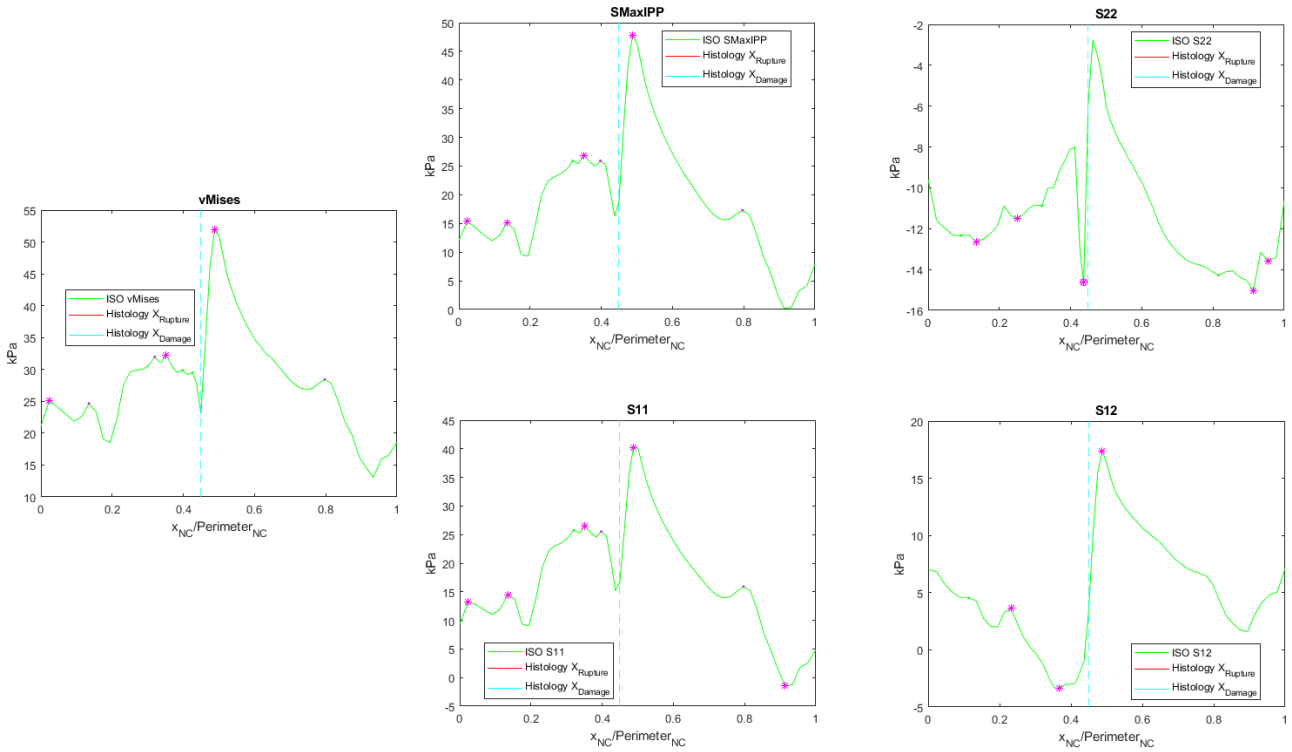

Figure C.4: NC1-Path Isotropic Stress Metrics

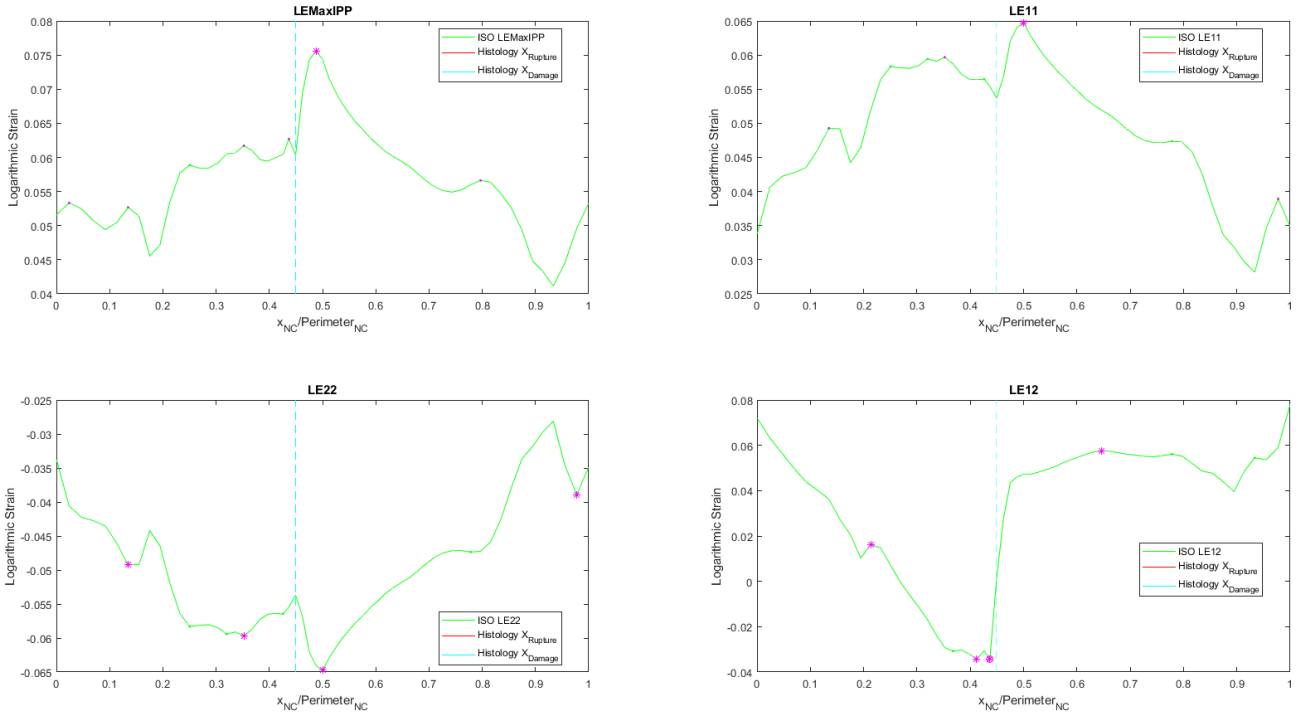

Figure C.5: NC1-Path Isotropic Strain Metrics

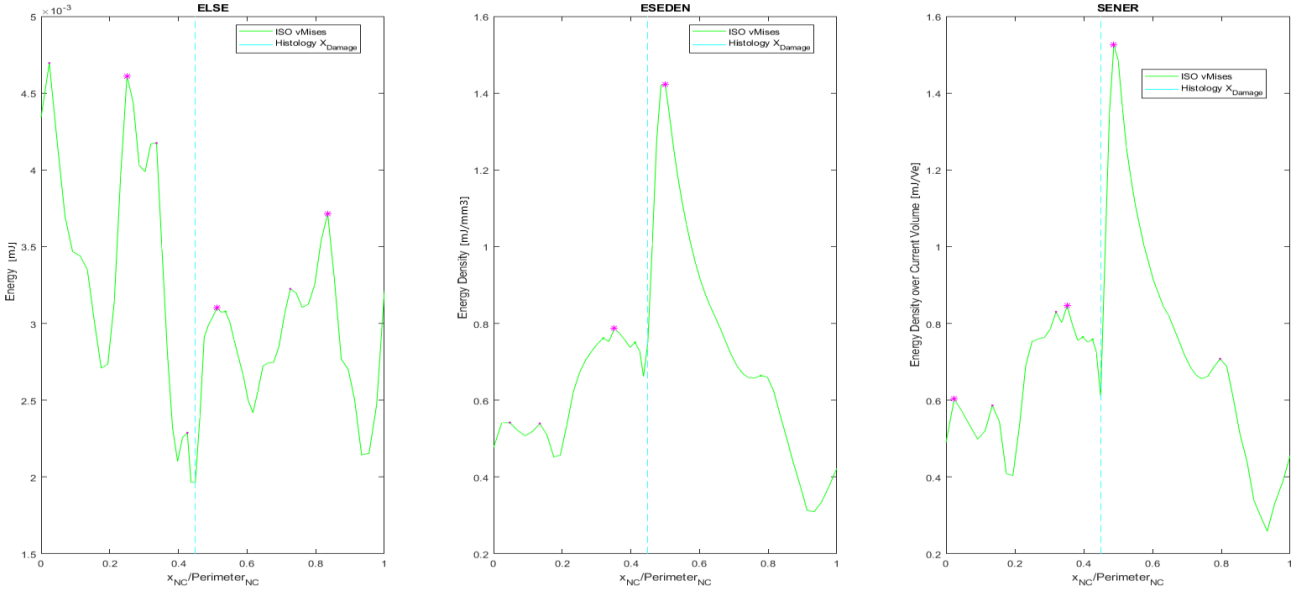

Figure C.6: NC1-Path Isotropic Energy Metrics

C.2 Anisotropic Path Data

C.2.1 Lumen

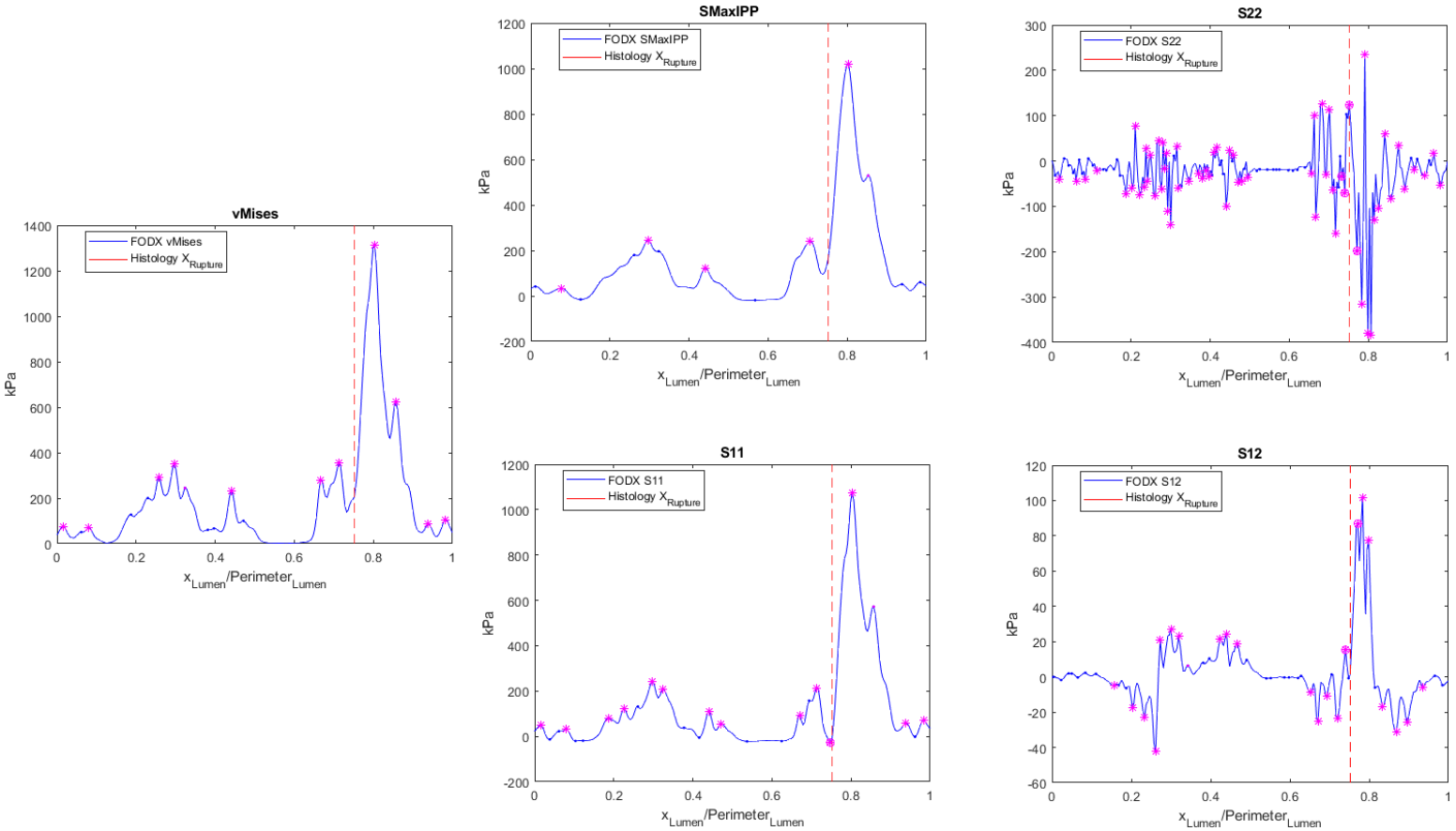

Figure C.7: Lumen-Path Anisotropic Stress Metrics

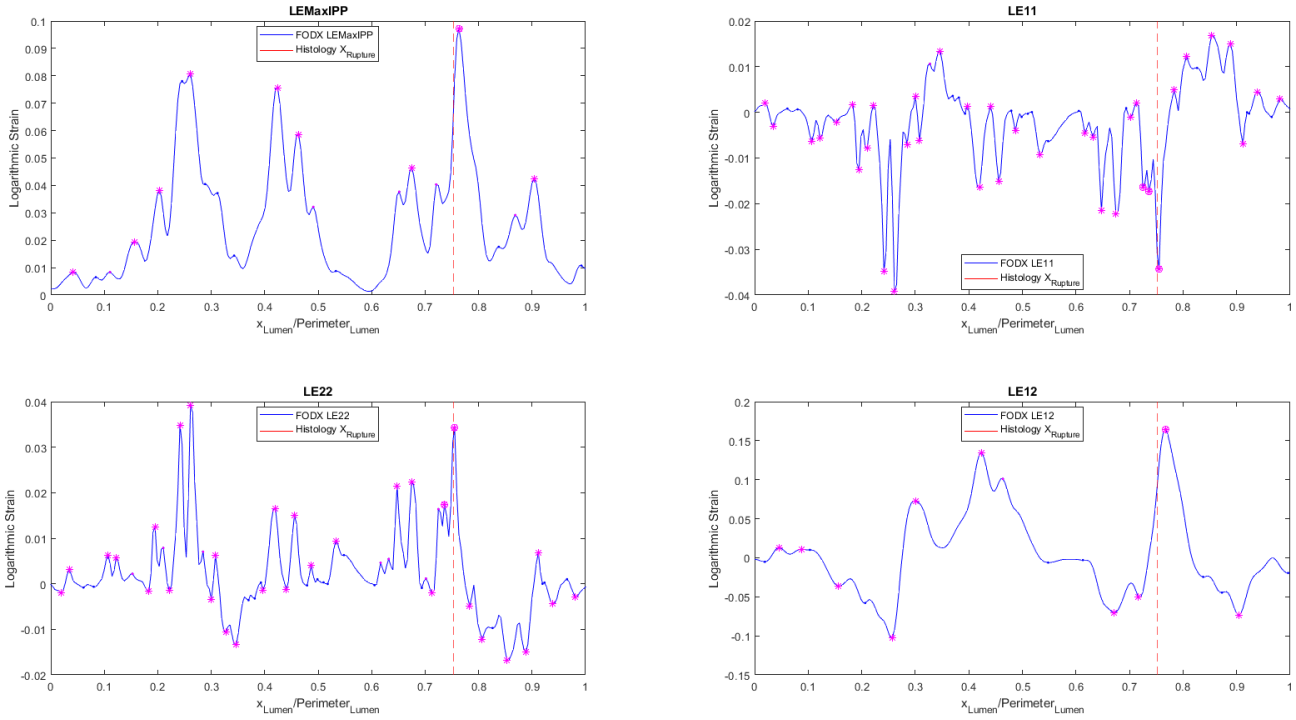

Figure C.8: Lumen-Path Anisotropic Strain Metrics

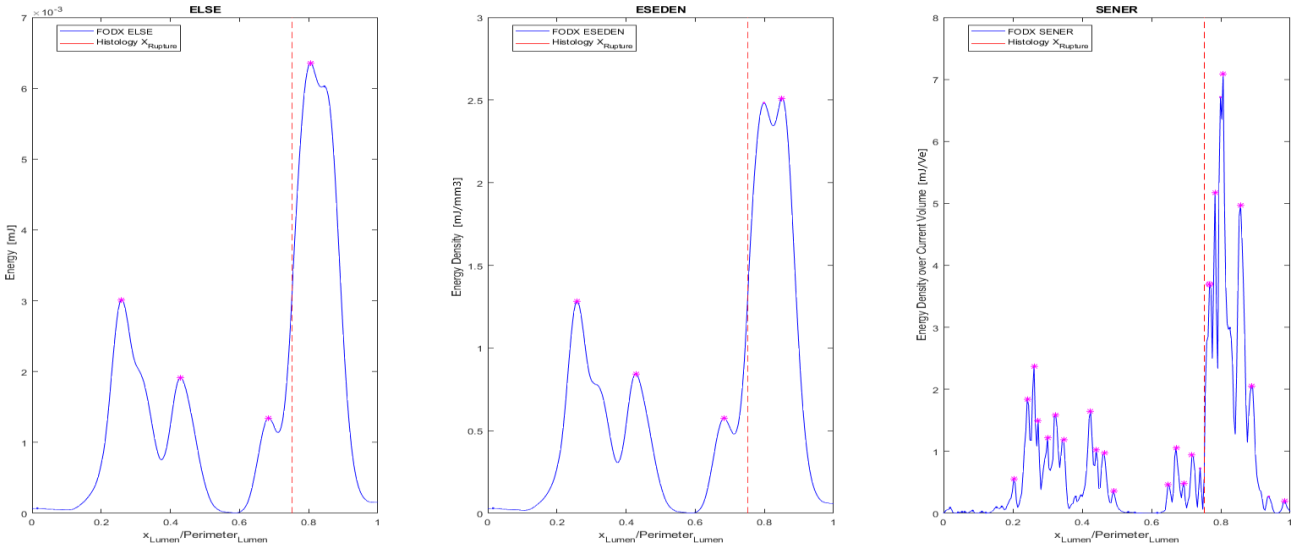

Figure C.9: Lumen-Path Anisotropic Energy Metrics

C.2.2 NC1

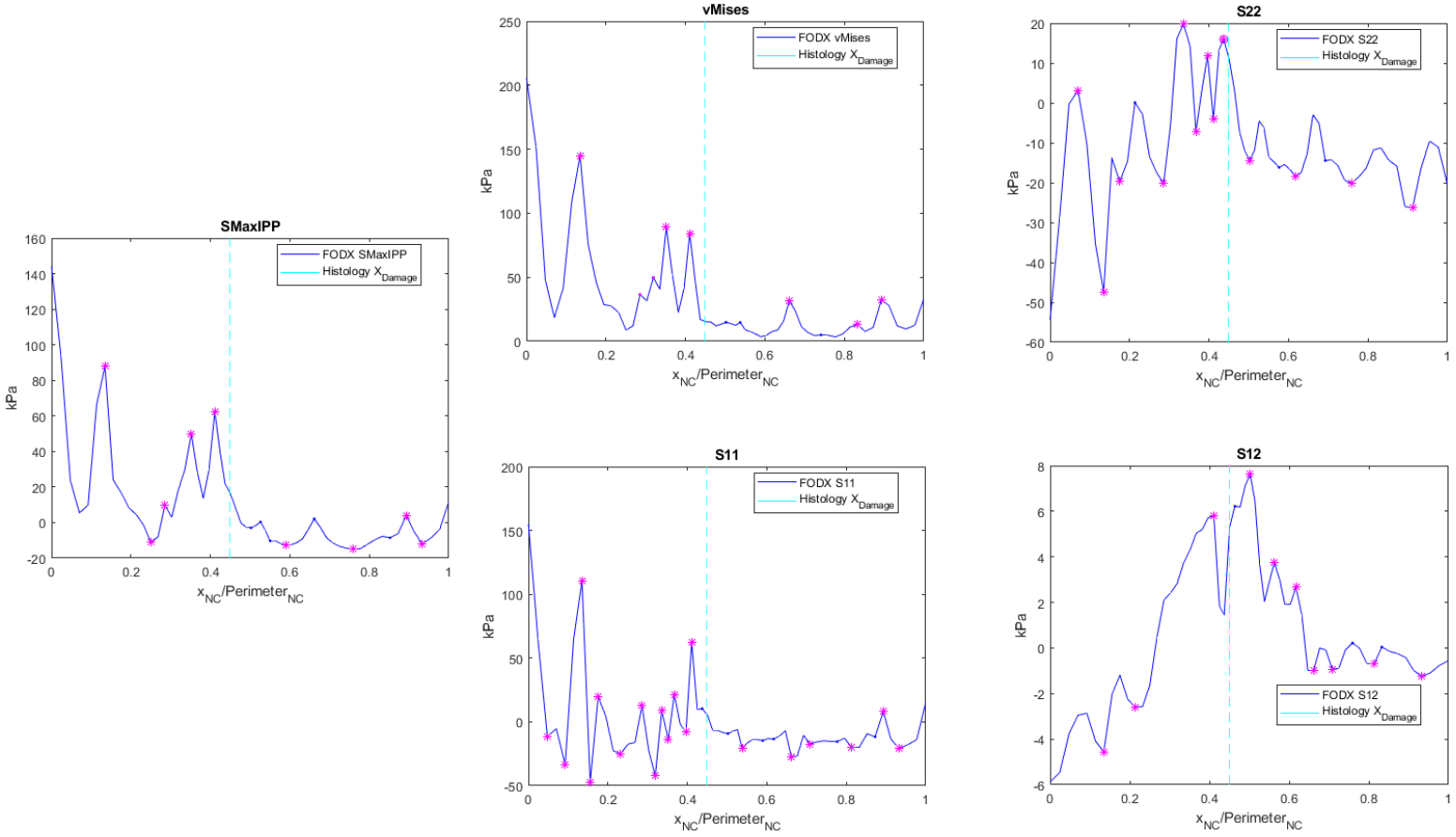

Figure C.10: NC1-Path Anisotropic Stress Metrics

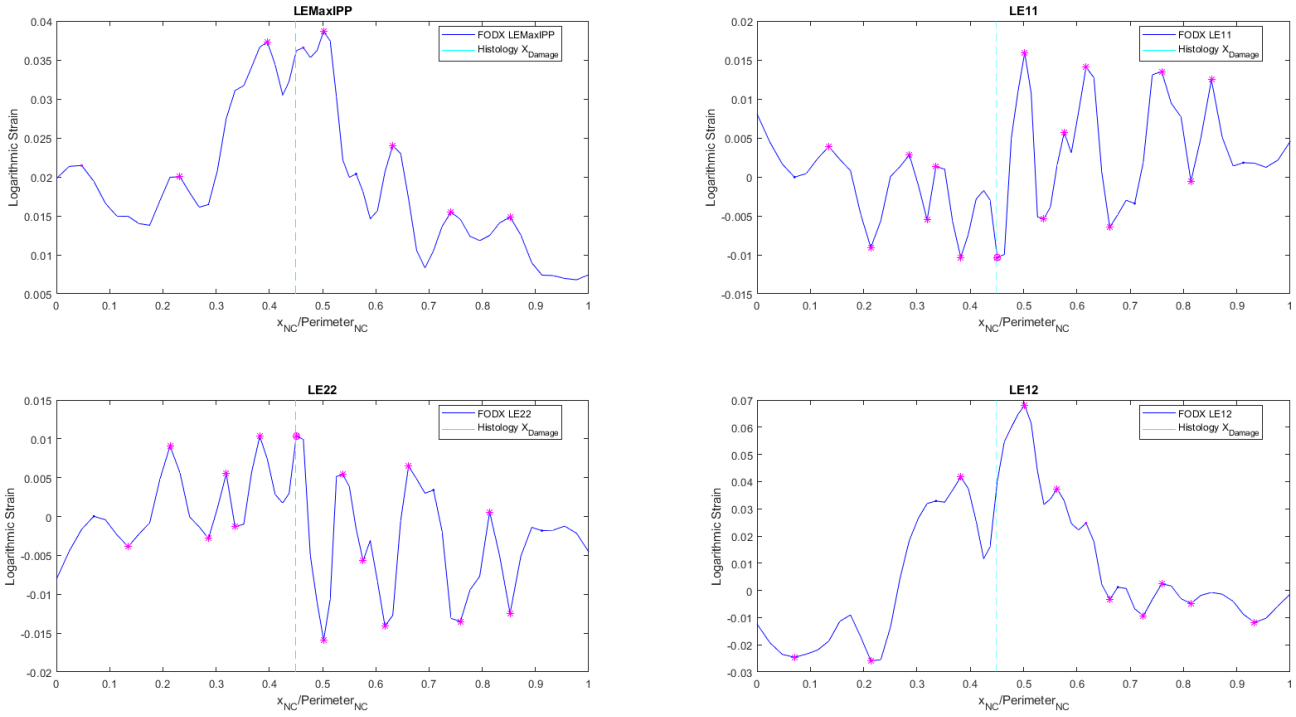

Figure C.11: NC1-Path Anisotropic Strain Metrics

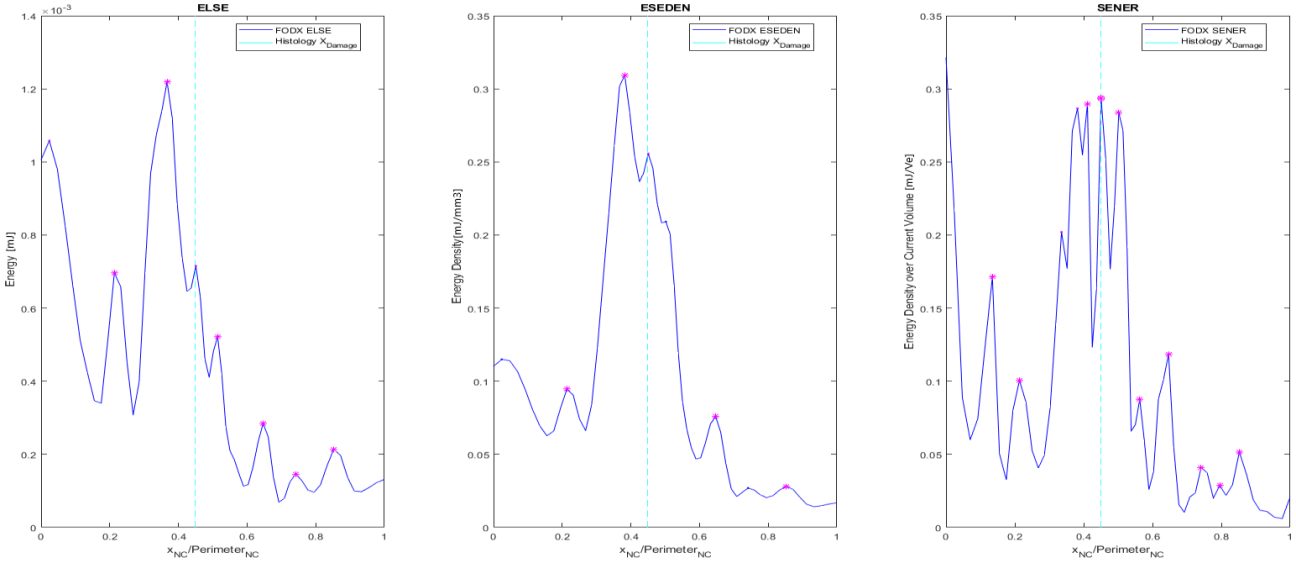

Figure C.12: NC1-Path Anisotropic Energy Metrics

Appendix D

Histology Observations (Examples)

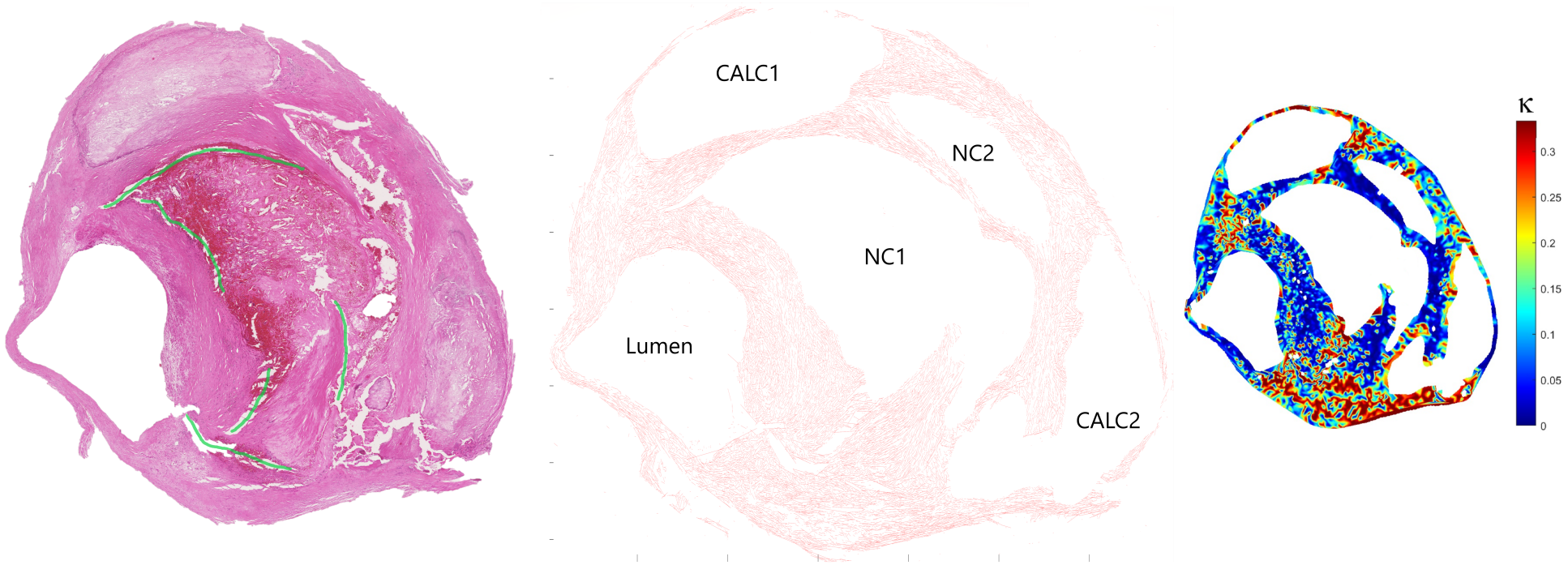

Figure D.1: Inclusion-Encirclement and corresponding Damage-Channels (green annotations) in section h00-16_17000
Left: Source Histology with Damage-Channels Annotated in Green
Middle: Fibre Plot - N.B: fibre running along inclusion boundaries (NC1/2, CALC1 in particular)
Right: Dispersion Map - N.B: low dispersion encircling lumen/inclusions, increased dispersion at vortices (e.g. North of Lumen and NC1)

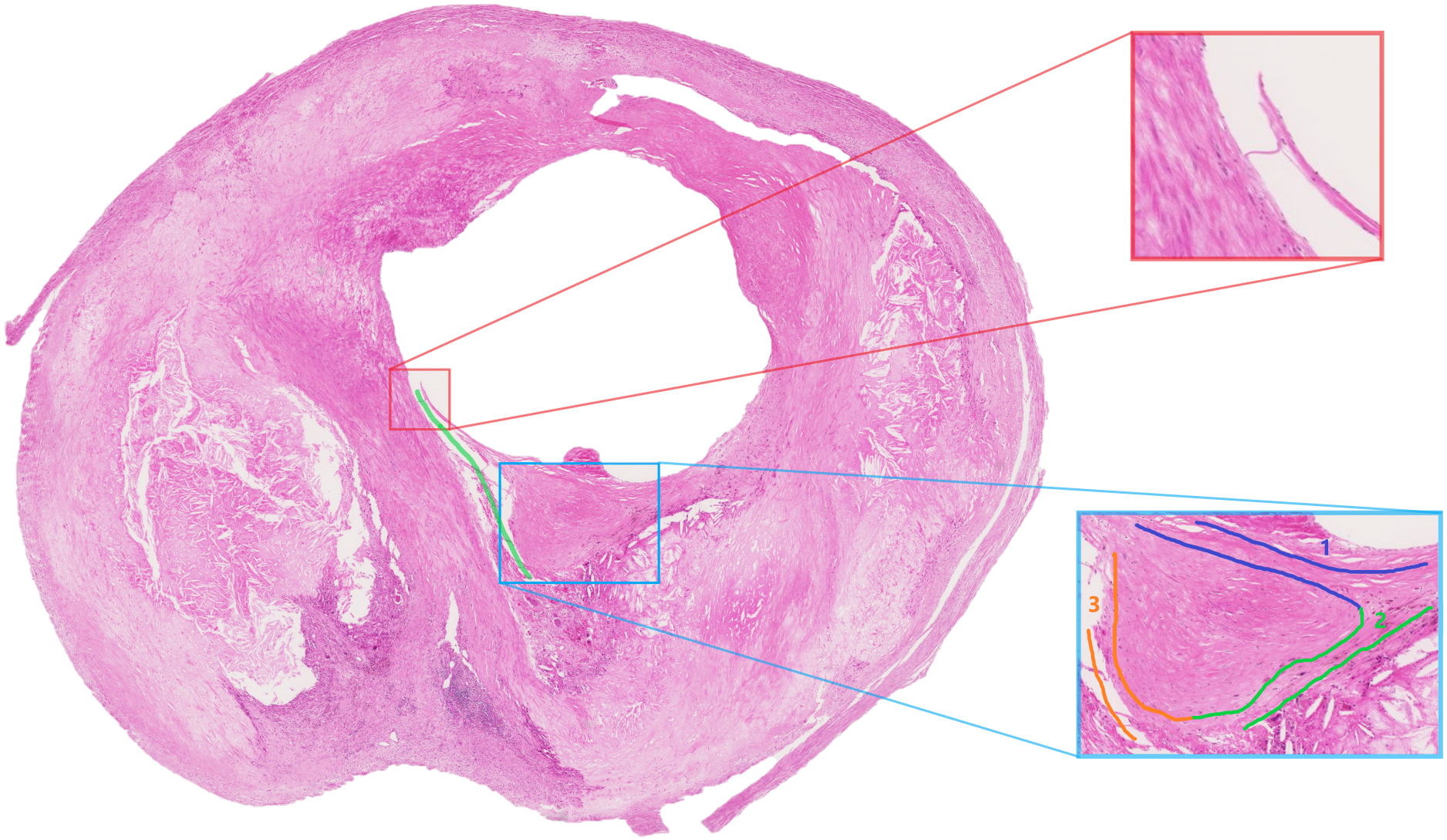

Figure D.2: Delamination Damage-Mode at Rupture-site (red inlay*) and Vortex Fibre Region (blue inlay**) in section h01-31_17000
* N.B: This rupture consists of a luminal fibre-tear followed by delaminative damage-propagation along a fibre-channel. A delaminating fibre can be seen spanning the damage-gap.
** A large vortical-fibre region arises where three fibre-groups convene: a lumen-following group (1) and two opposed inclusion-following groups (2 and 3). See fig. D.3 for corresponding fibre plot and dispersion map.

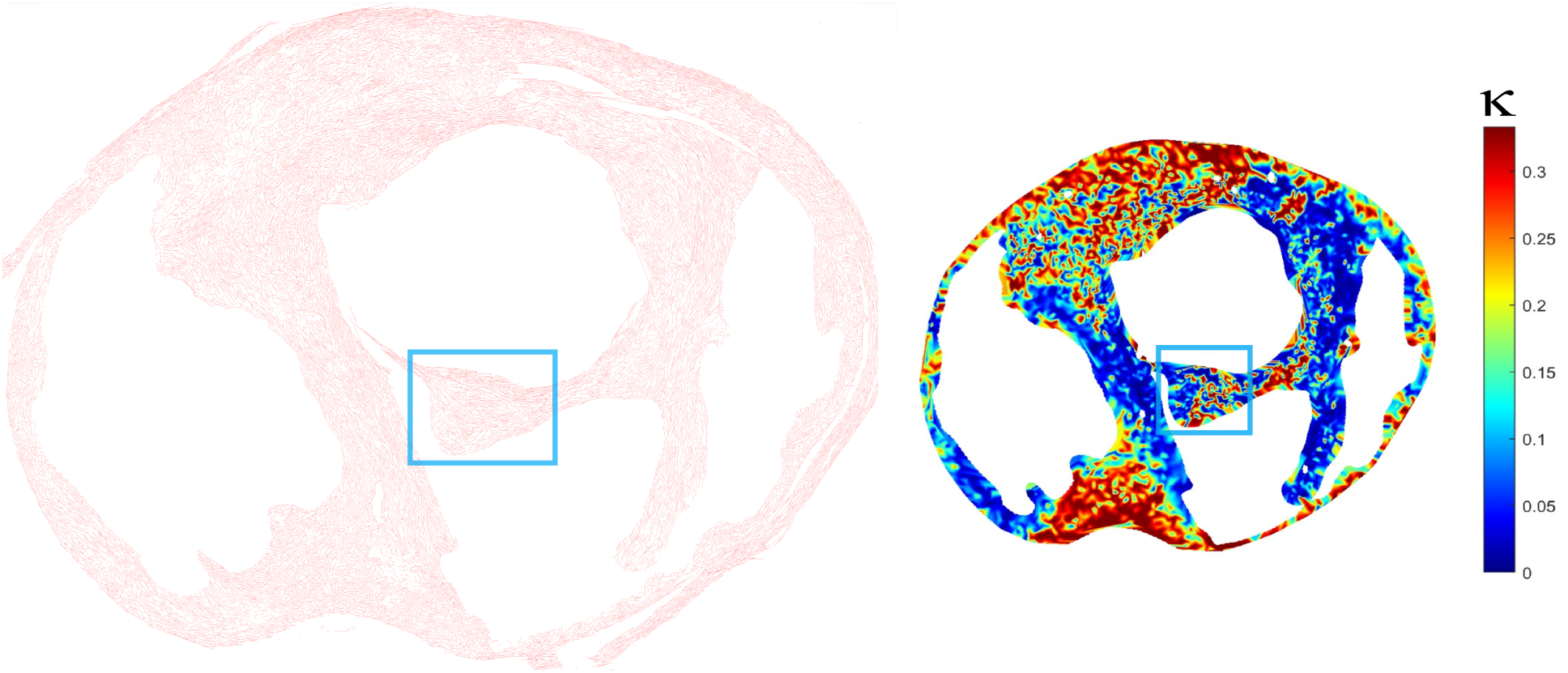

Figure D.3: Vortex Region (blue inlay) in Fibre Plot (left) and Dispersion Map (right) of section h01-31_17000
N.B: High Dispersion (of fibres) in the vortex region (blue inlay)

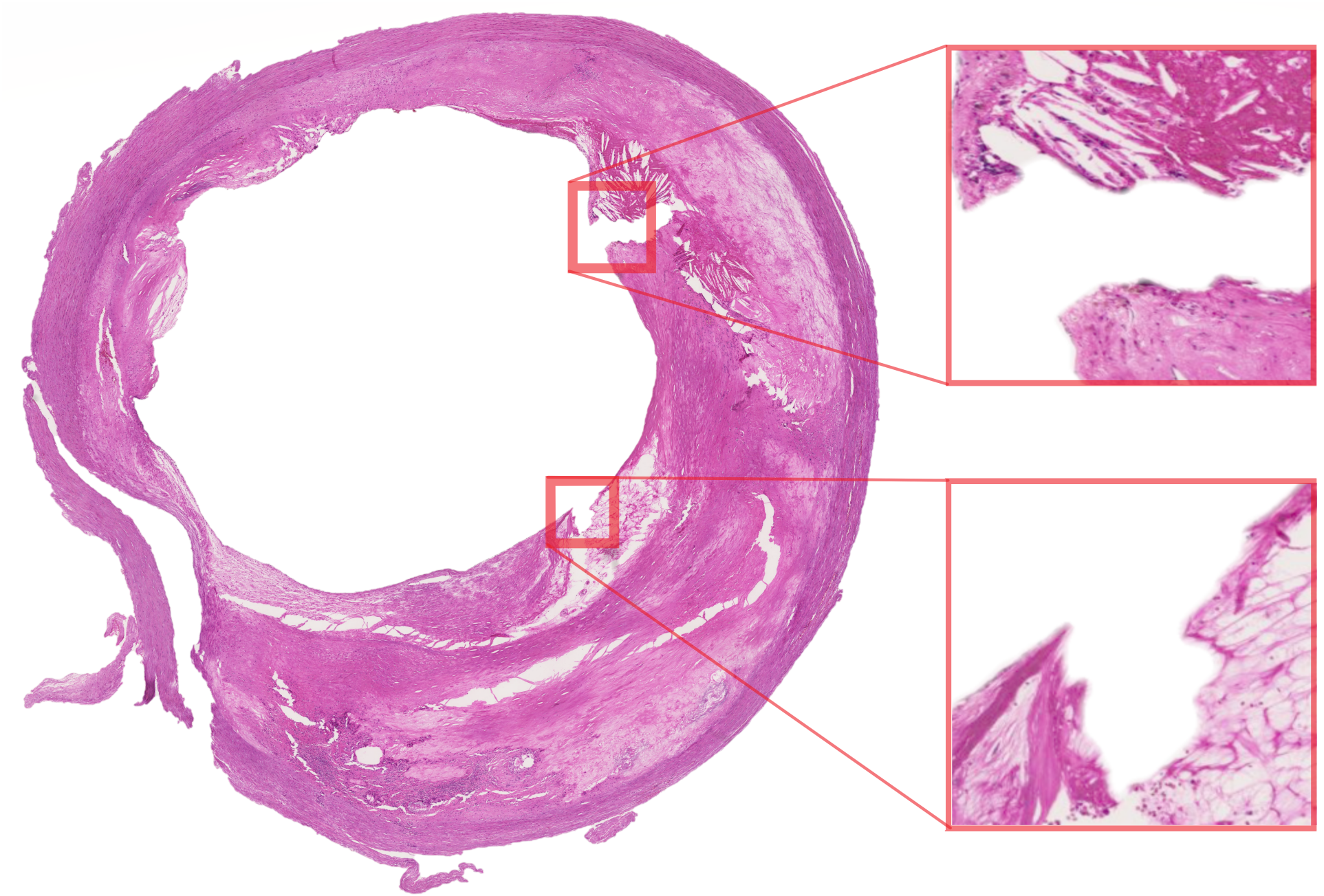

Figure D.4: Tearing Damage-Mode at Cap-Ruptures (red inlays) in section h03-75_9000

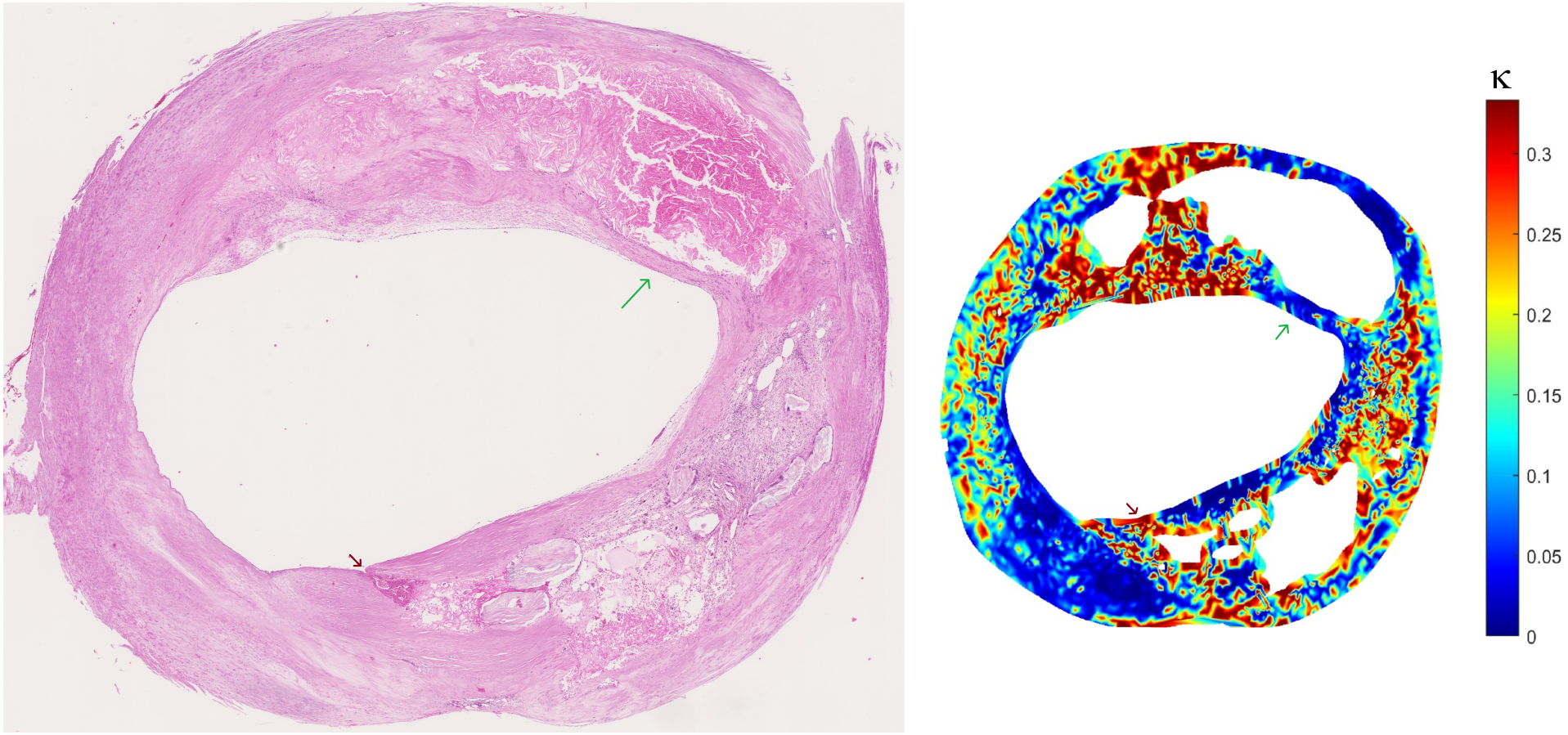

Figure D.5: Stable Thin Cap (green arrows) histology (left) and corresponding Dispersion Map (right) for section h02-57_11000
Green Arrows: Stable Thin Cap. Note aligned fibre in the histology at left and corresponding low dispersion at right.
Dark Red Arrows: Healed Rupture. Note the higher dispersion values at right.

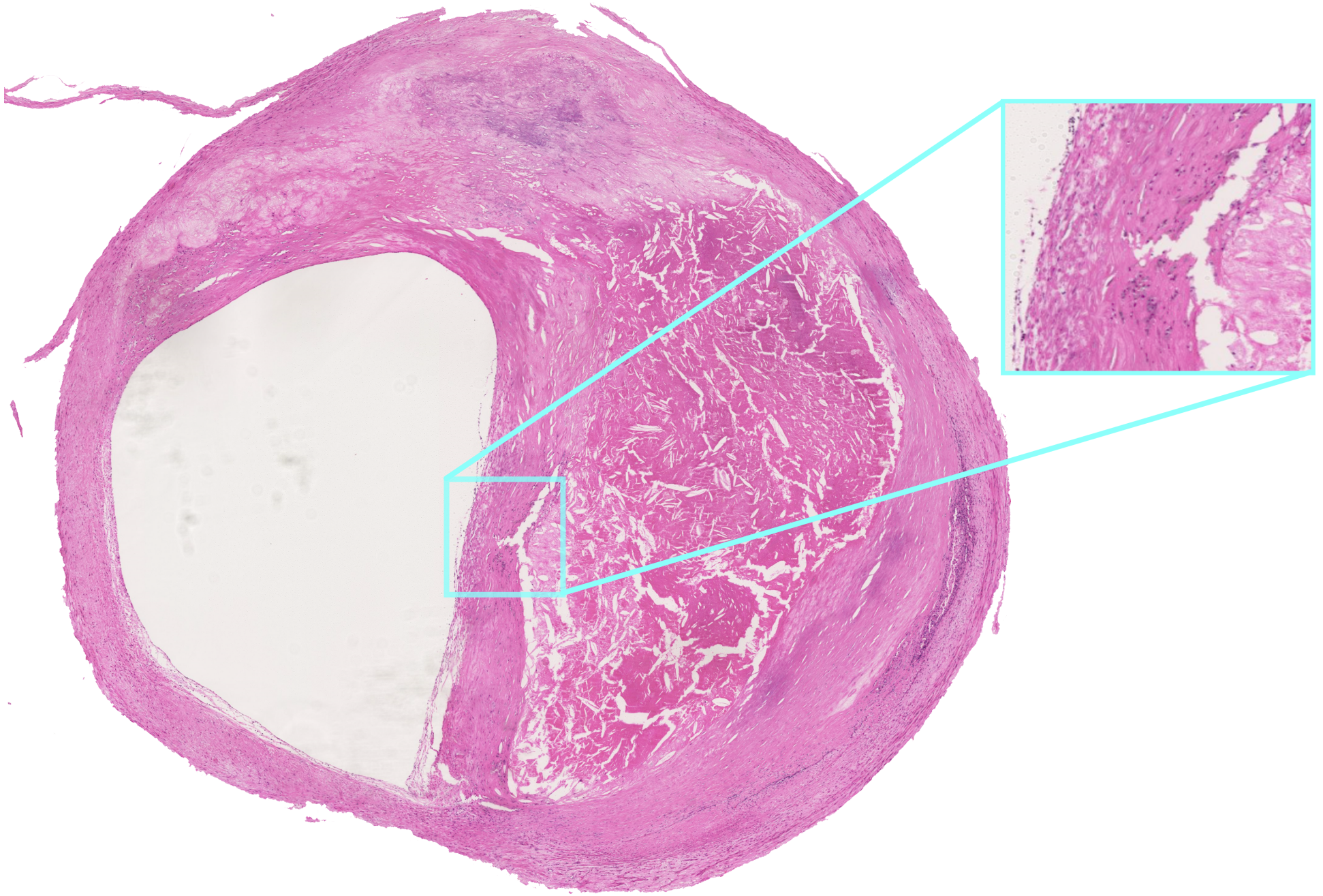

Figure D.6: Damage Initiated at an Inclusion in section h03-69_11000

N.B: Damage propagation towards the Lumen is *tearing* through the cap, whereas delamination is visible around the inclusion. It is unclear whether the damage was initiated mid-cap or at the inclusion. This cap did not rupture because of quality fibre at the Lumen. Note that there are more eosinophils in the torn region than the intact region, corroborating the inverse relationship between inflammation and fibre strength.

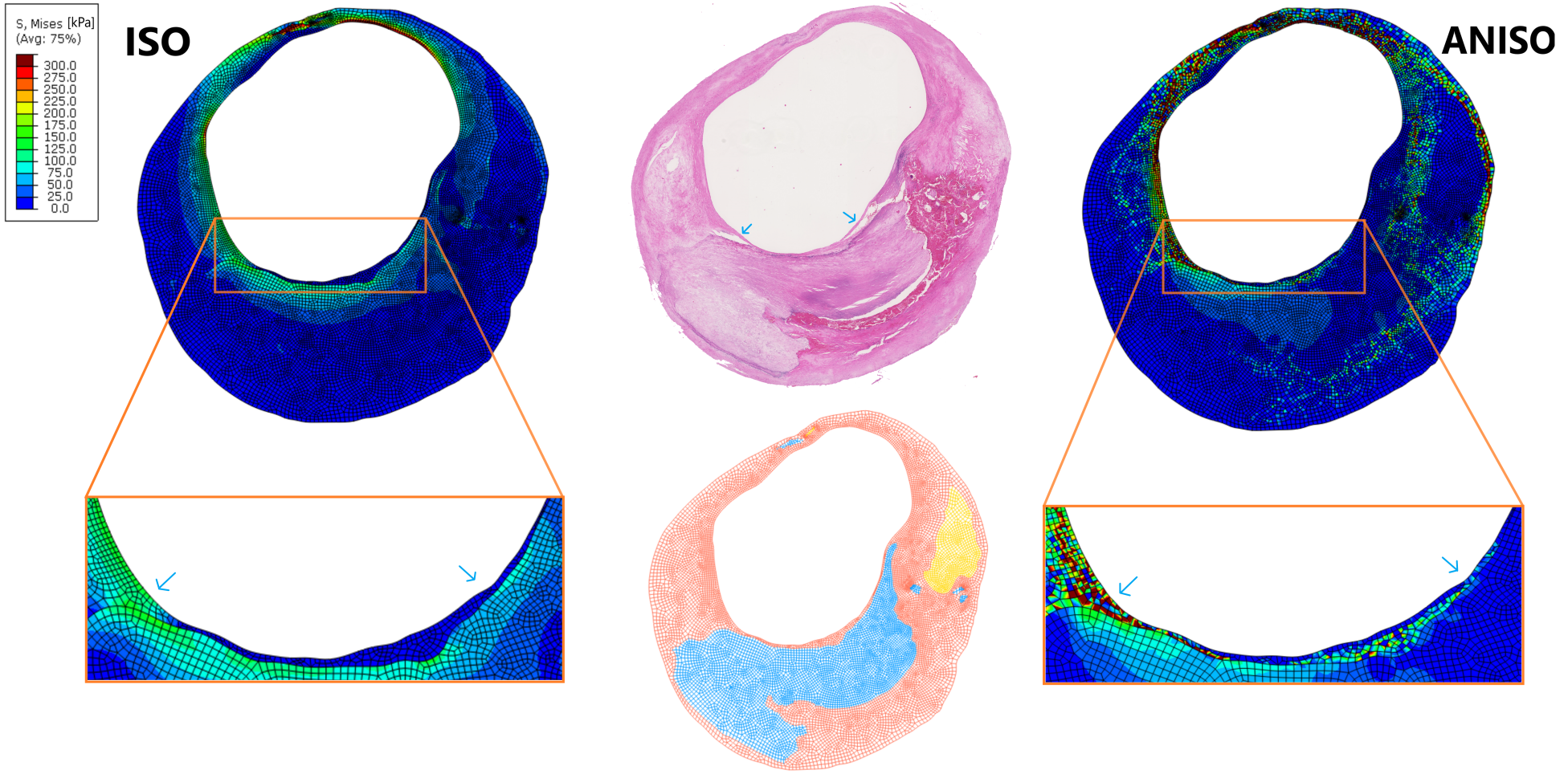

Figure D.7: Hard Inclusion and Fibre Shielding Effects in section 07-128_19500
Center: Histology and Segmented FEM. In the FEM, red elements indicate intima, blue calcification, and yellow necrotic core. In the Histology, blue Arrows indicate damage-sites.
Left: Isotropic FEM Output. Note the lack of cap-stress at the right damage-site and relatively moderate cap-stress at the left site. At both sites, stress is diverted from the cap into the hard inclusion (i.e. hard inclusion shielding).
Right: Anisotropic FEM Output. Note greater cap-stresses relative to the isotropic model at both damage-sites, as well as lower stresses in the hard-inclusion, due to fibre-shielding. As a result, anisotropic models are more sensitive to damage at superficial hard inclusions.

Appendix E

Metric Correlation p-Values

p-values Within-Model Correlations													
	Anisotropic / Isotropic	Stress					Strain				Energy		
		vMises	SMaxIPP	S11	S22	S12	LEMaxIPP	LE11	LE22	LE12	ELSE	ESEDEN	SENER
Stress	vMises		0.0000	0.0000	0.1674	0.0000	0.0000	0.0000	0.0000	0.0000	0.0000	0.0000	0.0000
	SMaxIPP	0.0000		0.0000	0.0000	0.0000	0.0000	0.0000	0.0000	0.0000	0.0000	0.0000	0.0000
	S11	0.0000	0.0000		0.0000	0.0000	0.0000	0.0000	0.0000	0.0000	0.0000	0.0000	0.0000
	S22	0.0000	0.0000	0.0000		0.8674	0.0000	0.0000	0.0000	0.0485	0.0000	0.0000	0.0046
	S12	0.0067	0.0014	0.0135	0.0088		0.0000	0.0000	0.0000	0.0000	0.0000	0.0000	0.0000
Strain	LEMaxIPP	0.0000	0.0000	0.0000	0.0000	0.2334		0.0000	0.0000	0.0000	0.0000	0.0000	0.0000
	LE11	0.0000	0.0000	0.0000	0.0000	0.1207	0.0000		0.0000	0.3935	0.0000	0.0000	0.0000
	LE22	0.0000	0.0000	0.0000	0.0000	0.1207	0.0000	0.0000		0.3935	0.0000	0.0000	0.0000
	LE12	0.0011	0.0001	0.0008	0.0858	0.0000	0.1908	0.0062	0.0061		0.0000	0.0000	0.0000
Energy	ELSE	0.0000	0.0000	0.0000	0.0000	0.8100	0.0000	0.0000	0.0000	0.2966		0.0000	0.0000
	ESEDEN	0.0000	0.0000	0.0000	0.0000	0.0191	0.0000	0.0000	0.0000	0.0069	0.0000		0.0000
	SENER	0.0000	0.0000	0.0000	0.0000	0.0267	0.0000	0.0000	0.0000	0.0099	0.0000	0.0000	

Figure E.1: p-values for Within-Model Correlation Coefficients (fig. 3.5). Upper-right triangle contains anistropic auto-correlation p-values, lower-left triangle isotropic. Colour Code: Green $< p = 0.05 \leq$ Red

p-values Cross-Model Correlations													
		Stress					Strain				Energy		
		vMises	SMaxIPP	S11	S22	S12	LEMaxIPP	LE11	LE22	LE12	ELSE	ESEDEN	SENER
Stress	vMises	0.0000	0.0000	0.0000	0.0000	0.0037	0.0000	0.0000	0.0000	0.0240	0.0000	0.0000	0.0000
	SMaxIPP	0.0000	0.0000	0.0000	0.0000	0.0037	0.0000	0.0000	0.0000	0.0274	0.0000	0.0000	0.0000
	S11	0.0000	0.0000	0.0000	0.0000	0.0008	0.0000	0.0000	0.0000	0.0366	0.0000	0.0000	0.0000
	S22	0.0000	0.0000	0.0000	0.0000	0.0422	0.0000	0.0000	0.0000	0.1339	0.0000	0.0000	0.0000
	S12	0.0000	0.0000	0.0000	0.0304	0.2729	0.0000	0.0000	0.0000	0.3073	0.0000	0.0000	0.0000
Strain	LEMaxIPP	0.0000	0.0000	0.0000	0.0000	0.0021	0.0000	0.0000	0.0000	0.0166	0.0000	0.0000	0.0000
	LE11	0.0000	0.0000	0.0000	0.0000	0.0000	0.0000	0.0000	0.0000	0.0001	0.1003	0.0000	0.0000
	LE22	0.0000	0.0000	0.0000	0.0000	0.0000	0.0000	0.0000	0.0000	0.0001	0.1006	0.0000	0.0000
	LE12	0.0000	0.0000	0.0000	0.0147	0.0105	0.0000	0.0000	0.0000	0.0091	0.0000	0.0000	0.0000
Energy	ELSE	0.0000	0.0000	0.0000	0.0000	0.1881	0.0000	0.0000	0.0000	0.3408	0.0000	0.0000	0.0000
	ESEDEN	0.0000	0.0000	0.0000	0.0000	0.6088	0.0000	0.0000	0.0000	0.7197	0.0000	0.0000	0.0000
	SENER	0.0000	0.0000	0.0000	0.0000	0.9752	0.0000	0.0000	0.0000	0.8870	0.0000	0.0000	0.0000

Figure E.2: p-values for Cross-Model Correlation Coefficients (fig. 3.6). Colour Code: Green $< p = 0.05 \leq$ Red

Appendix F

Metric Sensitivity Tables ('Hit'-Rates)

F.1 Rupture Sensitivities (Stratified)

Ruptures: Fully Stratified										
Inclusion-Type:	Soft (n_{RLS} = 30)				Hard (n_{RLH} = 11)				None (n_{RLNo} = 2)	
Inclusion-Depth:	Superficial (n_{RLSS} = 15)		Deep (n_{RLSD} = 15)		Superficial (n_{RLHS} = 10)		Deep (n_{RLHD} = 1)		-	
	ISO	ANISO	ISO	ANISO	ISO	ANISO	ISO	ANISO	ISO	ANISO
vMises	73%	73%	47%	87%	10%	40%	100%	100%	50%	50%
SMaxIPP	73%	67%	47%	87%	10%	40%	100%	100%	50%	50%
S11	67%	87%	47%	93%	20%	60%	100%	100%	50%	50%
S22	80%	93%	67%	93%	30%	60%	100%	0%	50%	50%
S12	87%	93%	80%	93%	10%	50%	100%	100%	50%	50%
LEMaxIPP	73%	100%	40%	87%	30%	80%	100%	100%	100%	100%
LE11	80%	100%	60%	100%	40%	80%	100%	100%	50%	100%
LE22	93%	100%	73%	100%	40%	80%	100%	100%	100%	100%
LE12	80%	100%	80%	100%	60%	90%	100%	100%	50%	100%
ELSE	73%	67%	53%	67%	10%	10%	100%	100%	50%	100%
ESEDEN	80%	67%	40%	73%	10%	20%	100%	100%	100%	100%
SENER	73%	93%	53%	93%	10%	50%	100%	100%	50%	100%

Figure F.1: Metrics' rupture-sensitivity results, stratified by inclusion-type and -depth. The 'hit-rates' (true-positive incidence) are presented as percentages and colour-coded for readability: Red (0-40%), Yellow (40-70%), Light Green (70-85%), Dark Green (>85%)

F.2 Fissure Sensitivities (Stratified)

F.2.1 Luminal Fissures

Fissures @Lumen: Fully Stratified											
	Inclusion Type:	Soft (n_{FLS} = 31)				Hard (n_{FLH} = 18)				None (n_{FLNo} = 11)	
	Inclusion Depth:	Superficial (n_{FLSS} = 5)		Deep (n_{FLSD} = 26)		Superficial (n_{FLHS} = 7)		Deep (n_{FLHD} = 11)		-	
		ISO	ANISO	ISO	ANISO	ISO	ANISO	ISO	ANISO	ISO	ANISO
Stress	*vMises*	80%	80%	50%	69%	29%	71%	45%	64%	55%	55%
	SMaxIPP	80%	80%	50%	69%	14%	43%	45%	64%	45%	55%
	S11	80%	80%	58%	85%	29%	57%	36%	64%	64%	64%
	S22	80%	100%	69%	96%	29%	86%	45%	73%	55%	73%
	S12	80%	80%	58%	85%	0%	29%	45%	73%	55%	55%
Strain	*LEMaxIPP*	80%	100%	50%	85%	71%	86%	73%	91%	55%	100%
	LE11	80%	100%	77%	92%	57%	71%	55%	82%	73%	100%
	LE22	100%	100%	81%	88%	43%	71%	55%	82%	73%	100%
	LE12	100%	80%	65%	92%	43%	86%	73%	100%	73%	82%
Energy	*ELSE*	80%	80%	65%	62%	29%	71%	45%	55%	45%	45%
	ESEDEN	40%	80%	42%	65%	29%	57%	45%	36%	45%	55%
	SENER	80%	80%	54%	77%	29%	71%	45%	55%	45%	55%

Figure F.2: Metrics' fissure-sensitivity results for damage at the lumen, stratified by inclusion-type and -depth. The 'hit-rates' (true-positive incidence) are presented as percentages and colour-coded for readability: Red (0-40%), Yellow (40-70%), Light Green (70-85%), Dark Green (>85%)

F.2.2 Fissures at Inclusions

Fissures @Inclusion: Fully Stratified									
	Inclusion Type:	Soft (n_{FIS} = 46)				Hard (n_{FIH} = 18)			
	Inclusion Depth:	Superficial (n_{FIS} = 6)		Deep (n_{FISD} = 40)		Superficial (n_{FIH} = 7)		Deep (n_{FLHD} = 11)	
		ISO	ANISO	ISO	ANISO	ISO	ANISO	ISO	ANISO
Stress	*vMises*	33%	67%	51%	68%	43%	43%	55%	55%
	SMaxIPP	50%	67%	51%	73%	71%	43%	55%	45%
	S11	67%	83%	56%	76%	57%	43%	64%	64%
	S22	67%	100%	73%	83%	57%	71%	73%	73%
	S12	50%	100%	73%	73%	57%	86%	73%	82%
Strain	*LEMaxIPP*	33%	67%	41%	54%	43%	29%	64%	45%
	LE11	67%	100%	68%	80%	57%	86%	73%	91%
	LE22	83%	100%	73%	76%	43%	71%	73%	91%
	LE12	33%	100%	78%	80%	57%	71%	82%	82%
Energy	*ELSE*	50%	83%	51%	56%	43%	0%	36%	36%
	ESEDEN	33%	83%	34%	54%	43%	0%	64%	45%
	SENER	33%	100%	44%	68%	43%	0%	55%	45%

Figure F.3: Metrics' fissure-sensitivity results for damage at inclusions, stratified by inclusion-type and -depth. The 'hit-rates' (true-positive incidence) are presented as percentages and colour-coded for readability: Red (0-40%), Yellow (40-70%), Light Green (70-85%), Dark Green (>85%)

Appendix G

Metric Strength Thresholds

G.1 Inclusion Strength Thresholds

Necrotic Cores			
		Isotropic	Anisotropic
Stress [kPa]	vMises	37*	77*
	SMaxIPP	32*	54*
	S11	25*	39*
	S22	6.8	12*
	S12	5.5*	3.9*
Strain [%]	LEMaxIPP	5.3	3.6
	LE11	2.0*	6.2
	LE22	2.0*	6.2
	LE12	3.0	2.0*
Energy	ELSE [mJ]	0.0035*	0.0019*
	ESEDEN $[\frac{mJ}{mm^3}]$	1.0*	0.61*
	SENER $[\frac{mJ}{V_e}]$	1.0*	0.63*

Calcifications			
		Isotropic	Anisotropic
Stress [kPa]	vMises	53	116*
	SMaxIPP	45	90*
	S11	26*	76*
	S22	22	20
	S12	16	6
Strain [%]	LEMaxIPP	1.5	1.1
	LE11	0.9*	0.3*
	LE22	0.9*	0.3*
	LE12	1.1	0.8
Energy	ELSE [mJ]	0.0012*	0.00054*
	ESEDEN $[\frac{mJ}{mm^3}]$	0.50*	0.40*
	SENER $[\frac{mJ}{V_e}]$	0.53*	0.43*

Table G.1: At-Inclusion Strength Thresholds, estimated using Isotropic and Anisotropic models.
N.B: V_e denotes (current) element-volume

Bibliography

[1] Institute for Health Metrics and Evaluation University of Washington, "GBD 2019 Compare," https://vizhub.healthdata.org/gbd-compare/, 2022, accessed: 20-10-2022.

[2] J. Engdahl, M. Holmberg, B. Karlson, R. Luepker, and J. Herlitz, "The epidemiology of out-of-hospital 'sudden'cardiac arrest," *Resuscitation*, vol. 52, no. 3, pp. 235–245, 2002.

[3] A. S. Adabag, R. V. Luepker, V. L. Roger, and B. J. Gersh, "Sudden cardiac death: epidemiology and risk factors," *Nature Reviews Cardiology*, vol. 7, no. 4, pp. 216–225, 2010.

[4] L. Phillips, J. Whisnant, and T. Reagan, "Sudden death from stroke." *Stroke*, vol. 8, no. 3, pp. 392–395, 1977.

[5] S. S. Virani, A. Alonso, H. J. Aparicio, E. J. Benjamin, M. S. Bittencourt, C. W. Callaway, A. P. Carson, A. M. Chamberlain, S. Cheng, F. N. Delling *et al.*, "Heart disease and stroke statistics 2021 update: a report from the american heart association," *Circulation*, vol. 143, no. 8, pp. e254–e743, 2021.

[6] A. Naylor, J.-B. Ricco, G. De Borst, S. Debus, J. De Haro, A. Halliday, G. Hamilton, J. Kakisis, S. Kakkos, S. Lepidi *et al.*, "Editor's choice–management of atherosclerotic carotid and vertebral artery disease: 2017 clinical practice guidelines of the european society for vascular surgery (esvs)," *European Journal of Vascular and Endovascular Surgery*, vol. 55, no. 1, pp. 3–81, 2018.

[7] J. D. Spence, "Management of asymptomatic carotid stenosis," *Neurologic Clinics*, vol. 33, no. 2, pp. 443–457, 2015.

[8] T. R. Dawber, G. F. Meadors, and F. E. Moore Jr, "Epidemiological approaches to heart disease: the framingham study," *American Journal of Public Health and the Nations Health*, vol. 41, no. 3, pp. 279–286, 1951.

[9] R. E. Tracy, W. P. Newman III, W. A. Wattigney, and G. S. Berenson, "Risk factors and atherosclerosis in youth autopsy findings of the bogalusa heart study," *The American journal of the medical sciences*, vol. 310, pp. S37–S41, 1995.

[10] J.-C. Fruchart, M. C. Nierman, E. S. Stroes, J. J. Kastelein, and P. Duriez, "New risk factors for atherosclerosis and patient risk assessment," *Circulation*, vol. 109, no. 23_suppl_1, pp. III–15, 2004.

[11] S. Minelli, P. Minelli, and M. R. Montinari, "Reflections on atherosclerosis: lesson from the past and future research directions," *Journal of multidisciplinary healthcare*, vol. 13, p. 621, 2020.

[12] H. Lu and A. Daugherty, "Recent highlights atvb atherosclerosis," *Arteriosclerosis, Thrombosis, and Vascular Biology (Highwire)*, vol. 35, no. 3, p. 485–491, 2015.

[13] D. Steinberg, "In celebration of the 100th anniversary of the lipid hypothesis of atherosclerosis," *Journal of lipid research*, vol. 54, no. 11, pp. 2946–2949, 2013.

[14] P. Libby and G. K. Hansson, "From focal lipid storage to systemic inflammation: Jacc review topic of the week," *Journal of the American College of Cardiology*, vol. 74, no. 12, pp. 1594–1607, 2019.

[15] D. S. Celermajer, C. K. Chow, E. Marijon, N. M. Anstey, and K. S. Woo, "Cardiovascular disease in the developing world: prevalences, patterns, and the potential of early disease detection," *Journal of the American College of Cardiology*, vol. 60, no. 14, pp. 1207–1216, 2012.

[16] G. Vilahur, J. J. Badimon, R. Bugiardini, and L. Badimon, "Perspectives: The burden of cardiovascular risk factors and coronary heart disease in europe and worldwide," *European Heart Journal Supplements*, vol. 16, no. suppl_A, pp. A7–A11, 2014.

[17] L. E. Mantella, K. Liblik, and A. M. Johri, "Vascular imaging of atherosclerosis: Strengths and weaknesses," *Atherosclerosis*, vol. 319, pp. 42–50, 2021.

[18] N. Pijls, J. Van Son, R. L. Kirkeeide, B. De Bruyne, and K. L. Gould, "Experimental basis of determining maximum coronary, myocardial, and collateral blood flow by pressure measurements for assessing functional stenosis severity before and after percutaneous transluminal coronary angioplasty." *Circulation*, vol. 87, no. 4, pp. 1354–1367, 1993.

[19] M. Zimarino, F. Prati, R. Marano, F. Angeramo, I. Pescetelli, L. Gatto, V. Marco, I. Bruno, and R. De Caterina, "The value of imaging in subclinical coronary artery disease," *Vascular Pharmacology*, vol. 82, pp. 20–29, 2016.

[20] L. J. Shaw, R. Blankstein, J. J. Bax, M. Ferencik, M. S. Bittencourt, J. K. Min, D. S. Berman, J. Leipsic, T. C. Villines, D. Dey *et al.*, "Society of cardiovascular computed tomography/north american society of cardiovascular imaging–expert consensus document on coronary ct imaging of atherosclerotic plaque," *Journal of Cardiovascular Computed Tomography*, vol. 15, no. 2, pp. 93–109, 2021.

[21] H. Hecht, M. J. Blaha, D. S. Berman, K. Nasir, M. Budoff, J. Leipsic, R. Blankstein, J. Narula, J. Rumberger, and L. J. Shaw, "Clinical indications for coronary artery calcium scoring in asymptomatic patients: expert consensus statement from the society of cardiovascular computed tomography," *Journal of cardiovascular computed tomography*, vol. 11, no. 2, pp. 157–168, 2017.

[22] A. S. Agatston, W. R. Janowitz, F. J. Hildner, N. R. Zusmer, M. Viamonte Jr, and R. Detrano, "Quantification of coronary artery calcium using ultrafast computed tomography," *Journal of the American college of cardiology*, vol. 15, no. 4, pp. 827–832, 1990.

[23] P. Greenland, L. LaBree, S. P. Azen, T. M. Doherty, and R. C. Detrano, "Coronary artery calcium score combined with framingham score for risk prediction in asymptomatic individuals," *Jama*, vol. 291, no. 2, pp. 210–215, 2004.

[24] A. J. Nelson, M. Ardissino, and P. J. Psaltis, "Current approach to the diagnosis of atherosclerotic coronary artery disease: more questions than answers," *Therapeutic Advances in Chronic Disease*, vol. 10, p. 2040622319884819, 2019.

[25] E. J. Topol and S. E. Nissen, "Our preoccupation with coronary luminology: the dissociation between clinical and angiographic findings in ischemic heart disease," *Circulation*, vol. 92, no. 8, pp. 2333–2342, 1995.

[26] M. Al Rifai, A. I. Ahmed, F. Alahdab, and M. H. Al-Mallah, "Clinical utility of coronary artery computed tomography angiography-what we know and what's new?" *Progress in Cardiovascular Diseases*, 2022.

[27] R. Virmani, F. D. Kolodgie, A. P. Burke, A. Farb, and S. M. Schwartz, "Lessons from sudden coronary death: a comprehensive morphological classification scheme for atherosclerotic lesions," *Arteriosclerosis, thrombosis, and vascular biology*, vol. 20, no. 5, pp. 1262–1275, 2000.

[28] F. Crawford, K. Welch, A. Andras, and F. M. Chappell, "Ankle brachial index for the diagnosis of lower limb peripheral arterial disease," *Cochrane Database of Systematic Reviews*, no. 9, 2016.

[29] J. Bourque and C. Kramer, "Noninvasive imaging of atherosclerosis," *Cardiovascular Imaging*, pp. 1193–1214, 2011.

[30] K. P. Kim, A. J. Einstein, and A. B. De González, "Coronary artery calcification screening: estimated radiation dose and cancer risk," *Archives of internal medicine*, vol. 169, no. 13, pp. 1188–1194, 2009.

[31] F. Jashari, P. Ibrahimi, R. Nicoll, G. Bajraktari, P. Wester, and M. Y. Henein, "Coronary and carotid atherosclerosis: similarities and differences," *Atherosclerosis*, vol. 227, no. 2, pp. 193–200, 2013.

[32] G. A. Holzapfel, J. J. Mulvihill, E. M. Cunnane, and M. T. Walsh, "Computational approaches for analyzing the mechanics of atherosclerotic plaques: a review," *Journal of biomechanics*, vol. 47, no. 4, pp. 859–869, 2014.

[33] F. D. Kolodgie, A. P. Burke, A. Farb, H. K. Gold, J. Yuan, J. Narula, A. V. Finn, and R. Virmani, "The thin-cap fibroatheroma: a type of vulnerable plaque: the major precursor lesion to acute coronary syndromes," *Current opinion in cardiology*, vol. 16, no. 5, pp. 285–292, 2001.

[34] P. D. Richardson, M. Davies, and G. Born, "Influence of plaque configuration and stress distribution on fissuring of coronary atherosclerotic plaques," *The Lancet*, vol. 334, no. 8669, pp. 941–944, 1989.

[35] G. C. Cheng, H. M. Loree, R. D. Kamm, M. C. Fishbein, and R. T. Lee, "Distribution of circumferential stress in ruptured and stable atherosclerotic lesions. a structural analysis with histopathological correlation." *Circulation*, vol. 87, no. 4, pp. 1179–1187, 1993.

[36] A. C. Akyildiz, L. Speelman, H. van Brummelen, M. A. Gutiérrez, R. Virmani, A. van der Lugt, A. F. van der Steen, J. J. Wentzel, and F. J. Gijsen, "Effects of intima stiffness and plaque morphology on peak cap stress," *Biomedical engineering online*, vol. 10, no. 1, pp. 1–13, 2011.

[37] Y. Vengrenyuk, S. Carlier, S. Xanthos, L. Cardoso, P. Ganatos, R. Virmani, S. Einav, L. Gilchrist, and S. Weinbaum, "A hypothesis for vulnerable plaque rupture due to stress-induced debonding around cellular microcalcifications in thin fibrous caps," *Proceedings of the National Academy of Sciences*, vol. 103, no. 40, pp. 14 678–14 683, 2006.

[38] N. Maldonado, A. Kelly-Arnold, Y. Vengrenyuk, D. Laudier, J. T. Fallon, R. Virmani, L. Cardoso, and S. Weinbaum, "A mechanistic analysis of the role of microcalcifications in atherosclerotic plaque stability: potential implications for plaque rupture," *American Journal of Physiology-Heart and Circulatory Physiology*, vol. 303, no. 5, pp. H619–H628, 2012.

[39] C. Yuan, L. M. Mitsumori, M. S. Ferguson, N. L. Polissar, D. Echelard, G. Ortiz, R. Small, J. W. Davies, W. S. Kerwin, and T. S. Hatsukami, "In vivo accuracy of multispectral magnetic resonance imaging for identifying lipid-rich necrotic cores and intraplaque hemorrhage in advanced human carotid plaques," *Circulation*, vol. 104, no. 17, pp. 2051–2056, 2001.

[40] C. Yuan, S.-x. Zhang, N. L. Polissar, D. Echelard, G. Ortiz, J. W. Davis, E. Ellington, M. S. Ferguson, and T. S. Hatsukami, "Identification of fibrous cap rupture with magnetic resonance imaging is highly associated with recent transient ischemic attack or stroke," *Circulation*, vol. 105, no. 2, pp. 181–185, 2002.

[41] P. A. Calvert, D. R. Obaid, M. O'Sullivan, L. M. Shapiro, D. McNab, C. G. Densem, P. M. Schofield, D. Braganza, S. C. Clarke, K. K. Ray *et al.*, "Association between ivus findings and adverse outcomes in patients with coronary artery disease: the viva (vh-ivus in vulnerable atherosclerosis) study," *JACC: Cardiovascular imaging*, vol. 4, no. 8, pp. 894–901, 2011.

[42] J. M. Cheng, H. M. Garcia-Garcia, S. P. de Boer, I. Kardys, J. H. Heo, K. M. Akkerhuis, R. M. Oemrawsingh, R. T. van Domburg, J. Ligthart, K. T. Witberg *et al.*, "In vivo detection of high-risk coronary plaques by radiofrequency intravascular ultrasound and cardiovascular outcome: results of the atheroremo-ivus study," *European heart journal*, vol. 35, no. 10, pp. 639–647, 2014.

[43] G. W. Stone, A. Maehara, A. J. Lansky, B. De Bruyne, E. Cristea, G. S. Mintz, R. Mehran, J. McPherson, N. Farhat, S. P. Marso *et al.*, "A prospective natural-history study of coronary atherosclerosis," *New England Journal of Medicine*, vol. 364, no. 3, pp. 226–235, 2011.

[44] D. Erlinge, A. Maehara, O. Ben-Yehuda, H. E. Bøtker, M. Maeng, L. Kjøller-Hansen, T. Engstrøm, M. Matsumura, A. Crowley, O. Dressler *et al.*, "Identification of vulnerable plaques and patients by intracoronary near-infrared spectroscopy and ultrasound (prospect ii): a prospective natural history study," *The Lancet*, vol. 397, no. 10278, pp. 985–995, 2021.

[45] P. Libby and G. Pasterkamp, "Requiem for the 'vulnerable plaque'," *European heart journal*, vol. 36, no. 43, pp. 2984–2987, 2015.

[46] G. Rioufol, G. Finet, I. Ginon, X. Andre-Fouet, R. Rossi, E. Vialle, E. Desjoyaux, G. Convert, J. Huret, and A. Tabib, "Multiple atherosclerotic plaque rupture in acute coronary syndrome: a three-vessel intravascular ultrasound study," *circulation*, vol. 106, no. 7, pp. 804–808, 2002.

[47] A. L. Figueroa, S. S. Subramanian, R. C. Cury, Q. A. Truong, J. A. Gardecki, G. J. Tearney, U. Hoffmann, T. J. Brady, and A. Tawakol, "Distribution of inflammation within carotid atherosclerotic plaques with high-risk morphological features: a comparison between positron emission tomography activity, plaque morphology, and histopathology," *Circulation: Cardiovascular Imaging*, vol. 5, no. 1, pp. 69–77, 2012.

[48] P. Libby *et al.*, "Collagenases and cracks in the plaque," *The Journal of clinical investigation*, vol. 123, no. 8, pp. 3201–3203, 2013.

[49] D. Tang, Z. Teng, G. Canton, C. Yang, M. Ferguson, X. Huang, J. Zheng, P. K. Woodard, and C. Yuan, "Sites of rupture in human atherosclerotic carotid plaques are associated with high structural stresses: an in vivo mri-based 3d fluid-structure interaction study," *Stroke*, vol. 40, no. 10, pp. 3258–3263, 2009.

[50] U. Sadat, Z. Teng, V. Young, M. Graves, M. Gaunt, and J. Gillard, "High-resolution magnetic resonance imaging-based biomechanical stress analysis of carotid atheroma: a comparison of single transient ischaemic attack, recurrent transient ischaemic attacks, non-disabling stroke and asymptomatic patient groups," *European Journal of Vascular and Endovascular Surgery*, vol. 41, no. 1, pp. 83–90, 2011.

[51] G. R. Douglas, "Fibre microstructure and mechanics of atherosclerotic plaques," Ph.D. dissertation, Cambridge University, 2018. [Online]. Available: https://www.repository.cam.ac.uk/handle/1810/271511

[52] Z. Teng, Y. Zhang, Y. Huang, J. Feng, J. Yuan, Q. Lu, M. P. Sutcliffe, A. J. Brown, Z. Jing, and J. H. Gillard, "Material properties of components in human carotid atherosclerotic plaques: a uniaxial extension study," *Acta biomaterialia*, vol. 10, no. 12, pp. 5055–5063, 2014.

[53] A. C. Akyildiz, L. Speelman, B. van Velzen, R. R. Stevens, A. F. Van Der Steen, W. Huberts, and F. J. Gijsen, "Intima heterogeneity in stress assessment of atherosclerotic plaques," *Interface Focus*, vol. 8, no. 1, p. 20170008, 2018.

[54] R. P. Vito and S. A. Dixon, "Blood vessel constitutive models—1995–2002," *Annual review of biomedical engineering*, vol. 5, no. 1, pp. 413–439, 2003.

[55] V. M. Heiland, C. Forsell, J. Roy, U. Hedin, and T. C. Gasser, "Identification of carotid plaque tissue properties using an experimental–numerical approach," *Journal of the mechanical behavior of biomedical materials*, vol. 27, pp. 226–238, 2013.

[56] G. A. Holzapfel and R. W. Ogden, "Constitutive modelling of passive myocardium: a structurally based framework for material characterization," *Philosophical Transactions of the Royal Society A: Mathematical, Physical and Engineering Sciences*, vol. 367, no. 1902, pp. 3445–3475, 2009.

[57] H. Nieuwstadt, A. Akyildiz, L. Speelman, R. Virmani, A. van der Lugt, A. van der Steen, J. Wentzel, and F. Gijsen, "The influence of axial image resolution on atherosclerotic plaque stress computations," *Journal of Biomechanics*, vol. 46, no. 4, pp. 689–695, 2013.

[58] A. C. Akyildiz, L. Speelman, H. van Brummelen, M. A. Gutiérrez, R. Virmani, A. van der Lugt, A. F. van der Steen, J. J. Wentzel, and F. J. Gijsen, "Effects of intima stiffness and plaque morphology on peak cap stress," *Biomedical engineering online*, vol. 10, pp. 1–13, 2011.

[59] A. C. Akyildiz, L. Speelman, H. A. Nieuwstadt, H. van Brummelen, R. Virmani, A. van der Lugt, A. F. van der Steen, J. J. Wentzel, and F. J. Gijsen, "The effects of plaque morphology and material properties on peak cap stress in human coronary arteries," *Computer Methods in Biomechanics and Biomedical Engineering*, vol. 19, no. 7, pp. 771–779, 2016.

[60] C. Costopoulos, Y. Huang, A. J. Brown, P. A. Calvert, S. P. Hoole, N. E. West, J. H. Gillard, Z. Teng, and M. R. Bennett, "Plaque rupture in coronary atherosclerosis is associated with increased plaque structural stress," *JACC: Cardiovascular Imaging*, vol. 10, no. 12, pp. 1472–1483, 2017.

[61] G. R. Douglas, A. J. Brown, J. H. Gillard, M. R. Bennett, M. P. Sutcliffe, and Z. Teng, "Impact of fiber structure on the material stability and rupture mechanisms of coronary atherosclerotic plaques," *Annals of Biomedical Engineering*, vol. 45, pp. 1462–1474, 2017.

[62] B. V. Shekhonin, S. P. Domogatsky, V. R. Muzykantov, G. L. Idelson, and V. S. Rukosuev, "Distribution of type i, iii, iv and v collagen in normal and atherosclerotic human arterial wall: immunomorphological characteristics," *Collagen and related research*, vol. 5, no. 4, pp. 355–368, 1985.

[63] A. Creane, E. Maher, S. Sultan, N. Hynes, D. J. Kelly, and C. Lally, "Prediction of fibre architecture and adaptation in diseased carotid bifurcations," *Biomechanics and modeling in mechanobiology*, vol. 10, pp. 831–843, 2011.

[64] M. J. Daemen, M. S. Ferguson, F. J. Gijsen, D. S. Hippe, M. E. Kooi, K. Demarco, A. C. van der Wal, C. Yuan, and T. S. Hatsukami, "Carotid plaque fissure: an underestimated source of intraplaque hemorrhage," *Atherosclerosis*, vol. 254, pp. 102–108, 2016.

[65] S. K. Nadkarni, M. C. Pierce, B. H. Park, J. F. de Boer, P. Whittaker, B. E. Bouma, J. E. Bressner, E. Halpern, S. L. Houser, and G. J. Tearney, "Measurement of collagen and smooth muscle cell content in atherosclerotic plaques using polarization-sensitive optical coherence tomography," *Journal of the American College of Cardiology*, vol. 49, no. 13, pp. 1474–1481, 2007.

[66] V. Flamini, C. Kerskens, C. Simms, and C. Lally, "Fibre orientation of fresh and frozen porcine aorta determined non-invasively using diffusion tensor imaging," *Medical Engineering & Physics*, vol. 35, no. 6, pp. 765–776, 2013.

[67] A. C. Akyildiz, C.-K. Chai, C. W. Oomens, A. van der Lugt, F. P. Baaijens, G. J. Strijkers, and F. J. Gijsen, "3d fiber orientation in atherosclerotic carotid plaques," *Journal of Structural Biology*, vol. 200, no. 1, pp. 28–35, 2017.

[68] D. Mohan and J. W. Melvin, "Failure properties of passive human aortic tissue. ii—biaxial tension tests," *Journal of biomechanics*, vol. 16, no. 1, pp. 31–44, 1983.

[69] E. E. Gdoutos, *Fracture mechanics: an introduction*. Springer Nature, 2020, vol. 263.

[70] J. N. Cameron, O. H. Mehta, M. Michail, J. Chan, S. J. Nicholls, M. R. Bennett, and A. J. Brown, "Exploring the relationship between biomechanical stresses and coronary atherosclerosis," *Atherosclerosis*, vol. 302, pp. 43–51, 2020.

[71] O. Y. Hung, A. J. Brown, S. G. Ahn, A. Veneziani, D. P. Giddens, and H. Samady, "Association of wall shear stress with coronary plaque progression and transformation," *Interventional cardiology clinics*, vol. 4, no. 4, pp. 491–502, 2015.

[72] M. Walsh, E. Cunnane, J. Mulvihill, A. Akyildiz, F. Gijsen, and G. A. Holzapfel, "Uniaxial tensile testing approaches for characterisation of atherosclerotic plaques," *Journal of biomechanics*, vol. 47, no. 4, pp. 793–804, 2014.

[73] A. Versluis, A. J. Bank, and W. H. Douglas, "Fatigue and plaque rupture in myocardial infarction," *Journal of biomechanics*, vol. 39, no. 2, pp. 339–347, 2006.

[74] Y. Huang, Z. Teng, U. Sadat, J. He, M. J. Graves, and J. H. Gillard, "In vivo mri-based simulation of fatigue process: a possible trigger for human carotid atherosclerotic plaque rupture," *Biomedical engineering online*, vol. 12, pp. 1–12, 2013.

[75] X. Pei, B. Wu, and Z.-Y. Li, "Fatigue crack propagation analysis of plaque rupture," *Journal of Biomechanical Engineering*, vol. 135, no. 10, p. 101003, 2013.

[76] A. Rezvani-Sharif, M. Tafazzoli-Shadpour, D. Kazemi-Saleh, and M. Sotoudeh-Anvari, "Stress analysis of fracture of atherosclerotic plaques: crack propagation modeling," *Medical & Biological Engineering & Computing*, vol. 55, pp. 1389–1400, 2017.

[77] J. A. Schaar, C. L. De Korte, F. Mastik, C. Strijder, G. Pasterkamp, E. Boersma, P. W. Serruys, and A. F. Van Der Steen, "Characterizing vulnerable plaque features with intravascular elastography," *Circulation*, vol. 108, no. 21, pp. 2636–2641, 2003.

[78] H. H. Hansen, G. J. de Borst, M. L. Bots, F. L. Moll, G. Pasterkamp, and C. L. de Korte, "Validation of noninvasive in vivo compound ultrasound strain imaging using histologic plaque vulnerability features," *Stroke*, vol. 47, no. 11, pp. 2770–2775, 2016.

[79] R. Lv, A. Maehara, M. Matsumura, L. Wang, C. Zhang, M. Huang, X. Guo, H. Samady, D. P. Giddens, J. Zheng *et al.*, "Using optical coherence tomography and intravascular ultrasound imaging to quantify coronary plaque cap stress/strain and progression: a follow-up study using 3d thin-layer models," *Frontiers in Bioengineering and Biotechnology*, vol. 9, p. 713525, 2021.

[80] A. H. Hoffman, Z. Teng, J. Zheng, Z. Wu, P. K. Woodard, K. L. Billiar, L. Wang, and D. Tang, "Stiffness properties of adventitia, media, and full thickness human atherosclerotic carotid arteries in the axial and circumferential directions," *Journal of biomechanical engineering*, vol. 139, no. 12, 2017.

[81] A. Cifuentes and A. Kalbag, "A performance study of tetrahedral and hexahedral elements in 3-d finite element structural analysis," *Finite Elements in Analysis and Design*, vol. 12, no. 3-4, pp. 313–318, 1992.

[82] G. Sommer, P. Regitnig, L. Koltringer, and G. A. Holzapfel, "Biaxial mechanical properties of intact and layer-dissected human carotid arteries at physiological and supraphysiological loadings," *American Journal of Physiology-Heart and Circulatory Physiology*, vol. 298, no. 3, pp. H898–H912, 2010.

[83] T. C. Gasser, R. W. Ogden, and G. A. Holzapfel, "Hyperelastic modelling of arterial layers with distributed collagen fibre orientations," *Journal of the royal society interface*, vol. 3, no. 6, pp. 15–35, 2006.

[84] H. M. Loree, R. D. Kamm, R. G. Stringfellow, and R. T. Lee, "Effects of fibrous cap thickness on peak circumferential stress in model atherosclerotic vessels." *Circulation research*, vol. 71, no. 4, pp. 850–858, 1992.

[85] H. E. Barrett, K. Van der Heiden, E. Farrell, F. J. Gijsen, and A. C. Akyildiz, "Calcifications in atherosclerotic plaques and impact on plaque biomechanics," *Journal of Biomechanics*, vol. 87, pp. 1–12, 2019.

[86] M. Ghasemi, R. D. Johnston, and C. Lally, "Development of a collagen fibre remodelling rupture risk metric for potentially vulnerable carotid artery atherosclerotic plaques," *Frontiers in Physiology*, p. 1789, 2021.

[87] K. Sakakura, M. Nakano, F. Otsuka, E. Ladich, F. D. Kolodgie, and R. Virmani, "Pathophysiology of atherosclerosis plaque progression," *Heart, Lung and Circulation*, vol. 22, no. 6, pp. 399–411, 2013.

[88] H. Huang, R. Virmani, H. Younis, A. P. Burke, R. D. Kamm, and R. T. Lee, "The impact of calcification on the biomechanical stability of atherosclerotic plaques," *Circulation*, vol. 103, no. 8, pp. 1051–1056, 2001.

[89] G. A. Holzapfel and R. W. Ogden, "Constitutive modelling of arteries," *Proceedings of the Royal Society A: Mathematical, Physical and Engineering Sciences*, vol. 466, no. 2118, pp. 1551–1597, 2010.

[90] T. C. Gasser and G. A. Holzapfel, "Modeling plaque fissuring and dissection during balloon angioplasty intervention," *Annals of biomedical engineering*, vol. 35, pp. 711–723, 2007.

[91] A. Ferrara and A. Pandolfi, "Numerical modelling of fracture in human arteries," *Computer Methods in Biomechanics and Biomedical Engineering*, vol. 11, no. 5, pp. 553–567, 2008.

[92] X. Pei, B. Wu, and Z.-Y. Li, "Fatigue crack propagation analysis of plaque rupture," *Journal of Biomechanical Engineering*, vol. 135, no. 10, p. 101003, 2013.

[93] P. Badel, S. Avril, M. A. Sutton, and S. M. Lessner, "Numerical simulation of arterial dissection during balloon angioplasty of atherosclerotic coronary arteries," *Journal of biomechanics*, vol. 47, no. 4, pp. 878–889, 2014.

[94] B. Merei, P. Badel, L. Davis, M. A. Sutton, S. Avril, and S. M. Lessner, "Atherosclerotic plaque delamination: Experiments and 2d finite element model to simulate plaque peeling in two strains of transgenic mice," *Journal of the mechanical behavior of biomedical materials*, vol. 67, pp. 19–30, 2017.

[95] A. Rezvani-Sharif, M. Tafazzoli-Shadpour, D. Kazemi-Saleh, and M. Sotoudeh-Anvari, "Stress analysis of fracture of atherosclerotic plaques: crack propagation modeling," *Medical & Biological Engineering & Computing*, vol. 55, pp. 1389–1400, 2017.

[96] L. A. Davis, S. E. Stewart, C. G. Carsten III, B. A. Snyder, M. A. Sutton, and S. M. Lessner, "Characterization of fracture behavior of human atherosclerotic fibrous caps using a miniature single edge notched tensile test," *Acta biomaterialia*, vol. 43, pp. 101–111, 2016.

[97] R. van den Berg, "A novel approach to estimating the material properties of atherosclerotic plaque tissue," Master's thesis, Delft University of Technology, 2019.